Natural and artificial lateral lines

Form-function relationship and Detection of water surface waves

DISSERTATION

zur

Erlangung des Doktorgrades (Dr. rer. nat.)

der

Mathematisch-Naturwissenschaftlichen Fakultät

der

Rheinischen Friedrich-Wilhelms-Universität Bonn

vorgelegt von

FELIX KALDENBACH

aus

Euskirchen

Bonn 2016

Angefertigt mit Genehmigung der Mathematisch-Naturwissenschaftlichen Fakultät
der Rheinischen Friedrich-Wilhelms-Universität Bonn

1. Gutachter: Prof. Dr. Horst Bleckmann
2. Gutachter: Prof. Dr. Michael Hofmann
Tag der Promotion: 1.6.2016
Erscheinungsjahr: 2016

Abstract

The lateral line system enables fish to sense weak water motions and pressure gradients. Its smallest sensory units are neuromasts. They are composed of hundreds to thousands of mechanosensitive hair cells covered by a mucous cupula that extends into the water. The cupula is deflected by mechanical forces of the water and the deflection is detected by the hair cells. Canal neuromasts – one type of neuromasts – are located inside fluid filled canals that run parallel to the surface of the fish. The canal lumen is hydrodynamically connected with the surrounding water by pores at each side of a neuromast. Pressure gradients between the pores lead to compensatory fluid motion inside the canal. By measuring the fluid motion in the canal, canal neuromasts can detect pressure gradients.

The working principle of a neuromast has been implemented in a biomimetic flow sensor that can be used in technical applications. In this artificial lateral line (ALL), a transparent silicone bar is positioned inside a fluid filled canal. It guides the light from an LED towards a position sensitive photodiode at the opposite side of the canal. Fluid motion causes a deflection of the silicone bar, which is detected by the position sensitive photodiode.

The present thesis comprises two biomimetic and one neurobiological study in the broad field of lateral line research. In the first study we examined the form-function relationship of individual components (form) and the performance (function) of the ALL. We found that the resonance frequency of the silicone bar determined the resonance frequency of the flow sensor. The thickness and the length of the bar both influenced the resonance frequency as well as the sensitivity. The sensitivity was also influenced by the length and the diameter of the artificial lateral line canal. The distance between the canal pores determined the spatial detection properties of the sensor. The pore diameter influenced its temporal filter properties. The functionality of the sensor in detecting oscillatory fluid motion remained when the canal pores were covered with thin, flexible membranes. The tension, diameter and thickness of the membranes determined the temporal filter properties of the sensor. The density and viscosity of the canal fluid influenced the sensitivity and the temporal filter properties. The acquired knowledge can be used to optimize the sensor for future applications.

In the second study we showed that the ALL can detect water surface waves when it is positioned horizontally below the water surface. We compared the ALL with a sophisticated technical sensor that is commonly used to measure surface waves. We found that some sensor characteristics were inherently associated with the ALL design: measuring differential pressure between two pores led to responses that depended on the propagation direction and frequency of the wave stimulus. In addition, the hydrodynamic interaction of surface wave and sensor altered the surface wave and thus led to discrepancies between the recorded and the actual surface wave. We finally demonstrated that an array of ALLs can be used to determine the direction of a wave train.

In the last part of this thesis we present the miscellaneous results of a research project that was originally designed to investigate the functional significance of the complex lateral line morphology of *Xiphister*, a stichaeid genus found at north-eastern pacific coastlines. For this purpose we planned to 2-dimensionally scan the receptive fields of primary lateral line afferents of *Xiphister* with a resolution of less than 1 mm. Preliminary experiments on goldfish delivered the most detailed receptive field scans of primary lateral line afferents described so far. However, the recorded units in *Xiphister* turned out to be insensitive to mechanical stimuli. Instead, they responded to thermal stimuli: while the ongoing activity varied directly with steady temperatures, sudden temperature changes resulted in a reversed response. Sudden cooling increased and sudden warming decreased neuronal activity.

Contents

List of Figures

I. ALL – Form-Function

II. ALL – Water surface waves

III. *Xiphister* miscellaneous

Abbreviations

ALL	artificial lateral line
CN	canal neuromast
DASPEI	2-(4-dimethyl-aminostyryl)-N-ethyl pyridinium iodide
EPD	effective pore distance
IPD	inter-pore distance
ODS	optical displacement sensor
PLLN	posterior lateral line nerve
POM	polyoxymethylene
PSTH	peristimulus time histogram
PVC	polyvinyl chloride
RMS	root mean square
SN	superficial neuromast

Outline

The present thesis examines various questions in the broad field of lateral line research. It is divided into three parts comprising two biomimetic projects on artificial lateral lines (ALLs) and one mainly neurobiological study on the functional significance of the stunning lateral line morphology of *Xiphister*.

The first part deals with the form-function relationship in an ALL, a biomimetic flow sensor. We systematically altered the physical properties (form) of the sensor and tested how these alterations influenced the performance (function) of the sensor.

In the second part of the thesis we investigated whether the ALL can be used to detect water surface waves. We compared the biomimetic flow sensor with a sophisticated technical sensor that is commonly used to measure surface waves. Furthermore, we demonstrate how an array of ALLs can be used to determine the direction of a wave train.

The third part shows the miscellaneous results of a research project that was designed to electrophysiologically investigate the functional significance of the lateral line morphology of *Xiphister*, a stichaeid genus that can be found at north-eastern pacific coastlines. Although one initial working hypothesis could not be validated, several surprising findings derived from this work and from preliminary tests on goldfish.

The three parts of the thesis are presented in separate chapters, each of which contains an introduction, material & methods, results and discussion section. Especially the first two biomimetic chapters are designed as independent manuscripts for future publication. The first two basic introductory paragraphs of these chapters are almost identical, because both chapters deal with ALLs.

I. ALL – Form-Function

1. Introduction

1.1. Lateral Line

The lateral line system enables fish and most aquatic amphibians to sense weak water motions and pressure gradients (Coombs, 2002). It is essential for a variety of behaviors such as spatial orientation, prey detection, predator avoidance, schooling and intraspecific communication (Bleckmann, 1994). The smallest sensory units of the lateral line system are neuromasts. They are composed of hundreds to thousands of mechanosensitive hair cells covered by a mucous cupula that extends into the water. Mechanical forces of the water deflect the cupula, the deflection is detected by the hair cells and action potentials are propagated to the central nervous system. Neuromasts are classified as one of two main types: Superficial neuromasts (SNs, Fig. 1a) occur free standing on the skin of the fish and respond in proportion to the water velocity. Canal neuromasts (CNs, Fig. 1b) are located inside fluid filled canals that run parallel to the surface of the fish. The canal lumen is hydrodynamically connected with the surrounding water by pores at each side of a CN. Pressure gradients between the pores lead to compensatory fluid motion inside the canal which in turn is detected by the CN. Consequently, CNs respond in proportion to the pressure gradient between adjacent pores (Bleckmann, 1994).

1.2. Biomimetic flow sensor

Gathering flow information is not only important for aquatic animals, but is also relevant in many technical applications. The working principle of CNs has been implemented in a biomimetic flow sensor (Klein, 2009, 2012; Klein & Bleckmann, 2011; Klein et al., 2011). In this sensor, the artificial neuromast (Fig. 1c) was composed of three functional components: Like the neuromast, the transparent silicone bar (1) was positioned inside a fluid filled canal. It guided the light from an LED (2) towards a position sensitive photodiode (3) at the opposite side of the canal. Fluid motion caused a deflection of the silicone bar. The deflection was detected by the position sensitive photodiode.

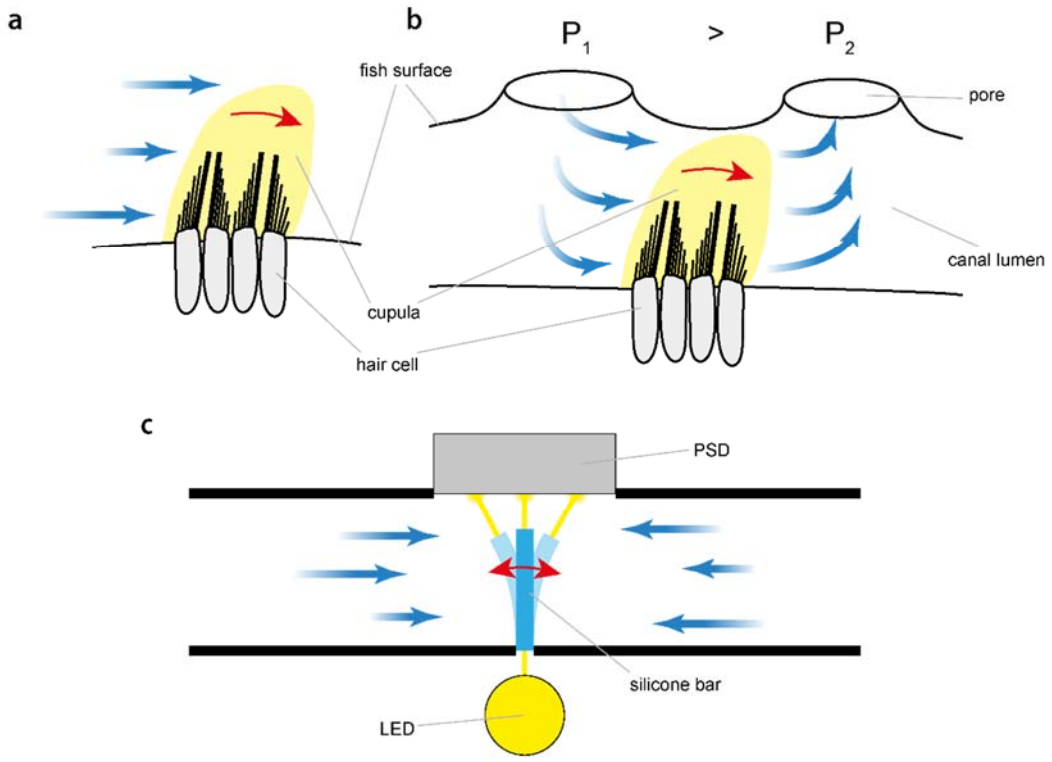

Fig. 1 Biological and artificial neuromasts (**a**) Scheme of a superficial neuromast SN being deflected by fluid motion. (**b**) Scheme of a CN situated inside the lateral line canal between two adjacent pores. Pressure differences between the pores cause fluid motion inside the canal. The canal fluid deflects the cupula of the neuromast. The artificial neuromast (**c**) is the biomimetic interpretation of the CN principle. A transparent silicone bar is deflected by the fluid motion inside a canal. The deflection is detected by a position sensitive photo diode (PSD) onto which the silicone bar guides the light from an LED.

1.3. Morphological diversity of the fish lateral line

Fish inhabit a great variety of hydrodynamic habitats like lakes, fast running rivers or highly turbulent sea shores (Nelson, 2006). In turn, lateral line morphologies show a vast diversity, too (Coombs, 1988). Besides SNs and CNs, neuromasts can also occur in grooves (Merrilees & Crossman, 1973) or may be shielded by ridge-like structures. The size, the shape and the stiffness of the cupula varies as well as the number of hair cells contained in one neuromasts (Münz, 1979). The ratio of SNs and CNs broadly varies (Beckmann et al., 2010), some species entirely lack in SNs, others in CNs. The distribution of SNs is different among species (Schmitz et al., 2014) and there is a great variety of trunk and cephalic canal patterns (Makushok, 1961). Canals can be narrow or wide and the CNs may block few or most of the canal. For instance, cephalic canal diameters vary from 100 µm up to 7 mm. Cephalic canals may be embedded in the dermal bone, in compact layers of dermis or supported by cartilaginous rings. Some canals are solid half canals covered with a thin and

flexible membrane (Dijkgraaf, 1963; Janssen, 1997). Trunk canals in most Osteichthyes are contained within or between modified lateral line scales. In some Stichaeids the trunk canal is formed by dermal like ring structures (Clardy et al., 2015). The pores that connect the canal and the surrounding water may have different diameters. They can be flat with the main canal or they are located at the end of prolonged tubules. These tubules might be branched resulting in multiple pores between two adjacent neuromast. Also multiple neuromasts occur between two adjacent pores.

1.4. Form-function relationship

The functional significance of the lateral line diversity is only partly understood. However, correlations between morphologies and habitats suggest that certain morphologies evolved as adaptations to certain environmental demands (Coombs, 1988).

A common approach to study the form-function relationship of natural lateral lines is to compare different morphologies and search for correlates of certain morphologies with certain habitats. This approach can be difficult and can lead to contradicting results because lateral line morphologies on the one hand as well as habitat properties on the other hand are a complex composition of numerous parameters. The influence of a single parameter of interest might be compensated and thus masked by other, unexpected parameters.

In contrast, studying the form-function relationship in an ALL can be advantageous. Single parameters like the pore diameter can independently be varied and its functional significance can be analyzed. For instance, the functional significance of the complex branching pattern of the trunk lateral line canals of the stichaeid species *Xiphister atropurpureus* remained unclear after electrophysiological tests (Bleckmann & Münz, 1990). However, mimicking the *Xiphister* trunk canals in an ALL revealed a possible spatial filter function of the examined structures (Klein et al., 2013).

ALLs provide pressure and flow information. They might be used in a broad variety of technical fields such as biomedical engineering or process engineering. In fact, as the biological models are adapted to the habitats by shaping their morphology, an ALL can be optimized for its technical requirements by altering its properties and/or dimensions. Thus, studying form-function relationships in

ALLs is not only useful for uncovering the functional significance of biological structures. The acquired knowledge can also be used to optimize the sensor for potential future tasks.

In the present study we systematically varied the dimensions and properties of the peripheral components of the sensor and investigated the influence on the sensors performance. Namely, we varied the dimensions of the silicone bar (thickness and length), the canal (length and diameter) and the pores (diameter and inter-pore distance). Finally, covering the pores with membranes (of different thickness, diameter and tension) enabled us to use canal fluids other than water (with different viscosity and density). The results will be discussed in regard to the optimization potential of the sensor for future tasks.

2. Materials & Methods

2.1. Sensor platform

In the present study, an artificial neuromast (c.f. 1.2) was integrated into a sensor platform that allowed to alter the dimensions and properties of the sensor by exchanging or adding individual components.

The functional units – the LED, the silicone bar, the canal and the position sensitive diode – were incorporated into separate circular polyoxymethylene (POM) plates that were stacked and screwed together (c.f. Fig. 2). The electronic components were mounted on custom fabricated circuit boards. Transparent polyvinyl chloride (PVC) plates were glued onto the POM components to cover the electronics watertight. Supply and data wire outlets were sealed with polyurethane coating. Threaded holes in the front and the back of the sensor were used to mount different adapter plates and to mount the sensor at various positions in the setup.

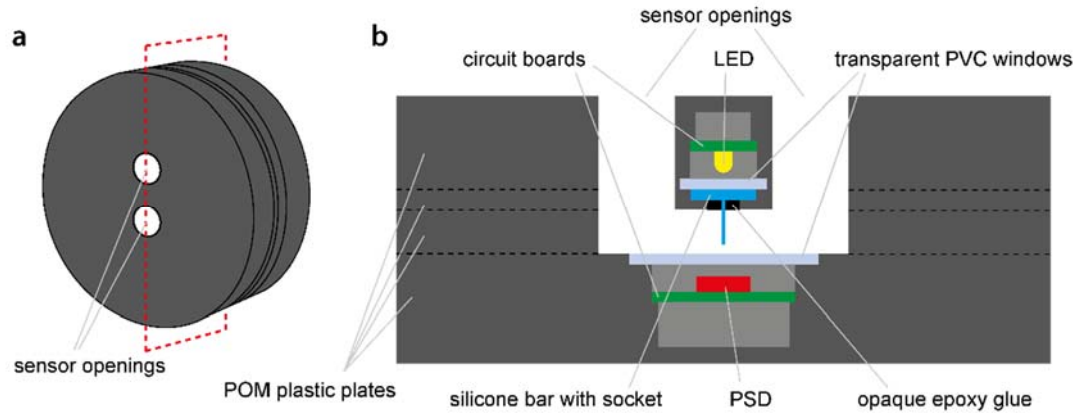

Fig. 2 Biomimetic flow sensor (**a**) Dimetric view of the biomimetic flow sensor used in the study. Dashed rectangle indicates the position of the cross section shown in (**b**). The sensor was built from POM plastic plates. The parts which contain the electronic components are shielded from the water by transparent PVC windows. PSD = position sensitive diode. Dimensions are not to scale.

2.2. Silicone bar

Silicone bars of different length (1, 2 and 3 mm; thickness = 75 µm) and thickness (75, 100 and 125 µm; length = 3 mm) were fitted into separate POM mounting plates allowing to exchange the silicone bars.

2.2.1. Resonance frequency

To measure the resonance frequency, the silicone bar (dismounted from sensor) was manually deflected with tweezers. It rebounded to its initial, straight position after being released. The oscillating rebound movement was videotaped with a high speed camera (Fastcam Ultima APX, Photon, San Diego, CA, USA; 4000 fps) and for each frame the degree of deflection was determined by tracking the bar's tip with a video tracking software (Video Spot Tracker v6.02). The resulting timeline data was analyzed using the Matlab curve fitting toolbox (Matlab Version 7.8.0, The Mathworks, Inc., Natrick, MA, USA). The best fit was calculated according to a damped, single degree of freedom oscillator equation:

$$\alpha(t) = \dot{\propto} e^{-\gamma t} \cdot \sin 2\pi f_d t \quad (1)$$

Here, the deflection (α) is expressed as function of time (t). The decay constant (γ) and the resonance frequency (f_d) of the fit function were used to quantify the silicone bar properties. The experiments were conducted in air as well as when the silicone bar was under water (in a transparent glass bin).

2.2.2. Temporal filter properties

To test the temporal filter properties of the biomimetic flow sensor equipped with silicone bars of different dimensions, the sensor was positioned in a water tank in a vertical pore-to-pore orientation (c.f. Fig. 2a). It was stimulated with dipole pressure fluctuations caused by a vibrating carbon cylinder (c.f. Fig. 3). The cylinder was 1 cm in diameter. It was horizontally positioned 5 mm away from the sensor surface at a vertical level right between the sensor openings. It vibrated parallel to the sensor surface in the direction from one sensor opening to the other. The cylinder was suspended within a carbon frame that was attached to a mechanical shaker (VT-20 Shaker 20N, Sigmatest, Gottmadingen, Germany). The shaker was driven by an AC Power Amplifier (PA75-2CH, Sigmatest, Gottmadingen, Germany) that was controlled by an AD/DA converter (Power 1401, CED, Cambridge, England) that was connected to a PC with the Spike2 software (Version 7, CED, Cambridge, England). An acceleration sensor (ADXL330, Analog devices, Norwood, MA, USA) was contained within the vibrating cylinder to monitor the acceleration of the dipole

source and thus to quantify the pressure fluctuations. To read out its signal, it was connected to the AD/DA converter.

Sine sweep stimuli were applied. The frequency constantly raised from 2 to 200 Hz (fixed rate of relative (not absolute) increase of frequency; $f_n=f_{n-1}*x$). The stimulus duration was 200 s. The stimulus amplitude was adjusted such that none of the sensors (ALL or acceleration sensor) was stimulated outside of its dynamic range. The ALL as well as the acceleration sensor signal were simultaneously recorded with the AD/DA converter. Any DC offset was removed in the Spike2 software (time constant = 10 s). Further analysis was done in Matlab. The integral of the modulus of the signals was calculated for time intervals matching the duration of one vibration cycle (increasingly smaller time intervals for increasing frequencies). We hence divided the integrals of the ALL signal by those of the acceleration sensor signal. The resulting values reflect the strength of the ALL signal in proportion to the applied pressure fluctuation. They are used to quantify the sensitivity of the ALL at a given frequency.

After a sweep stimulus was applied, the next mounting plate carrying a different silicone bar was installed. Each silicone bar was tested three times. The results were averaged.

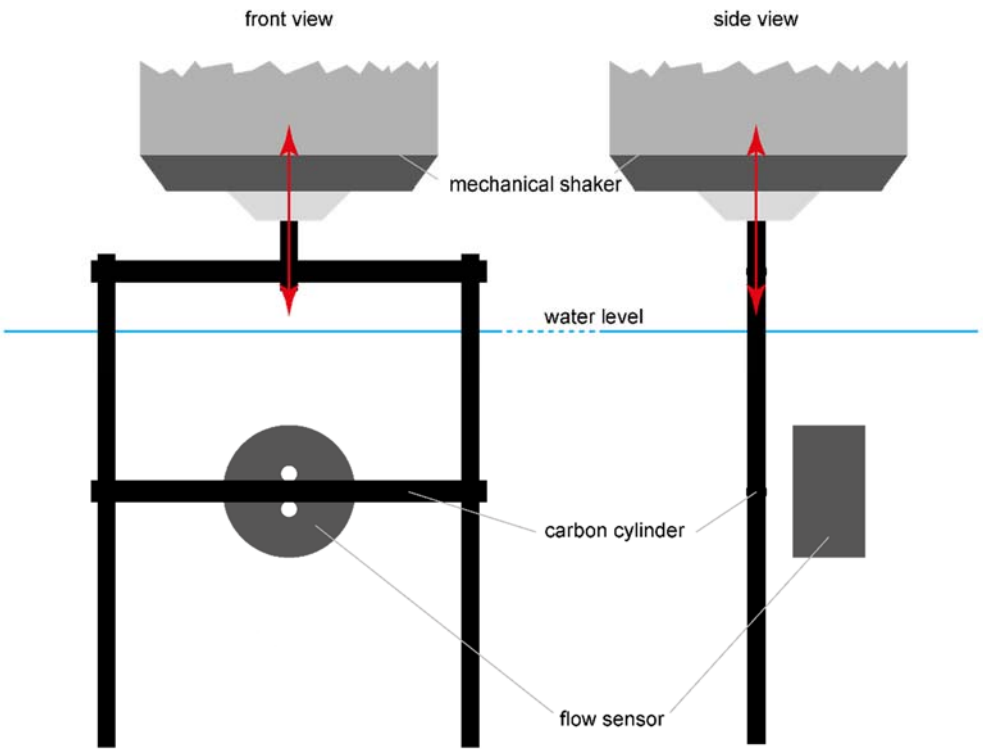

Fig. 3 Stimulus device Front and side view of the stimulus device and the ALL (flow sensor). A mechanical shaker vibrated a carbon cylinder that was suspended within a carbon frame. Red arrow: vibration direction. In most experiments, the carbon rod was positioned between the two sensor openings at a horizontal distance of 5 mm to the sensor surface. Dimensions are not to scale.

2.3. Canal

To test the influence of the canal dimensions, canal pieces of different length (2.8, 5.3 and 10.0 mm) and diameter (7.0, 3.7 and 2.0 mm) were mounted between a front plate that was fixed in the experimental tank and the flow sensor (c.f. Fig. 4). The temporal filter properties were measured according to the method described in section 2.2.2. Measurements were repeated 3 times for each canal piece and the results were averaged. The lengths as well as the diameters of the canal pieces were chosen to be in a constant ratio of 1.87 between one and the next bigger size. The vibrating cylinder was positioned 5 mm away from a fixed front plate that held the canal adapter plates and the sensor. Front plate and vibrating cylinder remained at the exact same position throughout the entire experiment.

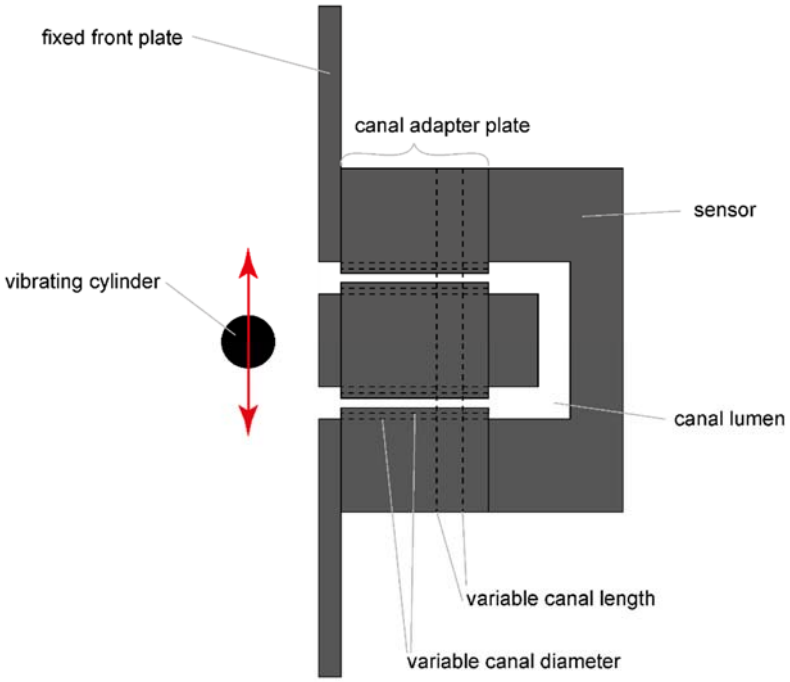

Fig. 4 Setup to test the influence of different canal dimensions Schematic cross section. The vibrating cylinder was positioned 5 mm away from the front plate. Canal adapter plates with variable canal length and diameter were mounted between this front plate and the sensor. Dimensions are not to scale.

2.4. Pores

2.4.1. Inter-pore distance

To test how the spatial resolution of the sensor was influenced by the inter-pore distance (IPD), three adapter plates with different IPDs (16, 28 and 40 mm, Fig. 5a) were mounted in front of the sensor. The cylinder was moved on a vertical transect parallel and 10 mm away from the surface of the sensor. The starting position was right between the pores. The cylinder was moved upwards in 1 mm steps for a total of 8 cm. At each position, a dipole stimulus (2 s, 15 Hz) was applied while ALL and the acceleration sensor signals were recorded. The measurements were repeated 3 times for each adapter plate and the results were averaged. The sensitivity of the ALL was calculated (c.f. 2.2.2) and plotted against the cylinder position. The resulting response profiles reflect the spatial response of the sensor with a given IPD.

2.4.2. Pore diameter

The influence of the pore diameter was tested by mounting adapter plates with various pore diameters (0.27, 0.45, 0.85, 1.17 and 4 mm; c.f. Fig. 5b). The

number of pores per sensor opening was adjusted according to the Hagen-Poiseuille equation to ensure a constant hydrodynamic resistance across all tested adapter plates. Otherwise, for instance, a single pore of 0.27 mm in diameter would have had blocked almost all of the signal, not allowing measurements at this pore diameter. In a control experiment, the influence of the hydrodynamic resistance was tested by mounting an adapter plate with a pore diameter of 0.85 mm but with 6 times more pores (18 vs. 108 pores). The cylinder was positioned 5 mm away from the pore adapter plates right between the sensor openings. The temporal filter properties were measured as described in section 2.2.2. The measurements were repeated 3 times for each adapter plate and the results were averaged.

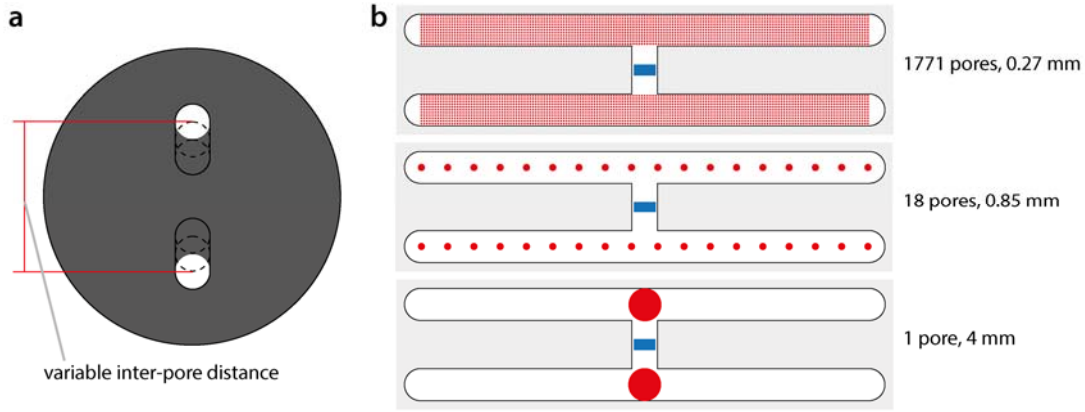

Fig. 5 Inter-pore distance and pore diameter adapter plates (**a**) Schematic drawing of the adapter plate that was mounted in front of the flow sensor to adjust the IPD. Pores were drilled into a long slot resulting in IPDs of 16, 28 and 40 mm. (**b**) Schematic pore configurations of three exemplary adapter plates that were mounted in front of the sensor to test the influence of the pore diameter. Due to spatial restrictions the pores were distributed along elongated side canals that were connected to the sensor openings. Blue rectangles mark the neuromast position. Fluctuating water flow was from the pores at one side, across the neuromast and towards the pores at the other side of the neuromasts. Dimensions are not to scale.

2.5. Membranes

2.5.1. Temporal filter properties

Membranes of either different tension (loose, medium, tight), diameter (13, 10 and 7 mm) or thickness (1.2, 0.8, 0.6 and 0.4 mm) were mounted in front of the sensor openings by means of adapter plates and the temporal filter properties were measured. The membranes used in the tension and diameter experiments were manufactured from 0.055 mm thin latex membranes. The membranes were first loosely attached to the adapter plates with the outer fixing ring and then

tensioned with the inner tensioning ring (c.f. Fig. 7, top). Different heights of the fillets on the tensioning ring resulted in different membrane tensions (loose, medium, tight; we did not quantify the tension). We altered the diameter of the pores over which the membranes were suspended to obtain different membrane diameters. To create membranes of different thickness, the adapter plates were placed front-down on a flat silicone pad. Different amounts of two-component-silicone were injected inside the pores of the adapter plates (c.f. Fig. 7, bottom). After the silicone was hardened, the adapter plate was carefully stripped of the silicone pad. The casted membranes remained inside the pores of the adapter plates. Temporal filter properties were measured according to section 2.2.2 while the cylinder was positions 5 mm away from the membrane adapter plates at a vertical level right between the sensor openings. Measurements were repeated 3 times for each membrane and the results were averaged. For comparison, the temporal filter properties were also tested with adapter plates that did not contain any membranes.

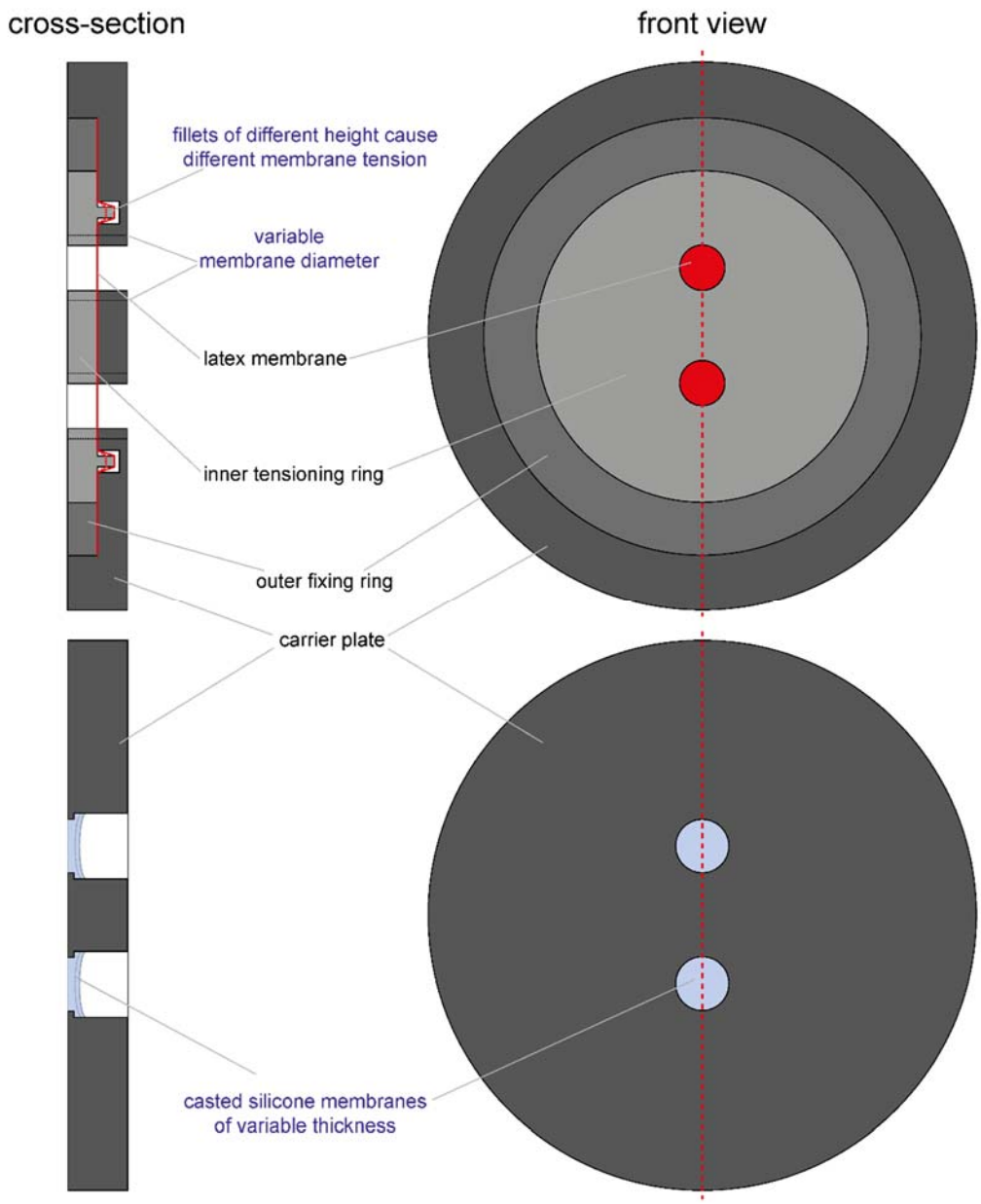

Fig. 6 Membrane adapter plates Schematic cross sections and front views of the adapter plates containing membranes of different diameter or membrane tension (top) and of different thickness (bottom). In the former, a thin latex membrane was fixed between the outer fixing ring and the carrier plate. The inner tensioning ring had fillets of different height causing different membrane tensions. In the latter, the variable membrane thickness was achieved by casting the membranes from different amounts of silicone.

2.5.2. Detection of Kármán vortex streets

The sensor was placed inside a flow tank to measure the alternating pressure fluctuations of a Kármán vortex street (c.f. Fig. 7). The vortex streets were generated by placing a D-shaped half cylinder in the laminar flow. The diameter of the cylinder was varied (1, 2 and 3 cm) resulting in different vortex shedding frequencies. The vortex shedding frequency (VSF) of a Kármán vortex street

depends on the diameter of the cylinder (d). It can be calculated according to (Vogel, 1996; Chagnaud et al., 2007):

$$VSF = \frac{St \cdot U}{d} \tag{2}$$

where St = the dimensionless Strouhal number = 0.2 (for D-shaped half-cylinder placed water, Vogel 1996) and U = actual flow velocity around the cylinder. U was calculated according to Liao et al. (2003):

$$U = U_f \frac{W}{W - d} \tag{3}$$

with U_f = laminar flow velocity in the absence of a cylinder = 11 cm/s and W = width of the flow tank = 20 cm. The sensor was positioned 10 cm downstream of the cylinder; the sensor front was at the lateral level of the edge of the half-cylinder. The root mean square (RMS) amplitude of a 60 s flow sensor signal was used to quantify the sensors sensitivity in a particular flow condition. The measurements were repeated three times and the results were averaged.

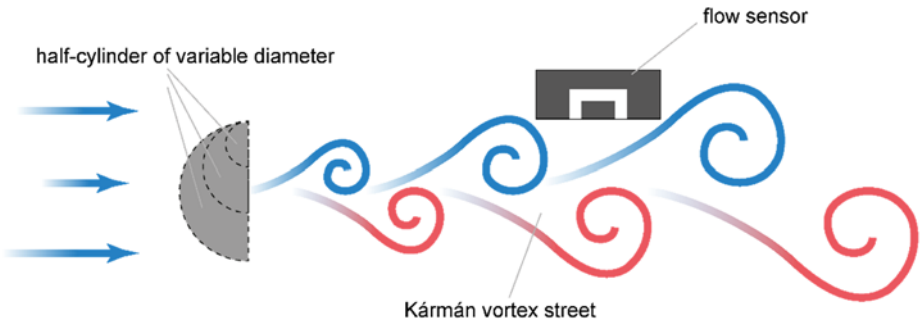

Fig. 7 Kármán vortex street detection Schematic top view of the Kármán vortex street setup. The flow sensor was mounted downstream of a d-shaped half-cylinder inside a flow tank. Different diameters of the half-cylinder caused different vortex shedding frequencies.

2.6. Fluids

To examine the influence of the canal fluid the sensor had to be filled with fluids other than the tank water. For this purpose it was closed by an adapter plate containing a 0.5 mm thin silicone membrane, manufactured as described in section 2.5.1. Valves, tubing and syringes that were connected to the adapter plate allowed to exchange the fluid inside the sensor. Solutions of various concentrations of sodium chloride (300, 200 and 100 g/l) and sucrose (500, 333.3 and 166.7 g/l) were injected into the sensor. The Viscosity (1.91, 1.47 and 1.18 $kg*m^{-1}*s^{-1}$ for sodium chloride and 7.56, 3.14 and 1.63 $kg*m^{-1}*s^{-1}$ for sucrose) and

density (1.18, 1.11 and 1.05 $kg*l^{-1}$ for sodium chloride and 1.19, 1.12 and 1.07 $kg*l^{-1}$ for sucrose) of the solutions was calculated according to literature (Ozbek et al., 1977; Kestin et al., 1981). The starting point for the choice of the applied concentrations was the maximum concentration of sodium chloride (300 g/l) being relatively close to its maximum solubility in water (359 g/l). Subsequently, the concentrations of sucrose were chosen to ensure comparable densities across the sodium chloride and sucrose solutions (c.f. Fig. 14b, left-bottom).

The cylinder was positioned 5 mm away from the sensor at a vertical position right between the sensor openings. The temporal filter properties were measured according to section 2.2.2 while. The measurements were repeated 3 times for each canal fluid and concentration, the results were averaged.

3. Results

3.1. Silicone bar

3.1.1. Resonance frequency

The method of measuring the resonance frequency by video tracking a rebounding silicone bar revealed reliable results (error >2%). The silicone bars oscillated with a constant frequency. The oscillation decayed (c.f. Fig. 8a) until the silicone bar finally rested in its initial, upright position. The damped, single degree of freedom oscillator equation fitted the observed oscillation well (R^2 >0.97). Thicker as well as shorter bars showed a higher resonance frequency than thinner respectively longer bars (c.f. Fig. 8b, top). For instance, the resonance frequency (in air) increased from about 32 to 93 Hz when the thickness increased from 75 to 125 µm. It decreased from about 304 to 93 Hz when the length increased from 1 to 3 mm. The resonance frequency of a specific bar was always lower when it was submerged (approx. 1/3 of the resonance frequency in air). The period of time in which the oscillation decayed, decreased with increasing thickness respectively decreasing length of the silicone bar. This is reflected by an increased decay constant (c.f. Fig. 8b, bottom). Under water, the decay constant was always higher than in air.

3.1.2. Temporal filter properties

The flow sensor can be described as a low pass filter with a distinct resonance peak (c.f. Fig. 8c). Measuring the frequency response profiles of the sensor equipped with silicone bars of different length and thickness revealed that the sensor's resonance peak systematically corresponded to the resonance frequency of the silicone bar. However, the resonance peak was always about 5 Hz lower than the resonance frequency of the silicone bar measured with the high speed camera (indicated by black arrows in Fig. 8c). The sensitivity of the sensor systematically correlates with the length of the silicone bars: within the test range, longer silicone bars resulted in a higher sensitivity across most frequencies (Fig. 8c, right). Although not as distinct, the relation of thickness and sensitivity was systematic, too: At most frequencies, the 125 µm thick bar resulted in the highest sensitivity, followed by the 100 and the 75 µm thick bars (Fig. 8c, left). Around 80 to 90 Hz, the sensor responded with a small but still distinct

resonance peak, no matter which type of silicone bar was installed. This peak was also present in all following experiments. It was traced back to being a stimulus artefact due to the resonance frequency of the aluminum rack on which the mechanical shaker was suspended.

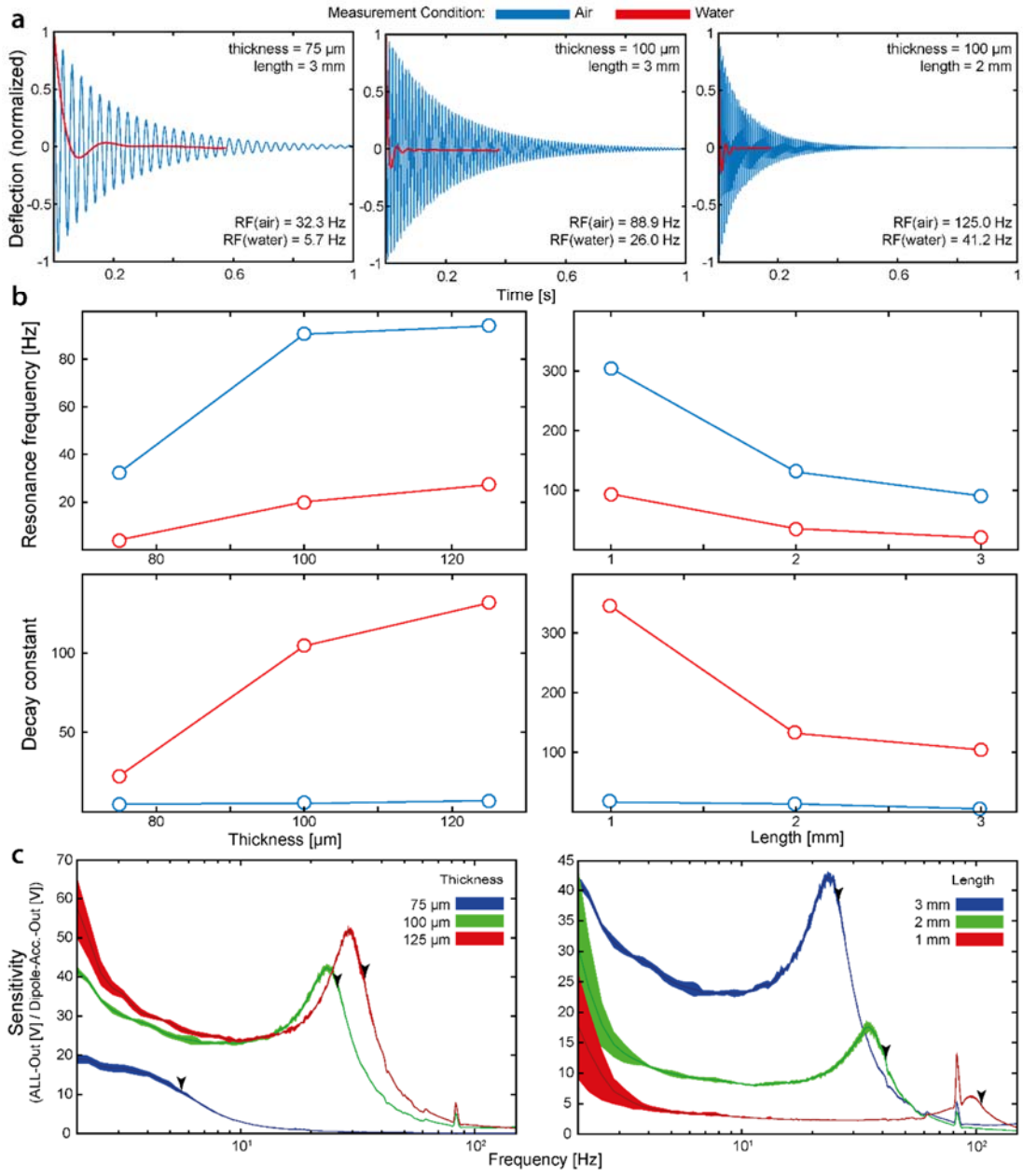

Fig. 8 Influence of thickness and length of the flexible silicone bar A high speed camera was used to examine the resonance frequency of the silicone bar. (**a**) Decaying oscillation in air (blue) and water (red) of three exemplary silicone bars. Increasing the thickness of the bar (from left to center) or decreasing its length caused an increase in resonance frequency and decay constant (faster decay). (**b**) Resonance frequencies (top) and decay constants (bottom) of all tested bars of different thickness (left) and length (right) in air (blue) and water (red). (**c**) Frequency response profiles of the sensor equipped with silicone bars of different thickness (left) and length (right). Sensitivity is plotted as function of stimulus frequency. Sensitivity was is defined as the flow sensor output voltage divided by the output voltage of the acceleration sensor that was mounted inside the dipole source. Thickness of graphs: standard deviation across repetitive measurements (n=3). Thickness and length of bars are color coded. Black arrowheads indicate the resonance frequencies of the mounted silicone bars.

3.2. Canal

The sensitivity of the sensor was influenced when additional canal sections were mounted: longer or narrower canal sections led to a decrease in sensitivity across all frequencies (Fig. 9). However, the magnitude of the influence of diameter and length was different: decreasing the diameter by a factor of 3.5 (from 7 to 2 mm) led to a decrease in sensitivity of approx. 60 % while increasing the canal length by the same factor (from 2.9 to 10 mm) led to a decrease in sensitivity of about 20 %. Within the test range, the variations of canal length and canal diameter did not influence the resonance frequency or the shape of the frequency response profiles.

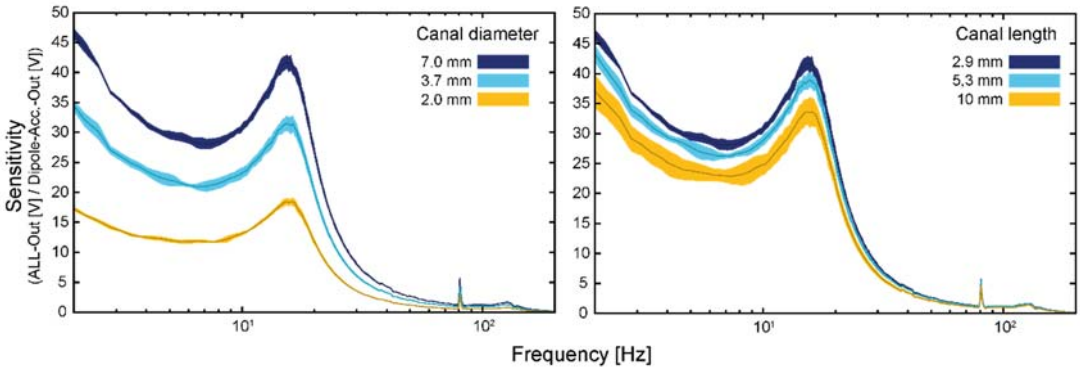

Fig. 9 Influence of canal diameter and length Frequency response profiles of sensors with canal sections of different diameter (left) and length (right). Sensitivity is plotted against stimulus frequency. Thickness of graphs: the standard deviation across repetitive measurements (n=3). Diameter and length of canal sections are color coded.

3.3. Pores

3.3.1. Inter-pore distance

The vibrating cylinder was moved on a transect parallel to the surface of the sensor to determine the spatial response of the sensor. At the shortest IPD (16 mm) the strongest responses were recorded when the cylinder was positioned at the center of the sensor (0 cm, Fig. 11a). When the cylinder was moved away from the sensor the responses first diminished, then increased up to a local maximum and finally decreased again. Increasing the IPD resulted in wider response profiles. The position, at which the sensor signal diminished as well as the local maximum moved further away from the center of the sensor when the IPD was increased. At an IPD of 40 mm the maximum response was not right at the center but slightly shifted to the side. The maximum response decreased

with increasing IPD. In contrast, the local maxima at the sides was higher at IPDs of 40 and 28 mm compared to 16 mm.

Although the presented experiments were conducted only at one side of the sensor (cylinder positioned at and above the center of the sensor, not below), we also tested the spatial response at both sides. These tests revealed that the spatial response profiles were symmetrical across both sides of the sensor.

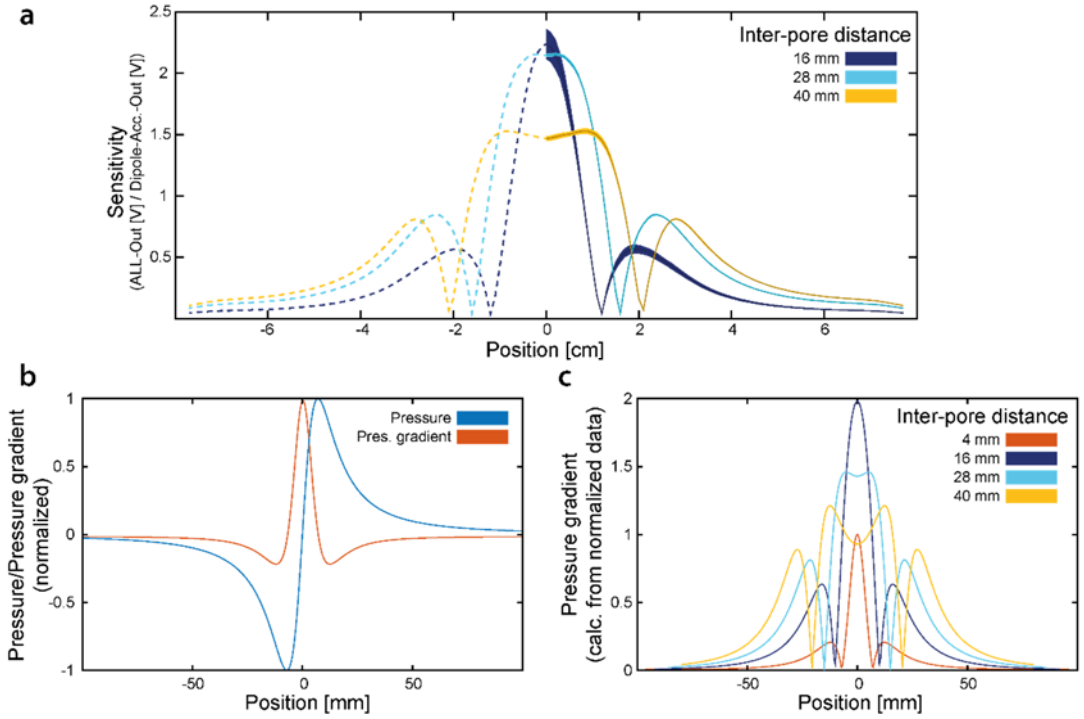

Fig. 10 Influence of inter-pore distance (**a**) Spatial response profile obtained by stimulating the flow sensor along a linear transect parallel to the surface of the sensor. Sensitivity is plotted as function of the dipole source position (0 cm is at the center of the sensor). Thickness of graphs: standard deviation across repetitive measurement (n=3). IPD is color coded. Solid lines: measured data. Dashed lines: mirrored solid lines, added for better visualization of the symmetric receptive fields. (**b**) Calculated pressure (blue) and pressure gradient (red) caused by a vibrating object. Positions correspond to the experimental conditions. (**c**) Calculated pressure difference between pores of variable IPD.

3.3.2. Pore diameter

Although the number of pores was adjusted to ensure equal hydrodynamic resistance across all of the tested adapter plates (c.f. 2.4.2), the average sensitivity across all frequencies slightly varied with no systematic correlation with the pore diameter. This possibly was due to fabrication tolerances of the adapter plates. For better comparison, the response profiles were normalized to their particular resonance peak (Fig. 11, left). The general shape of the frequency response profiles was similar in all of the tested pore configurations and resembled the previous experiments: a resonance peak was observed at around

15 Hz, while low pass filter characteristics lead to decreasing sensitivity up to about 80 Hz. However, the resonance peak frequency slightly shifted towards higher frequencies when the pores were narrower. For instance, the resonance peak was at 14.44 Hz with 4 mm pores. It was at 14.75 Hz when 0.27 mm pores were installed. The differences were minuscule, but the relation between pore size and resonance peak frequency was systematic (c.f. Fig. 11, left, inset). The normalized data was then plotted in proportion to the response of the sensor equipped with 0.85 mm pores (Fig. 11, right). The resulting graphs reveal that the sensor was less sensitive to high frequencies and more sensitive to low frequencies when the pore diameter was increased and vice versa.

In a control experiment the sensor was equipped with pores of identical diameter (0.85 mm) but with 6 times more pores (resulting in decreased hydrodynamic resistance). Only small differences were observed in the particular response profiles (Fig. 11, right). We thus suggest that the systematic tendencies observed in the experiment were – in fact – caused by the pore diameter and not by other parameters such as the number of pores or differences in the hydrodynamic resistance.

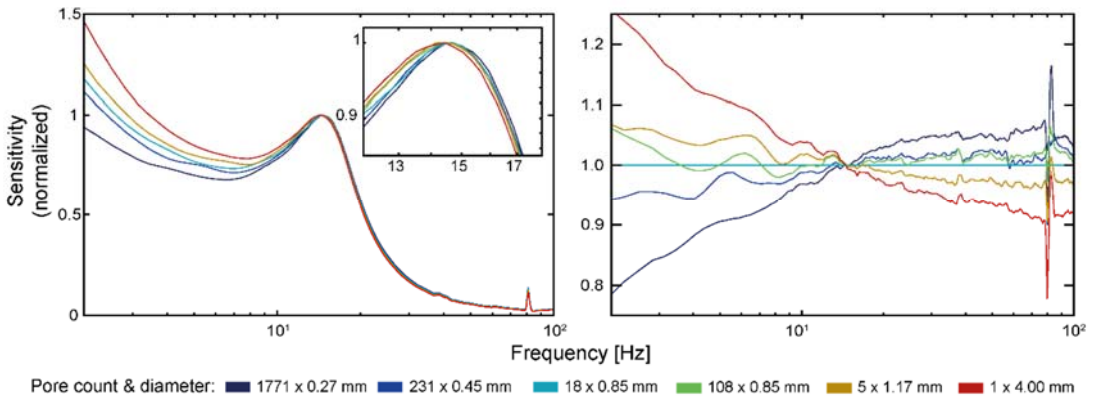

Fig. 11 Influence of pore diameter Frequency response profiles of sensors equipped with pores of different diameter. (left) Graphs are normalized to the resonance peak amplitude. The inlet gives a more detailed view of the resonance peak. For clarity, standard deviation across repetitive measurements (n=3) is omitted. (right) Graphs now plotted in proportion to the response of the sensor equipped with pores of 0.85 mm diameter.

3.4. Membranes

3.4.1. Temporal filter properties

When no membrane was attached, the frequency response profile of the sensor resembled the frequency response profiles measured in previous experiments. The

resonance peak occurred at about 12 Hz. Low pass filter characteristics led to a decrease in sensitivity up to about 30 Hz (c.f. Fig. 12, red graph). Covering the pores with a membrane resulted in an additional resonance peak. For instance, when a loosely tensioned membrane was attached, an additional resonance peak was observed at approx. 2.5 Hz (c.f. Fig. 12, top, blue graph). The sensitivity at this frequency even exceeded the sensitivity of the sensor when no membrane could obstruct the water flow through the pores (c.f. Fig. 12, top, compare blue and red graph). Increasing membrane tension systematically effected the additional resonance frequency: the higher the membrane tension, the higher the additional resonance frequency. A similar systematic relation applied for the membrane diameter and thickness: The smaller respectively thicker the membrane, the higher the additional resonance frequency of the sensor. When the sensor's resonance frequency (due to the resonance of the silicone bar) and the additional resonance frequency (caused by the resonance of the membrane) were similar, the resonance peaks fused to a prominent single peak (c.f. Fig. 12, top, green graph). Of course, adding a membrane did not increase the sensitivity at all frequencies: at frequencies further away of the membrane's resonance frequency the sensitivity of the sensor was attenuated compared to the sensor without a membrane (c.f. Fig. 13a, top, compare yellow and red graph).

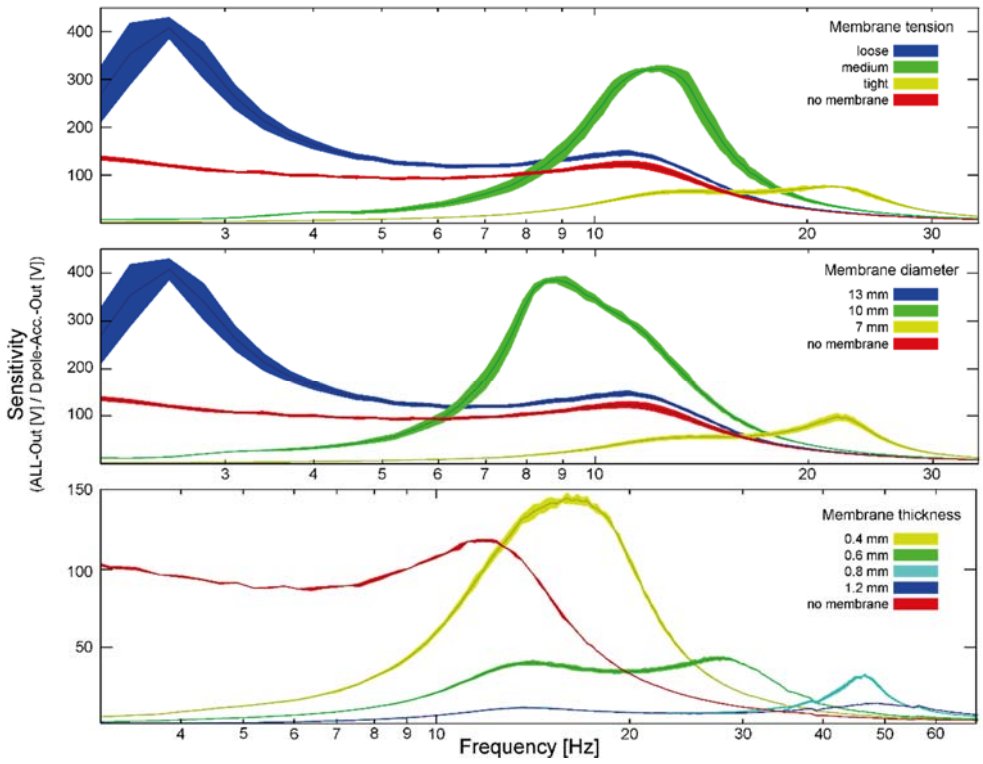

Fig. 12 Influence of membrane tension, diameter and thickness Frequency response profiles of sensors equipped with membranes of different tension (top), diameter (center), and thickness (bottom). Sensitivity as function of stimulus frequency. Thickness of the graphs: standard deviation of repetitive measurements (n=3). Membrane tension, diameter and thickness are color coded.

3.4.2. Detection of Kármán vortex streets

The membrane configuration influenced the performance of the sensor in detecting Kármán vortex streets. In all flow conditions the sensor responded weakest, when a tight membrane was installed. When the 3 and 2 cm cylinders were used to shed the vortex street, the sensor responded strongest, when no membrane was installed. In contrast, when the vortex street was shed with the 1 cm cylinder, the strongest response was observed when the loose membrane was installed (Fig. 13a).

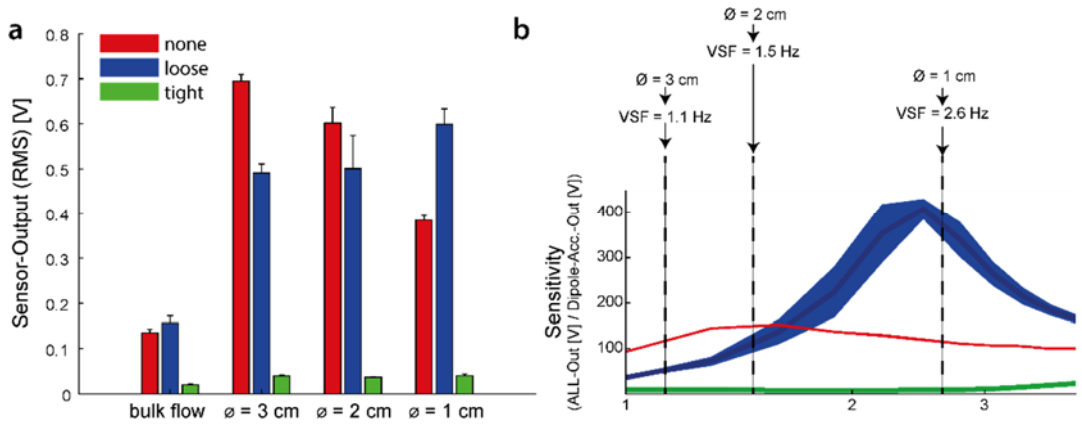

Fig. 13 Detection of Kármán vortex streets (**a**) RMS of the output voltage of a sensor that was exposed to a Kármán vortex street for 60 s. Vortex streets were shed by a 3, 2 or 1 cm diameter half-cylinders. Bulk flow was tested when no cylinder was installed. The sensor was equipped with a tight, a loose and without a membrane (color coded). Error bars code for the standard deviation of individual measurements (n=3). (**b**) Frequency response profile of the sensor equipped with the different membranes (same color coding as in **a**). Dashed lines indicate the vortex shedding frequencies of the respective half-cylinders.

3.5. Fluids

The frequency response profiles of the sensor filled with sodium chloride or sucrose solutions of different concentrations were similar in shape (Fig. 14a). In this experiment a membrane was used to retain the canal fluid. However, only one prominent resonance peak was present at around 20 Hz. We thus suggest that the resonance frequency of the membrane and the silicone bar were similar, resulting in a single resonance peak. To analyze the influence of the canal fluid we determined the frequency and the amplitude of this resonance peak (c.f. Fig. 14b). The experiments showed that the resonance peak amplitude decreased with increasing sodium chloride or sucrose concentrations. This decrease was steeper for the sucrose compared to the sodium chloride solutions (Fig. 14b, center-top). Similarly, the resonance frequency decreased with increasing concentration. The decrease was again slightly steeper for the sucrose solutions (Fig. 14b, center-bottom). Note that the results will be discussed in regard to the viscosity and density of the fluids later.

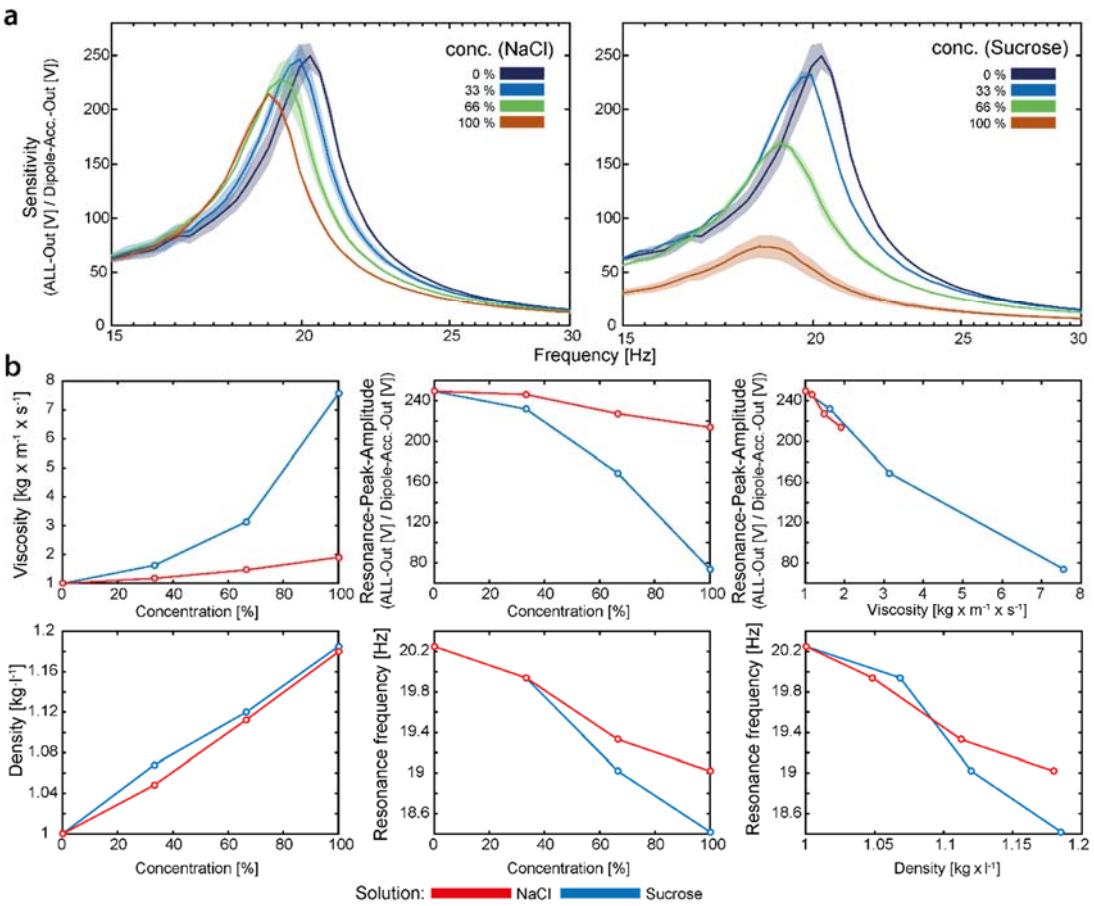

Fig. 14 Influence of canal fluids (**a**) Frequency response profiles of the flow sensor filled with sodium chloride (left) and sucrose (right) solutions of different concentrations. Color coded concentrations are given in proportion to the maximum concentration used. The thickness of the graphs codes for standard deviation across individual measurements (n=3). (**b**) Viscosity and density of the sodium chloride (red) and the sucrose (blue) solutions as function of the concentration (left, top and bottom). Resonance peak amplitude and frequency as function of the concentration (center, top and bottom). Resonance peak amplitude as function of the viscosity (top-right). Resonance peak frequency (bottom-right) as function of the density of the canal fluid.

4. Discussion

4.1. Silicone bar

4.1.1. Resonance frequency

The r^2-values of the fit functions (>0.97) indicate that the damped single degree of freedom oscillator equation (eq. (1); c.f. 2.2.1) was sufficient to describe the oscillating movement of the silicone bar.

In such oscillating systems, the natural resonance frequency (f_n) depends on the system properties mass (m) and stiffness (k) according to:

$$f_n * 2\pi = \sqrt{\frac{k}{m}} \tag{4}$$

The resonance frequency increases, when the stiffness of the silicone bar disproportionally increases compared to its mass. Both, increasing the thickness of the bar as well as decreasing its length might have had this effect (c.f. Fig. 8b, top).

The oscillation of the silicone bar was damped by friction: On the one hand by its inner friction, on the other hand by frictional forces from the surrounding fluid (air or water). Damping causes the exponential decay of the oscillation. It can be quantified by the decay constant. Water has a much higher viscosity than air, resulting in higher frictional forces and thus higher decay constants. This was observed in the present study (c.f. Fig. 8b, bottom).

The decay (constant) did not only increase when the bar was submerged in the fluid. In addition, it increased with increasing bar thickness or a decrease in bar length (c.f. Fig. 8b, bottom). The reason for this might in part be an increase of inner friction. However, it is mainly caused by the increase of the resonance frequency: In each oscillation cycle the system lost a small amount of energy, resulting in the decay of the oscillation amplitude. At higher resonance frequencies this energy loss occurs more often per time resulting in a decreased decay duration, i.e. in an increased decay constant.

Last, in a damped oscillation process the resonance frequency (f_d) is determined by the natural (undamped) resonance frequency (f_n) and the decay constant (γ) according to:

$$f_d \cdot 2\pi = \sqrt{(f_n \cdot 2\pi)^2 - \gamma^2} \tag{5}$$

When the silicone bar was transferred into the water (causing an increased decay constant), the resonance frequency should hence decrease. In fact, this was observed in the experiments (c.f. Fig. 8b, top).

4.1.2. Temporal filter properties

CNs respond in proportion to the acceleration of the surrounding medium respectively the vibrating object (Denton & Gray, 1983). Therefore it is appropriate to express sensitivity of the ALL by calculating the ALL response in proportion to the acceleration of the vibrating object (Kalmijn, 1988), respectively in proportion to the response of the acceleration sensor.

The temporal filter properties of the flow sensor not only depend on the properties of the silicone bar, but also on the canal system. Thus, to explain the frequency response profiles of the sensor equipped with different types of silicone bars it is also important to take into account the influence of the canal.

Before outside pressure fluctuations are detected by the artificial neuromast they are propagated along the canal. In terms of sensitivity (as defined above), the canal acts as a first order low-pass filter (van Netten 2006). In fact, the measured frequency response profiles reflect the low-pass filter characteristics of the canal: sensitivity decreases with increasing frequencies until it diminishes at about 100 Hz (c.f. Fig. 8c). A distinct resonance peak was superimposed on the low-pass filter response. The systematic correlation of the frequency of this resonance peak and the resonance frequency of the particular silicone bar (measured with the high speed camera) suggests, that the resonance of the sensor is caused by the resonance of the silicone bar.

The resonance frequency of the sensor was always about 5 Hz lower than the resonance frequency of the silicone bar (measured with the high speed camera). This was due to the superposition of the resonance peak and the constantly decreasing low-pass filter response, shifting the resonance peak towards lower frequencies.

Longer bars are less stiff than a shorter bar. Thus, they are deflected more by a given canal fluid velocity than a shorter bar. A sensor that is equipped with a longer silicone bar should therefore be more sensitive. As expected, longer silicone bars caused a higher sensitivity across all frequencies.

Thinner silicone bars are less stiff as well and should therefore increase the sensitivity of the sensor, too. Contrarily, thinner silicone bars led to a decrease of sensitivity. We assume that thinner bars limited the amount of light that was guided towards the position sensitive photo diode and therefore decreased the sensitivity of the sensor.

4.2. Canal

Altering the diameter and length of an additional canal section influenced the average sensitivityof the sensor across all frequencies while the temporal filter properties (shape of the frequency response profile) did not change significantly (c.f. Fig. 9). The canal system of the ALL can be approximated as a cylindrical pipe with a particular hydrodynamic resistance. The volumetric flow rate ($\dot{V}$) can be calculated by the Hagen-Poiseuille equation:

$$\dot{V} = \frac{\pi \cdot r^4 \cdot \Delta p}{8 \cdot \eta \cdot l} \tag{6}$$

Given a fixed pressure difference (Δp) and a particular fluid viscosity (η), the flow rate increases with the fourth power of the pipe's radius (r) and is inversely proportional to its length (l). As the flow rate inside the canal is the factor that determines the deflection of the bar, the radius as well as the length of the canal should effect the sensitivity of the canal. In fact, increasing the radius led to an increase, increasing the length of the canal led to a decrease of sensitivity. The radius of the canal also had a bigger influence than its length, as expected.

4.3. Pores

4.3.1. Inter-pore distance

The spatial response profile we observed by moving the vibrating object on a linear transect (Fig. 10a) is referred to as the "Mexican hat" and has been described several times (Coombs et al., 1996; Yang et al., 2010; Klein & Bleckmann, 2011). To explain the Mexican hat it is necessary to understand the

spatial properties of the pressure field around a vibrating object (sphere). The dipole pressure field around a vibrating object can be calculated according to (Coombs et al., 1996):

$$P = ((\rho 2\pi f a^3 U)/2r^2) \cdot \cos\theta \quad (7)$$

where ρ = fluid density = 1 kg/l, f = vibration frequency = 15 Hz, r = distance from the point of interest to the source center, θ = angle to the axis of oscillation (0°), and a = source radius = 10 mm. A solution of the equation for the stimulus positions used in the experiment is depicted in Fig. 10b. The source oscillation amplitude (U) was arbitrarily set to 1 m/s. The blue graph indicates that the pressure is increased in front (positive position) and decreased behind (negative position) the vibrating object (with respect to the vibration direction). CNs as well as artificial neuromasts respond in proportion to the pressure gradient between adjacent pores. The IPD of a biological lateral line is small (few millimeters) compared to the dimensions of the exemplary pressure field. The spatial response profile of a CN can thus be approximated with the first derivative of the pressure (red graph). However, the IPDs of our sensor were much bigger. We calculated the pressure difference between the pores on the basis of the pressure field shown in Fig. 10a to model the spatial response profiles for the IPDs 4, 16, 28 and 40 mm (Fig. 10c). The calculated profiles resemble the measured response profiles (c.f. Fig. 10a). They demonstrate that the maximum response increases with increasing IPD (4 and 16 mm, Fig. 11c) as long as the IPD does not exceed the distance between the maximum and the minimum peak of the pressure field (Fig. 10b, blue graph). If the IPD is increased beyond this distance, the maximum response decreases and a double peak shape occurs (28 and 40 mm, Fig. 10c). The response diminishes, when the pores are located at positions of equal pressure, i.e. at one and the other side of the maximum or the minimum peak of the pressure field (c.f. Fig. 10b, blue graph). The distance between the local maxima respectively the positions at which the response diminishes increases with increasing inter-pore interval due to the asymmetric shape of the maximum and the minimum peak of the pressure field.

The measured as well as the calculated data show that the IPD influences the spatial response of the sensor. Depending on the dimensions of the pressure field

and the position of the sensor, increasing or decreasing the IPD can lead to increased responses.

4.3.2. Pore diameter

We already examined that the canal system acts as a low-pass filter leading to a decrease of sensitivity with increasing frequencies. The cut-off frequency of this first-order low-pass filter can be calculated according to (Schlichting & Gersten, 2004; van Netten, 2006):

$$f_{cut} \cong 5\mu/(2\pi\rho R^2) \tag{8}$$

where μ = the viscosity of water = 1.0 mPa*s, ρ = the density of water = 1 kg/l and R = the radius of the canal. The cut-off frequency of the canal system in the ALL ($R = 3.5$ mm) is 0.065 Hz. This means that the stimulus frequencies we applied (>2 Hz; due to technical limitations of the mechanical shaker) were beyond the cut-off frequency of the canal. Even in the previous experiments, where we used canal sections with a diameter of 3.7 and 2 mm (R = 1.75 and 1 mm, the theoretical cut-off frequencies (0.233 respectively 0.796 Hz) were below the applied stimulus frequencies. In contrast, in the biological lateral lines the (much smaller) canal diameter and the resulting cut-off frequency has to be considered in terms of the temporal filter characteristics. For instance, in the ruffe (*Gemnocephalus cernuus*), the diameter of the cephalic lateral line canals is about 1 mm. In addition, the viscosity of the canal fluid is increased (compared to water). In sum, the cut-off frequency of the cephalic lateral line canals of the ruffe is about 20 Hz (van Netten, 2006).

To investigate the effect of the canal diameter on the temporal filter properties of our flow sensor, we varied the diameter in only a short and the most peripheral section of the canal: the pores. The aim was to test whether the pores alone are sufficient to shapes the frequency response of the sensor. The theoretical cut-off frequencies at the tested pore diameters were 0.199 Hz at 4 mm, 2.326 Hz at 1.17, 4.406 Hz at 0.85 mm, 15.719 Hz at 0.45 mm and 43.664 Hz at 0.27 mm diameter pores. The present experiment showed that the sensor was more sensitive to high frequencies when the pore diameter was small (c.f. Fig. 11). However, the effect was minuscule. This was expected as the pores are only a short section of the entire canal system.

The resonance frequency was slightly shifted towards higher frequencies when the pores were small. This was due to the superposition of the resonance of the silicone bar and the cut-off filter properties of the sensor. A steeper low-pass filter shifts the resonance peak towards lower frequencies.

4.4. Membranes

4.4.1. Temporal filter properties

Our experiments revealed that oscillatory pressure fluctuations were still detected by the ALL when the pores were covered by a flexible membrane (Fig. 12). The membrane caused an additional resonance peak in the frequency response profiles. Compared to the sensor without membrane, the sensitivity around the additional resonance frequency was increased. At frequencies further away, membranes led to a decrease of sensitivity. These results is in agreement with theoretical assumptions and empirical data of previous studies (Denton & Gray, 1988).

To explain the results we have to consider the physical properties of a membrane: Like the silicone bar, a flexible membrane that is suspended across the pores acts as a single degree of freedom oscillator. The natural resonance frequency of the membrane is determined by the system parameters mass and stiffness (eq. (4); c.f. 4.1.1). Both parameters are influenced by the membrane tension, diameter or thickness.

For instance, increasing the tension of the membrane leads to an increase in stiffness and thus to an increase in the membrane's resonance frequency. In fact, the resonance peak frequency shifted towards higher frequencies when the membrane tension was increased (c.f. Fig. 12, top).

When the diameter of the membrane is increased, its stiffness decreases (similar to the decrease of stiffness of the silicone bar with increasing length). Consequently, it was expected that the resonance frequency of the membrane respectively the resonance peak frequency of the sensor decreased with increasing membrane diameter (c.f. Fig. 12, center).

Increasing the thickness of the membrane leads to an increase in both, stiffness and mass. This is comparable to the increase of the thickness of the silicone bar.

The additional resonance peak shifted towards higher frequencies, when the thickness of the membrane was increased (c.f. Fig. 12, bottom). Hence, we assume that the stiffness of the membrane increased disproportionally to its mass.

4.4.2. Detection of Kármán vortex streets

The sensor was equipped with different membrane configurations and the performance in detecting Kármán vortex streets was tested. The aim was to examine the significance of the frequency response profiles (obtained with a sine sweep stimuli) for complex measurement tasks.

In fact, the performance of the sensor in detecting a specific vortex street (c.f. Fig. 13a) corresponded to the frequency response profiles (c.f. Fig. 13b). For vortex shedding frequencies of 1.1 respectively 1.5 Hz (i.e. if the vortex street was shed with a 3 or 2 cm cylinder) the frequency response profiles predict the strongest response, when no membrane is attached. For a vortex shedding frequency of 2.6 Hz (1 cm cylinder) the frequency response profiles predicts the strongest response for the sensor equipped with the loose membrane. Both predictions eventuated in the experiment (Fig. 13a).

4.5. Fluids

Although multiple fluid parameters are varied by changing the concentration of sucrose and sodium chloride in the canal fluid (e.g. electrical conductivity or the refractive index), viscosity and density are the most important parameters in terms of hydrodynamics.

Viscosity exponentially increased with the concentration of the solutions (c.f. Fig. 14b, top-left). Density linearly increased with the concentration of the solutions (c.f. Fig. 14b, bottom-left). The resonance peak amplitude was exponentially, negatively correlated with the concentration (the higher the concentration, the weaker the response; c.f. Fig. 14b, top-center), whereas the resonance frequency was linearly, negatively correlated with the concentration (c.f. Fig. 14b, bottom-center). When the resonance peak amplitude was finally plotted as function of viscosity, a negative linear relationship was apparent for both types of solution (c.f. Fig. 14b, top-right). A negative linear relationship was also observed when the resonance peak frequency was plotted as function of

density, (c.f. Fig. 14b, bottom-right). Hence, we suggest that the resonance peak amplitude is mainly influenced by the fluid's viscosity while that the resonance frequency is mainly influenced by the density of the fluid.

The resonance peak amplitude and frequency were arbitrarily extracted to quantify the sensor properties. Of course, it is likely that the fluid effects the sensor in various ways and across all stimulus frequencies. For instance, according to the Hagen-Poiseuille equation, the fluid viscosity determines the hydrodynamic resistance of the canal system. This should lead to decrease of sensitivity over all frequencies. The damping of the silicone bar is influenced by the fluid viscosity and density as well. The damping in turn effects the resonance frequency of the bar (c.f. 4.1.1). Also the cut-off frequency of the canal is influenced by both, the viscosity and the density of the canal fluid. We cannot comprehensively determine, to which degree the depicted mechanisms contribute to the changes in the frequency response profile obtained in the experiment.

4.6. Summary & Conclusion

The present study investigates the form-function relationship of individual components (form) and the performance (function) of the ALL.

We demonstrated that the resonance frequency of the silicone bar determines the resonance frequency of the ALL. The thickness and the length of the bar both influence the sensor's resonance frequency as well as the overall sensitivity.

Both, canal length and canal diameter, turned out to influence the overall sensitivity of the sensor. However the canal diameter is the more crucial parameter. It should thus be addressed in the first place to increase sensitivity in a potential future task. In turn, adding a bottleneck canal section with a small diameter could be a simple method to decrease sensitivity when the sensor is overstimulated.

The IPD had a clear impact on the spatial response of the sensor. The dimensions of the hydrodynamic signals have to be considered when the IPD is determined in a future sensor design. Furthermore, altering the pore diameter led to the expected influence on the temporal filter properties (small pores led to an increased cut-off frequency). However, the effect was weak and its applicability in the optimization of the sensor for a specific task is questionable.

The membranes turned out to preserve the functionality of the sensor in detecting oscillatory fluid motion. The experiments show how the tension, diameter and thickness of the membrane can be used to optimize the sensor, e.g. to detect a Kármán vortex street. In future tasks, membranes could be used to shield the sensor from solid particles. They also allow to use canal fluids other than the surrounding fluid.

Finally, we demonstrated the effect of different canal fluids on the performance of the sensor. For instance, using canal fluids less viscous than water might increase the sensitivity of the sensor in potential future applications.

II. ALL – Water surface waves

1. Introduction

1.1. Lateral Line

The lateral line system enables fish and most aquatic amphibians to sense weak water motions and pressure gradients (Coombs, 2002). It is essential for a variety of behaviors such as spatial orientation, prey detection, predator avoidance, schooling and intraspecific communication (for review see Bleckmann 1994). The smallest sensory unit of the lateral line system is the neuromast. It is composed of hundreds to thousands of mechanosensitive hair cells covered by a mucous cupula that extends into the water. Mechanical forces of the water deflect the cupula. The deflection is detected by the hair cells. There are two types of neuromasts: SNs (Fig. 1a) occur free standing on the skin and respond in proportion to water velocity. CNs (Fig. 1b) are located inside fluid filled canals that run parallel to the surface of the fish. The canal lumen is hydrodynamically connected with the surrounding water by pores located at each side of a CN. Pressure gradients between the pores lead to fluid motion inside the canal which in turn is detected by the CN. Consequently, CNs respond in proportion to the pressure gradient between adjacent pores (Kalmijn, 1988; Bleckmann, 1994).

1.2. Biomimetic flow sensors

Gathering flow information is not only important for aquatic animals, but also for many technical applications. The working principle of CNs has been implemented in a biomimetic flow sensor (Klein, 2009, 2012; Klein & Bleckmann, 2011; Klein et al., 2011). In this sensor, the artificial neuromast (Fig. 1c) was composed of three components: Like the neuromast, a transparent silicone bar (1) was positioned inside a fluid filled canal. It guided the light from a LED (2) towards a position sensitive photodiode (3) located at the opposite side of the canal. Fluid motion caused a deflection of the silicone bar which was detected by a position sensitive diode.

1.3. The cephalic lateral line of surface feeding fish

In the course of evolution the morphology, physiology and behavior of fish adapted to numerous aquatic habitats. Some fish species of the families Cyprinodontidae, Hemirhamphidae, Gaseropelecidae and Pantodonitidae have specialized on foraging at the water surface. Even when vision is poor, e.g. in the dark or in turbid water, surface feeding fish are able to detect and hence to strike towards terrestrial insects trapped at the water surface (Bleckmann et al., 1989*a*). The sensory system that enables this foraging strategy is the dorsal lateral line, especially the cephalic lateral line on the flattened head. When the fishes are hovering below the water surface, the cephalic lateral line neuromasts are in contact with the water surface (Schwartz, 1970). Surface feeding fishes are not only able to detect prey stimuli and to discriminate these stimuli from surface waves caused by abiotic wave sources like the wind (Bleckmann et al., 1981; Vogel & Bleckmann, 1997). Surface feeding fish can also determine the direction and the distance to a wave source. Thus, they can localize their prey (Bleckmann & Schwartz, 1982).

The anatomical properties of the cephalic lateral line (e.g. size and distribution of neuromasts) varies across different species of surface feeding fish (Schwartz, 1970, 1971). In most surface feeding fish the cephalic canal system is reduced and the lateral line neuromasts are in direct contact with the water surface. In *Pantodon buchholzi*, the lateral line organs are located in grooves that are covered by thin, flexible membranes. Only in *Fundulus notatus*, the cephalic canal system is still present (van Bergeijk & Alexander, 1962).

1.4. Detection of surface waves with an artificial lateral line

The goal of the present study was to test whether ALLs are suitable for the detection of water surface waves. We investigated how basic physical parameters such as the distance from the wave source, the frequency of the wave, the direction of wave propagation and the water level above the sensor influence the response of the sensor. We will discuss the advantages and disadvantages that are inherently associated with the canal architecture. Finally, we will show how an array of artificial neuromasts can be used to determine the direction of a wave train.

2. Materials & Methods

2.1. Sensor

The functional elements of the sensor (LED, silicone bar, canal and position sensitive diode) were incorporated into separate circular POM plates that were stacked and screwed together (c.f. Fig. 15). The electronic components were mounted on custom fabricated circuit boards. Transparent PVC plates were glued onto the POM components to seal the electronics watertight. Supply and data wire outlets were sealed with polyurethane coating.

In most experiments a sensor with only one artificial neuromast was used (c.f. Fig. 15 a-c, single-sensor). For the detection of the propagation direction of the surface wave a sensor with four artificial neuromasts was built (c.f. Fig. 15d, quadruple-sensor). Sharing the center pore, four individual neuromasts were oriented 90° to each other leading to a cross shaped pore pattern. A POM inset in the center pore was hydrodynamically separated the individual artificial neuromasts from each other.

The sensors were mounted on a laboratory stand in the center of a circular plastic tank (diameter 390 cm, water depth 17 cm). The laboratory stand allowed to position the sensors 2 mm below the water surface. The tank walls were covered with foam plastic to reduce the reflection of surface waves.

The sensor was powered by a laboratory power supply that allowed to control the supply voltage of the LED and the position sensitive photodiode. The sensor signal was digitized (Micro 1401, CED, Cambridge, England) and monitored and analyzed on a PC using the Spike2 software (Version 7, CED, Cambridge, England).

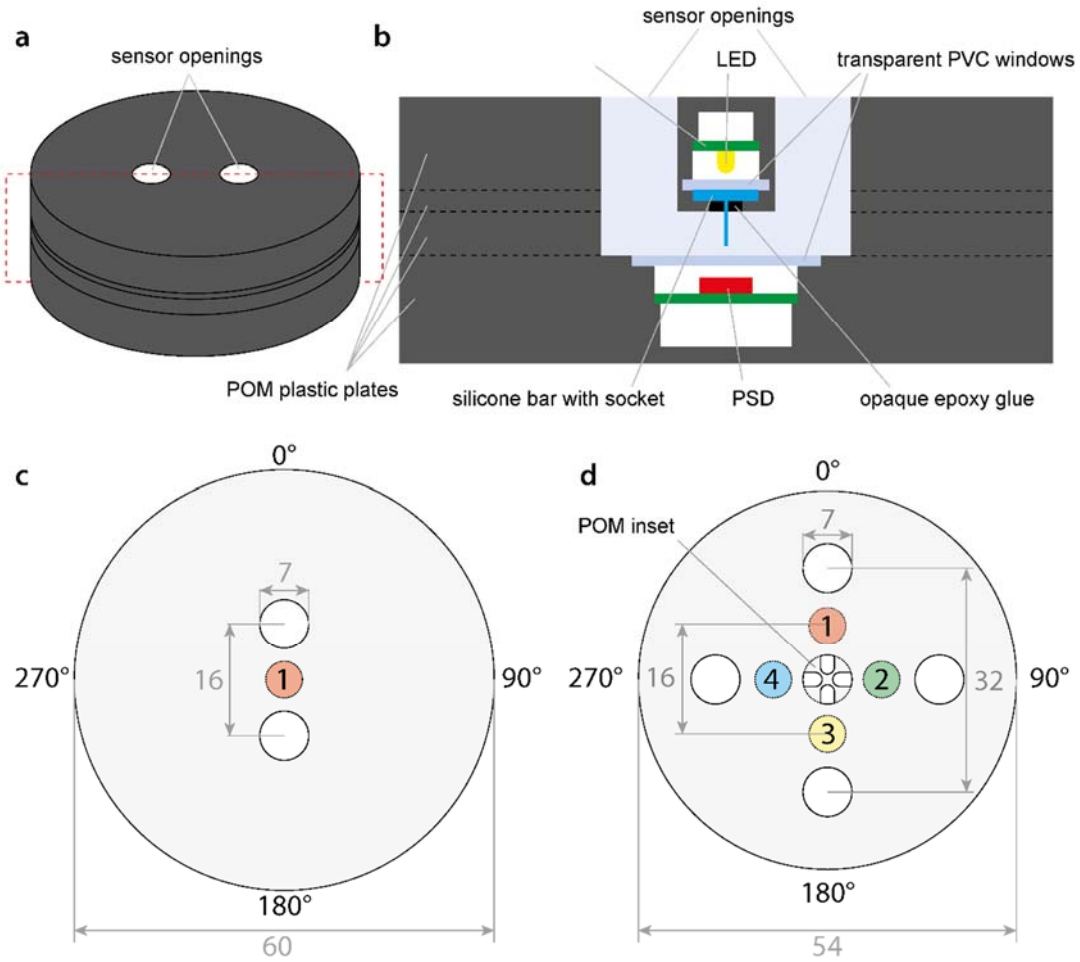

Fig. 15 Single- and quadruple ALL sensors 3-dimensional scheme (**a**) and cross-section of the single-sensor (**b**). Dashed rectangle in **a** indicates the position of the cross section. The sensor dimensions, the neuromast numbering and the angle definition are shown in **c** (single-sensor) and **d** (quadruple-sensor).

2.2. Generation of surface waves

A plastic rod (diameter 1 cm), attached to a mechanical shaker (VT-20 Shaker 20N, Sigmatest, Gottmadingen, Germany), was used to generate concentric water surface waves. The shaker was driven by an AC Power Amplifier (PA75-2CH, Sigmatest, Gottmadingen, Germany) that was controlled by an AD/DA converter (Micro 1401, CED, Cambridge, England). An acceleration sensor (ADXL330, Analog devices, Norwood, MA, USA) inside the plastic rod monitored the acceleration of the rod. The acceleration sensor signal was fed into the AD/DA converter.

The mechanical shaker was attached to linear guides (isel Germany AG, Germany) that allowed movements in all directions. Thus the position of the wave source relative to the position of the lateral line sensor could be adjusted at will.

Signals used to drive the shaker were programmed in Matlab (Version 7.8.0, The Mathworks, Inc., Natrick, MA, USA; sampling frequency = 5000 Hz). In most experiments we used mono frequency signals (3, 6, 9 or 12 Hz, duration 1 s, rise and fall time 0.5 s, c.f. Fig. 16, top). The actual amplitude of the waves was adjusted with the AC power amplifier such that the signal amplitudes were big enough to be detected by the ALL and the acceleration sensor but small enough to reduce surface wave reflections. Each sine wave signal was presented 5 times. Inter-stimulus duration was 8 s.

In addition to the mono frequency stimuli we generated a sweep stimulus (duration 60 s, constant amplitude, rise and fall time 0.5 s). Frequency constantly rose from 1 to 30 Hz (fixed rate of relative frequency increase; $f_n=f_{n-1}*x$). Sweeps were presented only once for each stimulus condition.

2.3. Data analysis

Data was analyzed using Matlab. ALL signals were subdivided into sections of 3 s (from 0.5 s before to 2.5 s after rod vibration onset). Signals were averaged, the DC offset was removed and a smoothing filter (time constant = 5 ms) was applied. To quantify the strength of a signal, the integral of its modulus was calculated. In case of the quadruple-sensor the delay between the signals of the individual neuromasts was determined with cross-correlation.

If a sweep stimulus was applied, the response of the artificial neuromast was quantified by calculating integrals of the modulus of the sensor signal at time intervals matching the duration of the vibration cycles (increasingly smaller time intervals for increasing frequencies). The integrals were then divided by the duration of the vibration cycles.

2.4. Experiments

2.4.1. Comparison with an optical displacement sensor

Measuring the vertical distance between a fixed point above the water and the water surface allows to detect water surface waves. An optical displacement sensor (ODS) was used for this purpose. It is a common tool to contactlessly detect surface waves (Grap et al., 2015).

In a first set of experiments a sweep stimulus was generated. This stimulus was measured simultaneously with the ALL single-sensor and an ODS (optoNCDT 2400-10, Micro-Epsilon, Ortenburg, Germany). The two sensors were positioned at opposite sides of the wave source. The shortest distance from the center of the wave source to the measurement point of the ODS respectively to the center of the ALL was 5 cm. Stimulus angle was 0° (c.f. Fig. 15c). After the first measurement the wave source was moved perpendicular to the connecting line between the two sensors at 1 cm increments over a total distance of 10 cm. At each position the sweep stimulus was presented. Note that in this experiment not only the source distance but also the stimulus angle increased. The ODS was, however, not directional sensitive, i.e. it responded equally well to surface waves from all directions.

2.4.2. Stimulus angle

To test the influence of the stimulus angle on the response of the ALL, we increased the stimulus angle in 15° steps (wave source distance 10 cm). The frequency of the applied surface wave stimuli was 3, 6, 9 and 12 Hz. The 3, 9 and 12 Hz stimuli were applied between 0° and 90°, 6 Hz stimuli were applied between 0° and 360°.

2.4.3. Source distance

The sensor was stimulated with water surface waves generated at distances between 0 mm and ± 200 mm (stimulus angle 0° respectively 180°; c.f. Fig. 15c). With the 6 Hz stimuli, a transect from -200 (180°) to +200 mm (0°) was performed. The interval between source positions varied between 2 mm in the proximity of the sensor and 20 mm in the distance (c.f. Fig. 19a,b). At 3, 9 and 12 Hz, stimuli were only presented at distances between 20 and 200 mm.

2.4.4. Sensor depth

The distance between sensor and water surface was increased in 1 mm steps between 2 mm and 53 mm. Source distance was 10 cm, stimulus angle was 0°. Sensor depth was defined as the distance between the top of the sensor and the water surface, it was measured with a digital caliper. Wave stimuli of 3, 6, 9 and 12 Hz were used. The sensor depth was increased until a signal no longer was visible (e.g. 12 mm at 12 Hz, 53 mm at 3 Hz).

2.4.5. Quadruple-sensor – Direction detection

2.4.5.1 Circular stimulus pattern

We stimulated the quadruple-sensor with 6 Hz surface waves (source distance 10 cm, stimulus angles 0° to 360°, 15° intervals).

2.4.5.2 Raster stimulus pattern

We again presented 6 Hz surface waves. The wave source was positioned within a rectangular raster of 200 x 200 mm, spacing between positions was 20 mm (c.f. Fig. 21f).

3. Results

The ALL responded to water surface waves. Fig. 16 shows an example of the output voltage of the DA converter (used to control the mechanical shaker), the signal of the acceleration sensor (used to monitor the movement of the rod attached to the shaker) and the signals of the ODS respectively the ALL (measuring the surface wave). Source distance was 10 cm, stimulus angle was 0°. As expected, the acceleration sensor signal resembled the output voltage of the DA converter used to control the mechanical shaker. The ODS signal as well as the ALL signal occurred with a delay of about 0.3 s, the period of time which the surface wave needed to travel from the wave source towards the sensors.

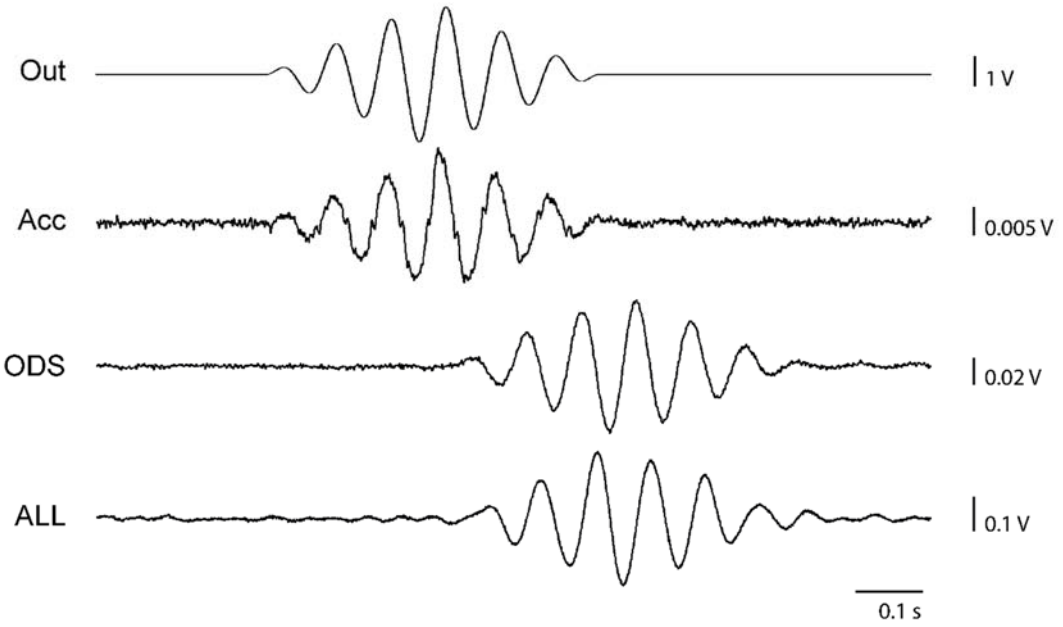

Fig. 16 Sine pulse stimulation From top to bottom: Output voltage of the DA-converter (**Out**), Acceleration sensor signal (**Acc**), optical displacement sensor signal (**ODS**) and ALL signal (**ALL**). Stimulus frequency 6 Hz, source distance 10 cm, stimulus angle 0°.

3.1. Comparison with an optical displacement sensor

Comparing our ALL with the ODS revealed that the sensors differed in frequency response and directional sensitivity. While the frequency response of the ODS (Fig. 17a, red graph) had a maximum at 8 Hz, the ALL (Fig. 17a, blue graph) had a maximum response at 6 Hz and an additional local maximum at 17 Hz, separated by a local minimum at 13 Hz.

When the wave source was moved away from the sensors perpendicular to the connecting line between the two sensors (resulting in an increase in source

distance and stimulus angle) the response of the ODS decreased across all frequencies. However, the single peaked shape of the response profile remained (Fig. 17c). Normalizing the response profiles (c.f. Fig. 17d) reveals that with increasing distance (Fig. 17d, from blue to red graphs) higher frequencies were stronger attenuated than lower frequencies.

With the ALL different results were obtained. Similar to the ODS the average response across all frequencies decreased with increasing source distance (Fig. 17e). In contrast, the shape of the response profile changed with source position (Fig. 17e). The local minimum, at the stimulus angle 0° present at 13 Hz (c.f. Fig. 17e, blue graph), shifted towards higher frequencies and finally diminished with increasing stimulus angle respectively source distance (c.f. Fig. 17e, red graph).

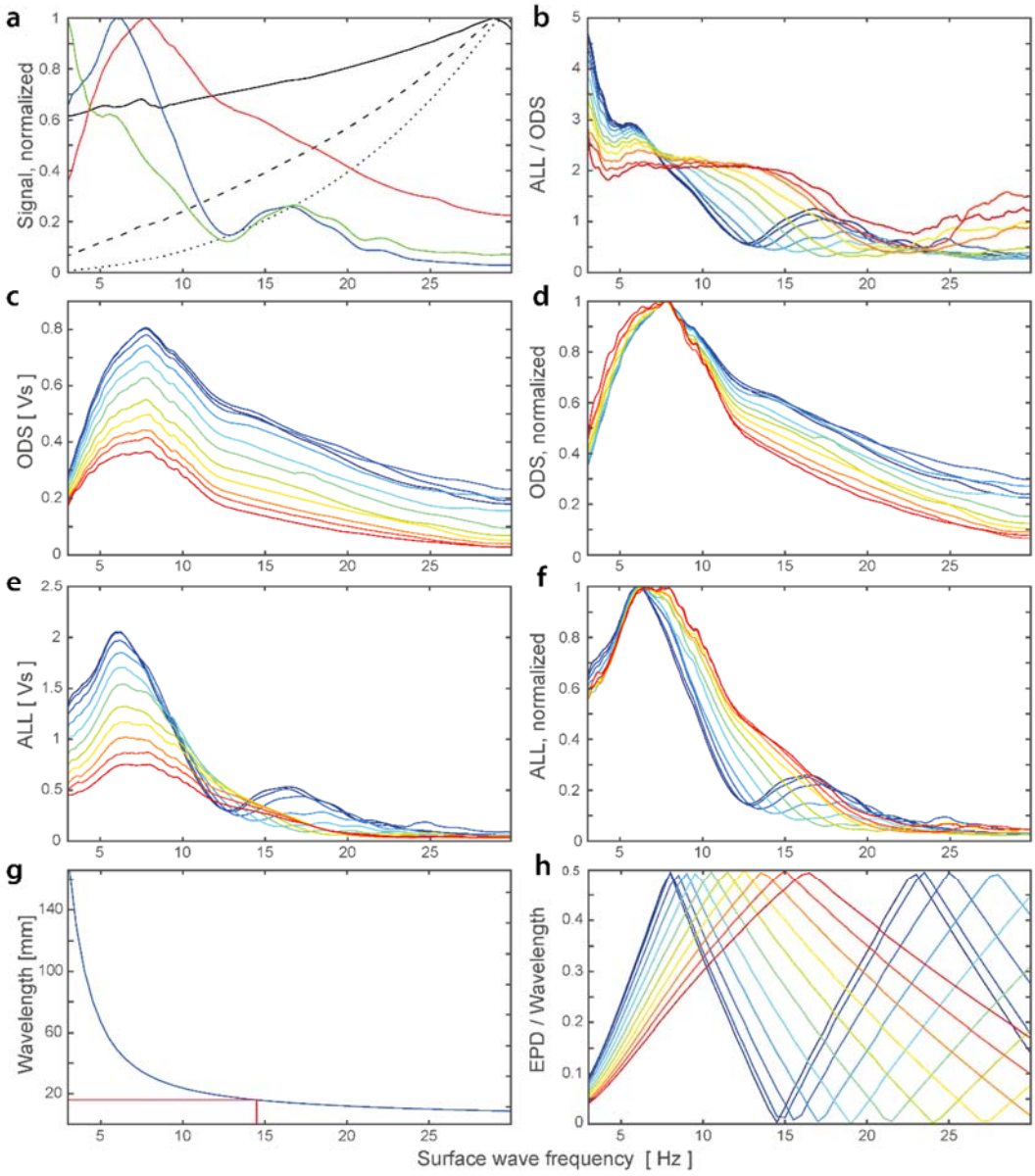

Fig. 17 Comparison with an optical displacement sensor (**a**) Frequency response of the ODS (red graph), the ALL (blue graph) and the ratio of both sensor signals (green graph). Source distance was 10 cm, stimulus angle was 0°. The solid, dashed and dotted black lines indicate displacement, velocity and acceleration of the wave source (vibrating rod). (**c**,**d**) Responses of the ODS for different source positions (distance and angle). (**e**,**f**) Corresponding responses of the ALL. (**b**) Ratio of ALL and ODS signal. (**g**) Wavelength of surface waves as function of wave frequency. Red lines mark the frequency at which wavelength equals IPD (16 mm at 14.5 Hz). Calculation according to (Bleckmann et al., 1989*a*). (**h**) Interference of EPD and wavelength as function of the surface wave frequency. Values above 0.25 indicate positive, values below 0.25 negative interference. See discussion for further description. Color coding in **b-f**, **h**: From blue to red source distance increases from 50 to 112 mm, the stimulus angle increases from 0° to 63° (increments can be accessed from the experiment description in the materials & methods section).

3.2. Stimulus angle

When the stimulus angle was varied (source distance 10 cm), the directional sensitivity of the sensor became apparent (Fig. 18). At 6 Hz (green graph) the ALL was most sensitive at 0° and 180°. In contrast, at 90° and 270° a minimum

response was observed. The response was symmetrical across all quadrants, forming two symmetric areas of high sensitivity oriented towards at 0° and 180°.

According to the response profiles obtained in the sweep experiment (c.f. Fig. 17a, blue graph), strongest responses were obtained at 6 Hz, followed by 3, 9 and 12 Hz.

For a better comparison of directional sensitivity responses were normalized (Fig. 18b). At 3 and 6 Hz (Fig. 18b, green and red graph) the strongest responses occurred at a stimulus angle of 0°. The strongest responses at 9 and 12 Hz (Fig. 18b, blue and black graph) were observed at 45° respectively 60°. Across all frequencies minimum responses were observed at 90° respectively 270°.

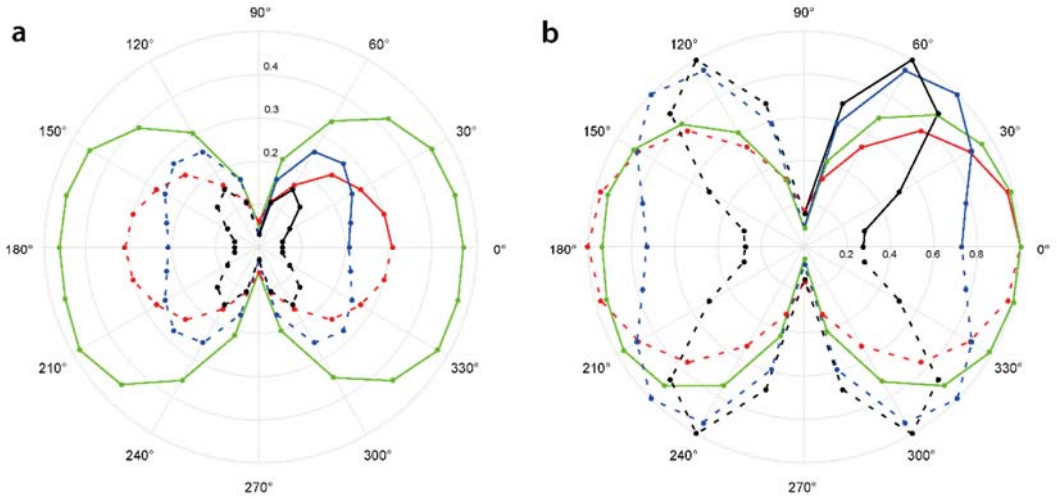

Fig. 18 Stimulus angle Response of the ALL as function of the stimulus angle. (**a**) Absolute values [Vs]. (**b**) Data normalized to the maximum response for each stimulus frequency. Stimulus frequency was 3 (red), 6 (green), 9 (blue) and 12 Hz (black). Solid lines indicate data points. Since directional sensitivity is symmetrical to the center of the sensor, measurements at 3, 9 and 12 Hz were only done in the range 0° to 90°. Values in the range from 90° to 360° (dashed lines) were mirrored.

3.3. Source distance

In the next experiment, we altered the source distance (stimulus angle 0° or 180°; c.f. Fig. 19). At 6 Hz we recorded the response of the sensor while moving the wave source along a transect from -200 mm (stimulus angle 180°) to +200 mm (stimulus angle 0°; Fig. 19a). With decreasing distance the response increased up to a maximum that occurred at a distance of ±8 mm (wave source directly above canal pores). When source distance was between -8 to +8 mm (i.e. between the pores), the response suddenly decreased to almost 0 Vs at the source

distance 0 mm (center of the sensor). As expected, the response profile was symmetrical.

Comparing the responses to different stimulus frequencies (source distance 20 to 200 mm; Fig. 19b) revealed that the relative decrease of the response with increasing source distance increased from 3 to 12 Hz (from the red to the black graph). Note that data was normalized to the particular responses at 20 mm.

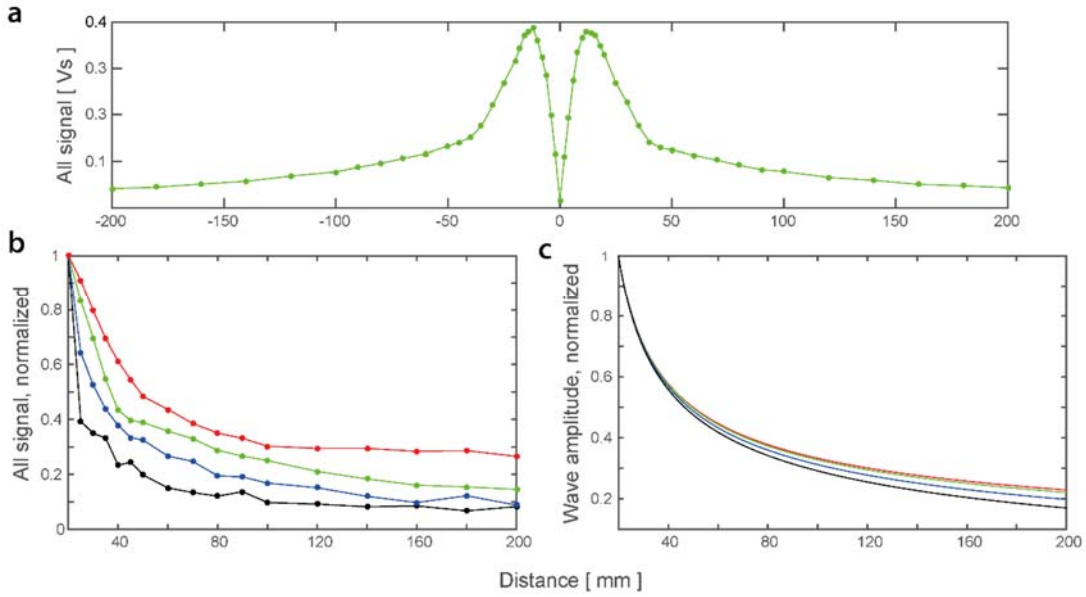

Fig. 19 Source distance Response of the ALL as function of source distance. (**a**) A 6 Hz surface wave was presented at distances between -200 mm (180° stimulus angle) and +200 mm (0°). (**b**) Data shown for source distances between 20 and 200 mm (stimulus frequencies were 3 (red), 6 (green), 9 (blue) and 12 Hz (black). (**c**) Calculated attenuation curves of surface waves of different frequencies (c.f. **b**) as function of source distance.

3.4. Sensor depth

For all stimulus frequencies (3, 6, 9 and 12 Hz) the response amplitudes decreased with increasing sensor depth. We used normalized exponential fits to compare the responses obtained at different frequencies. In general, response attenuation was larger at higher stimulus frequencies (Fig. 20b).

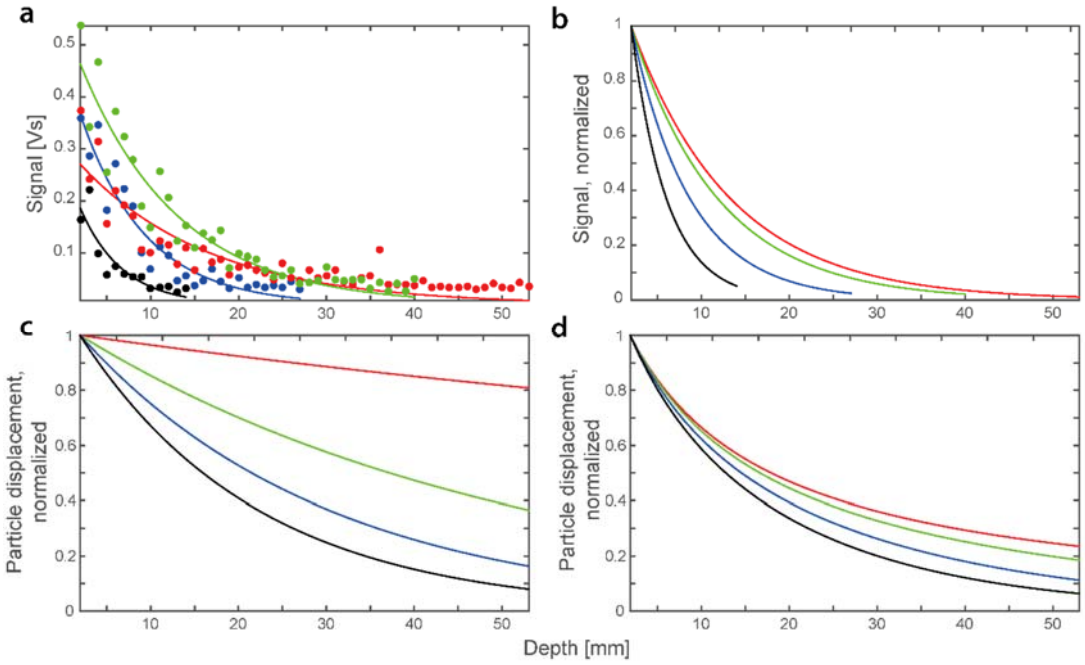

Fig. 20 Sensor depth Responses of the ALL as function of sensor depth. Stimulus frequency was 3 (red), 6 (green), 9 (blue) and 12 Hz (black). (**a**) Absolute values. Graphs show exponential fit functions. (**b**) Fit functions normalized to the sensor depth 2 mm. (**c**,**d**) Calculated horizontal particle displacement as function of water depths (2 to 52 mm, frequencies and color code as in **a** and **b**). In **c** the maximum water depth at the observation point h was set to the depth of the experimental tank, in **d** it was set to the sensor depth. See discussion part for further description.

3.5. Quadruple-sensor – Direction detection

3.5.1. Circular stimulus pattern

In a first experiment we generated 6 Hz surface waves (source distance 10 cm, stimulus angle 0° to 360°). Similar to the single-sensor experiment (c.f. Fig. 18), the highest responses were elicited when the respective artificial neuromast was stimulated in the direction of its pore orientation (e.g. 0° respectively 180° for artificial neuromast 1 and 3; Fig. 21b). However, unlike in the single-sensor experiment, polar plots were not symmetrical in all axes (Fig. 21b, red plot). Instead, an artificial neuromast responded stronger when it was stimulated from the direction of its outer pore (e.g. 0° for artificial neuromast 1; remember that each sensor was connected with one outer pore and the common center pore, c.f. Fig. 15d). Although the absolute response over all stimulus angles varied across the individual artificial neuromasts (not apparent in Fig. 21b because data was normalized to the maximum), the shape of their directionality profile is similar.

To determine the propagation direction of the wave, the delay of the signals of the artificial neuromasts 1 and 3 respectively 2 and 4 was calculated by cross-

correlation (see Fig. 21a for an explaination of artificial neuromast numbering). Fig. 21c shows the delay between the signals of artificial neuromasts 1 and 3 (blue graph) as a function of stimulus angle. The resulting curve resembles a sine function (c.f. Fig. 21c). The maximum delay of about 0.1 s was reached at 0° and 180°. Note that negative values indicate that the surface wave first arrived at artificial neuromast 3. The maximum cross-correllation coefficient was above 0.8 for most of the presented stimulus angles (red graph). At 80° and 100° resectively 260° and 280° the correlation coefficient dropped to or below 0.8. This drop was caused by the small signal amplitudes of the neuromast(s) whose pores were aligned perpendicular to the wave propagation direction. To account for this we set the delay to 0 s when the correlation coefficient dropped to or below 0.8 (Fig. 21, data points marked green). In Fig. 21d the delay of the responses of the artificial neuromasts 1 and 3 respectively 2 and 4 is plotted as function of stimulus angle. Both delays resemble a sine function with a 90° phase shift.

The stimulus angle α was calculated according to:

$$\alpha = \cot^{-1} \frac{dt_{13}}{dt_{24}} \tag{9}$$

where dt_{13} is the delay between artificial neuromast 1 and 3 and dt_{24} is the delay between artificial neuromasts 2 and 4.

When the caclulated stimulus angle is plotted against the actual stimuls angle (Fig. 21e) it turns out that the stimulus angles were determined successfully.

3.5.2. Raster stimulus pattern

We finally tested the stimulus angle determination procedure not only for a fixed source distance. To do so we positioned the wave source within a rectangular raster resulting in various source distances and stimulus angles (c.f. Fig. 21f). The results resemble the results of previous experiments: stimulus angle determination is precise at most source positions. Angular deviations of 20° or higher (angle determination error) only occured around the stimulus angles of 0° and 90° or if the wave source was in the proximity of the sensor.

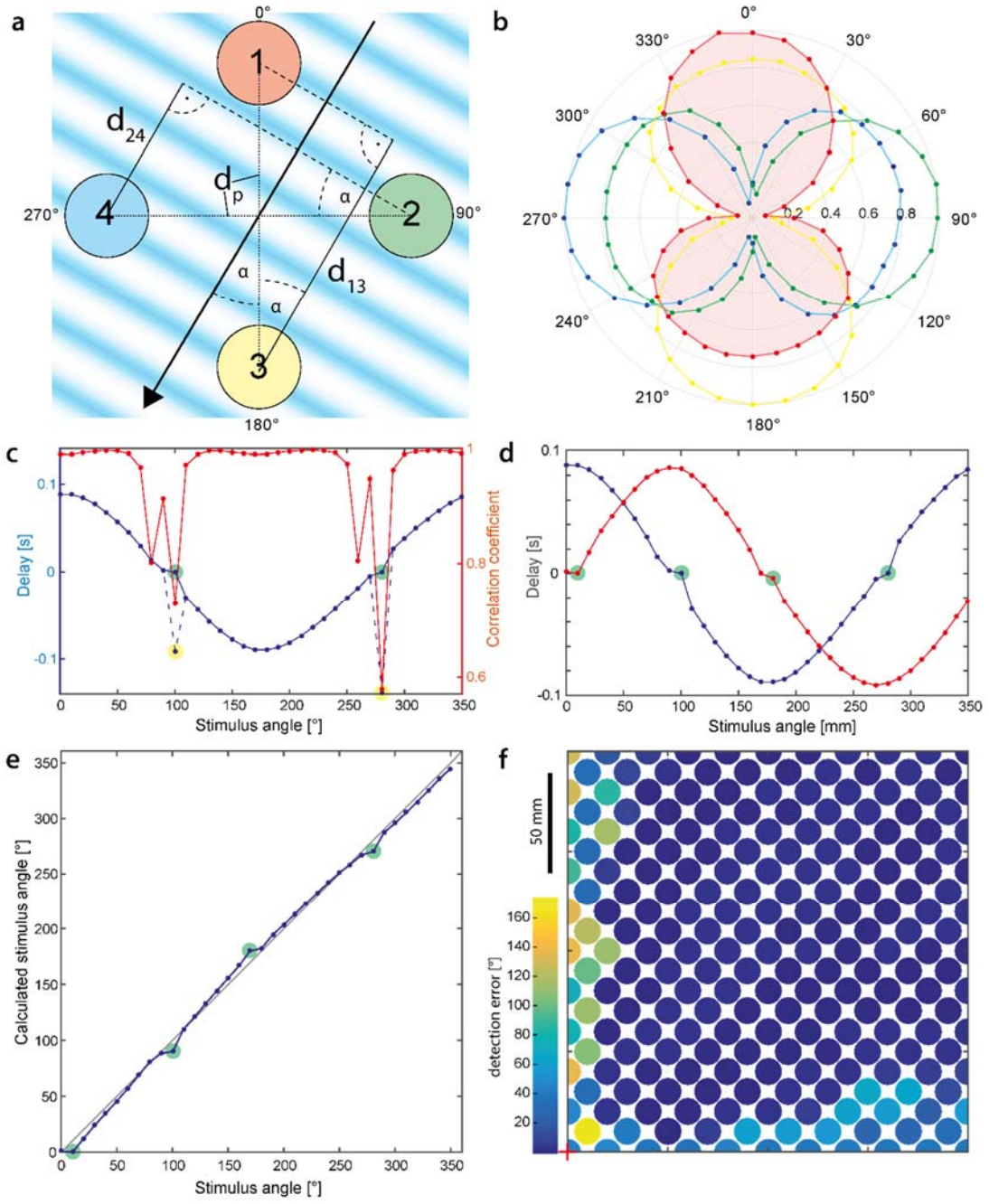

Fig. 21 Quadruple-Sensor (**a**) Geometrical conditions and definitions when a surface wave successively approaches the artificial neuromasts. Black arrow indicates the direction of a surface wave, blue and white bars represent the peaks and troughs of the wave. $\boldsymbol{\alpha}$ stimulus angle, $\boldsymbol{d_{13}}$ and $\boldsymbol{d_{24}}$ effective distances between the particular neuromasts, $\boldsymbol{d_p}$ distance between the neuromasts, equals the IPD. (**b**) Responses of the artificial neuromasts of the quadruple-sensor are plotted against stimulus angle (polar plot). Responses are normalized to the maximum response of each neuromast. Color coding according to the colors of artificial neuromasts in **a**. The response of sensor 1 is highlighted in red. (**c**) The delay between the signals of sensor 1 and 3 (blue graph) as well as the corresponding correlation coefficient are plotted against stimulus angle. Corrected data points (green; see text for explanation) are marked in yellow. (**d**) The delays between the signals of artificial neuromast 1 and 3 (blue graph) respectively artificial neuromast 2 and 4 (red graph) as function of stimulus angle. (**e**) Calculated stimulus angle as function of actual stimulus angle. Grey line indicates perfect stimulus angle detection. (**f**) Raster stimulus pattern: detection error at different source positions in one quadrant (0°-90°). Red cross (bottom-left) indicates the center of the sensor.

4. Discussion

4.1. Comparison with an optical displacement sensor

In order to interpret the responses of the ALL it is important to know the frequency and amplitude of the surface wave stimulus. We used an ODS (optoNCDT 2400-10, Micro-Epsilon, Ortenburg, Germany) to measure the vertical displacement of the water surface over time, i.e. to record the surface waves. The device we used was well suitable for this task due to its high spatial (0.4 µm vertical displacement over an area 50 µm) and temporal (2 ms) resolution. The ODS signal represented the actual surface wave stimulus.

The importance of surface wave monitoring becomes obvious when we consider the wave generation process. We used a sine sweep signal with an amplitude of 1 V to generate water surface waves. The plunger movement was monitored by an acceleration sensor (c.f. Fig. 17a, dotted line). The velocity (=acceleration/2 f; dashed line) and the displacement (=velocity/2 f; solid line) of the plunger were calculated. None of these parameters resembled the surface wave displacement amplitude (red graph) when plotted against stimulus frequency. Hence, measuring the plunger movement with an acceleration sensor does not provide sufficient information to characterize the surface waves. In fact, hydrodynamic processes influence the surface wave in the course from its generation by the solid-fluid interaction with the plunger to the propagation process from the source to the sensor.

Some influence comprises the attenuation of the surface wave when it is horizontally propagating over the water surface and when it vertically propagates into the water. Both types of attenuation are frequency dependent and in both cases higher frequencies are stronger attenuated (Bleckmann, 1988). They will be discussed in detail later. Yet, they are relevant factors that cause the decrease of wave amplitude with increasing frequency (Fig. 17a, red graph; decrease from ~8 to 30 Hz). In contrast, from 3 to about 8 Hz the wave amplitude constantly increases. This might be explained by the increasing plunger acceleration (c.f. Fig. 17a, dotted line). However, further complex hydrodynamic processes that are difficult to access might have had influenced the surface wave amplitude, too. Therefore it was important to directly monitor the waves with the ODS.

Plotting the frequency response of the ODS for different source positions revealed a decrease of displacement amplitude with increasing source distance and stimulus angle across all stimulus frequencies (Fig. 17c). Normalizing the response profiles furthermore shows that the attenuation was more severe for the higher frequencies (Fig. 17d). Both findings were caused by the frequency dependent attenuation of propagating surface waves.

The frequency dependent response profiles of the ALLs (Fig. 17a, blue graph, graphs in e and f) are the result of (1) the input, namely the surface wave amplitude and (2) the sensor properties. To analyze the latter, we divided the response of the ALL (Fig. 17a blue graph) by the response of the ODS (red graph). The resulting graph (green) represents the frequency dependent sensitivity of the ALL.

Over all, the graph shows a decrease in sensitivity with increasing frequency. This was expected for this type of sensor and has been observed in dipole stimulus experiments, too (c.f. chapter I). It can be explained by the low-pass filter characteristics of lateral line canals (van Netten, 2006). In addition to this overall decrease, the green graph (Fig. 17a) shows a local peak at 6 Hz. Even though this peak got less prominent when source distance and stimulus angle were increased (Fig. 17b) it remained relatively constant at 6 Hz. Most likely, this peak was caused by the resonance of the sensor's deflective silicone bar. A resonance peak is typical for lateral line sensors (Denton & Gray, 1988; van Netten, 2006) and has also been observed in the dipole stimulus experiments mentioned above.

Furthermore, the sensor showed a local sensitivity minimum at about 13 Hz. Most likely this was caused by geometrical interference of the IPD and the wavelength of the surface wave. Assuming that the wavelength matches the IPD of our sensor (16 mm), both pores will simultaneously be exposed to the same phase of the wave, resulting in equal pressure at both pores which is not an effective stimulus. In contrast, the pressure difference is maximal, when one pore is exposed to a wave peak while the other pore is exposed to a wave trough, e.g. when the wavelength is half (or third or fourth etc.) of the IPD. More comprehensively, wavelength and IPD interfere negatively if their quotient is close to an integer (respectively the reciprocal of an integer).

In Fig. 17g the theoretical wavelength of surface waves is plotted as function of wave frequency. The red rectangle refers to a wavelength of 16 mm (IPD), which occurs at about 14.5 Hz. At this frequency we thus expect a decrease in sensitivity due to the negative interference of IPD and wavelength. In our experiments a trough in the response profile was located at 13 Hz. The deviation of 1.5 Hz might, however, be explained by the superposition of the interference effective with other sensor properties or by discrepancies of the calculated and the actual wavelength.

At stimulus angles ≠0° respectively ≠180° it is not the ratio of wavelength and IPD, but the ratio (=Q) of wavelength and effective pore distance (EPD) that determines the interference. EPD is the distance the surface wave travels from the first to the second pore (assuming waves with a parallel wave front). At a stimulus angle ≠0° respectively ≠180°, the EPD is different from the IPD (c.f. Fig. 22). It is maximal at 0° respectively 180° (EPD = IPD) and 0 at 90° respectively 180°.

In Fig. 17h the difference between Q and the closest integer is plotted against the wave frequency for all tested source positions (color coded). Values close to 0.5 indicate positive, those closer to 0 negative interference. Both, the frequencies of the most positive (peaks) and most negative (troughs) interference increase with increasing stimulus angle (and thus decreasing EPD; from blue to red graph). Due to the superposition with other sensor properties (e.g. the decrease of the sensitivity with increasing wave frequency), this interference effect is not as prominent in the recorded data (Fig. 17b) as in the calculated curves (Fig. 17h). However, the shift of the negative interference trough from 13 Hz to higher frequencies that is expected with increasing stimulus angle (c.f. Fig. 17h) is apparent in the recorded data (Fig. 17b) as well.

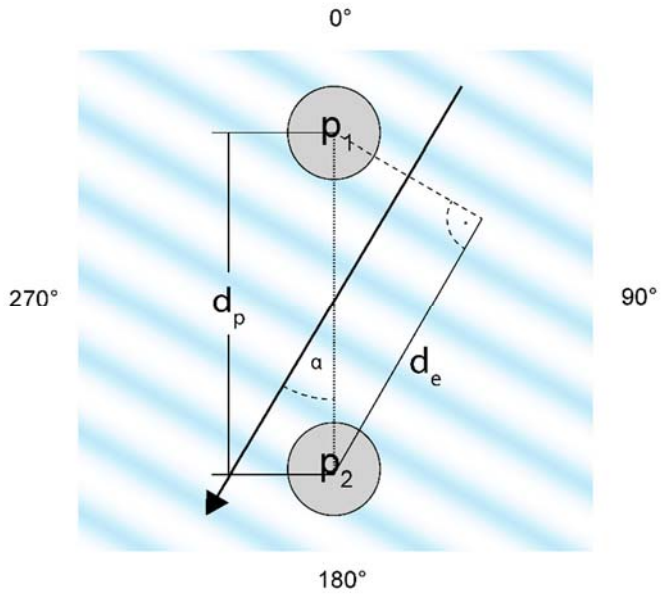

Fig. 22 Effective pore distance Geometrical conditions and definitions when a surface wave successively approaches the pores $\mathbf{p_1}$ and $\mathbf{p_2}$ of an artificial neuromasts. Black arrow indicates the direction of a surface wave, blue and white bars represent the peaks and troughs of the wave. $\boldsymbol{\alpha}$ stimulus angle, $\boldsymbol{d_p}$ IPD, $\boldsymbol{d_e}$ EPD.

4.2. Stimulus angle

The directional sensitivity of the ALL was investigated with surface waves that approached the sensor from various stimulus angles (Fig. 18). Across all stimulus frequencies, the most apparent result was that the sensor did not respond at the stimulus angles 90° and 270°. At these stimulus angles the wave source has an equal distance to both pores. Similar to the negative interference effect described above, both pores are exposed to the same phase of the wave and thus no response is elicited. At stimulus angles increasingly different from 90°or 270° the EPD increases from 0 to 16 mm (=IPD). Recalling the fact that interference is positive when the EPD = wavelength/2, we expect that at high frequencies (shorter wavelength) the sensor shows the maximum response at high stimulus angles (=small EPDs). In contrast, at low stimulus frequencies (longer wavelength) the sensor shows the maximum response at low stimulus angles (=large EPDs). This was indeed observed: At 12 Hz the maximum response was elicited at 60°, at 9 Hz at 45° and at 3 and 6 Hz at 0° (Fig. 18). Furthermore, the calculation of the interference (Fig. 17h) explains the data shown in Fig. 18. At 3 and 6 Hz the most positive interference is predicted for a stimulus angle of

0° (the darkest blue graph (0°) shows the highest positive interference value). In contrast, at 12 Hz the positive interference is lowest at a stimulus angle of 0°, all other calculated stimulus angles show a more positive interference (note that in Fig. 17h only stimulus angles up to 63° are considered). The interference calculation (Fig. 17h) does not exactly apply to the stimulus angle data (Fig. 18). For instance, at 12° the calculation predicts a maximum response at 50°, not at 60° as observed. This most likely is due to the superposition of the interference effect with other sensor properties.

4.3. Source distance

When the ALL was stimulated with surface waves from various source distances the maximum response was observed at a source distance of 8 mm (Fig. 19a). At this distance the plunger was positioned right above one pore. When the plunger was positioned between the pores the response was weaker. The response almost entirely diminished at a source distance of 0 mm, i.e. if the plunger was placed right above the center of the sensor. In this case the pores were at equal distance from the source and thus were exposed to the same phase of the wave. Therefore no response was elicited.

At distances between 8 and 200 mm the response of the sensor constantly decreased. The decrease was more severe at higher stimulus frequencies (Fig. 19b). This is due to the attenuation of propagating water surface waves. For source distances >2 cm the attenuation can be calculated according to (Bleckmann, 1988):

$$A = A_i \sqrt{\frac{R_i}{R}} e^{(16\nu\pi^2/\lambda^2 C_{ph})(R_i - R)} \tag{10}$$

where A_i is the displacement amplitude of the wave at distance R_i, A is the actual wave amplitude at distance R, ν is the kinematic viscosity of water, λ is the wavelength and C_{ph} is the phase velocity of the surface wave. Both wavelength and phase velocity depend on wave frequency (Bleckmann 1985, Fig. 19c).

4.4. Sensor depth

For the stimulus frequencies 3, 6, 9 and 12 Hz Fig. 20a shows the responses of the sensor as function of the sensor depth. Data points scatter around the exponential fit curves. This possibly is due to our imperfect technique of measuring water depth. The water surface tension caused a meniscus at the caliper. This made it impossible to precisely measure the sensor depth. However, normalizing the exponential fit curves revealed systematic data (Fig. 20b).

The data shows that the responses of the sensor decreased with increasing sensor depth and stimulus frequency. Due to the attenuation of water surface waves with increasing water depth this was expected. The horizontal and vertical displacement component A_h and A_v of a fluid particle that moves on a circular/elliptical path, typical for surface waves, can be calculated by the equations (Lighthill, 2001):

$$A_h = \frac{A_0}{\sinh(k * h)} * \cosh(k(h - z)) \tag{11a}$$

$$A_v = \frac{A_0}{\sinh(k * h)} * \sinh(k(h - z)) \tag{11a}$$

where $k = 2\pi/\lambda$, A_0 is the maximal displacement amplitude of the particles at the water surface above the observation point, z is the water depth of interest and h is the maximum water depth at the observation point. In Fig. 20c,d the horizontal particle displacement amplitude is plotted against water depth for the frequencies 3, 6, 9 and 12 Hz. In c the maximal water depth was set to the depth of the experimental tank ($h = 17$ cm), in d it was set to the sensor depth (top of the sensor) + the distance from the sensor surface to the floor of the artificial lateral line canal ($h = z + 14.5$ mm). In both scenarios the particle displacement decreased with increasing depth and frequency. However, the apparent higher similarity of the data (Fig. 20b) with the attenuation curves shown in d (maximum water depth = sensor depth) suggests that the sensor influences the particle displacement. Its rigid spatial extent most likely interferes with the moving water particles, decreasing their displacement amplitude, especially at low frequencies.

4.5. Quadruple-sensor – Direction detection

Measuring the directional sensitivity of each artificial neuromast (Fig. 21b) revealed results similar to the results obtained with the single-sensor (Fig. 18). One difference was the asymmetry of the directional responses. This might have been caused by the asymmetry of the sensor: The inner pore was narrower than the outer pore, also the outer pore was closer to the edge of the sensor. However, the more relevant reason for the asymmetry is the geometry of the setup. Each artificial neuromast was positioned 8 mm off the center while the source distance was kept constant with respect to the center of the sensor. For instance, when the stimulus angle was 0°, the artificial neuromast 1 (c.f. Fig. 21a) was 16 mm closer to the wave source than at the stimulus angle 180°, resulting in a larger stimulus amplitude and thus a stronger response. In addition, the effective stimulus angle for each artificial neuromast is different from the stimulus angle as defined with respect to the center of the quadruple-sensor (note the difference between "effective stimulus angle" and "stimulus angle" in the following). For instance, for artificial neuromast 1, in the range from 0° to 180°, the effective stimulus angle was higher (respectively lower in the range from 180° to 360°) than the stimulus angle as defined with respect to the center of the quadruple-sensor. Therefore artificial neuromast 1 e.g. responded weaker at 60° than at 120°. At 60° the effective stimulus angle was closer to 90°, the EPD was shorter, the pressure difference between the pores was less and the response was weaker. Consequently, artificial neuromast 1 showed the weakest responses not at 90° and 270°, but at 75° and 285°.

The method we chose to detect the stimulus direction required the determination of the delay between the signals of the artificial neuromasts that were oriented in a 180° angle (i.e. artificial neuromasts 1 and 3 respectively 2 and 4, c.f. Fig. 21a). We used the cross-correlation to calculate the delay (c.f. Fig. 21c, for artificial neuromasts 1 and 3). High correlation coefficients indicated that for most stimulus angles the results were reliable. In the range of 90° and 270° (respectively 0° and 180° for artificial neuromasts 2+4) the correlation coefficient suddenly dropped. This was due to the low signal amplitudes caused by the short EPDs. Interestingly, the lowest correlation coefficients did not occur at 90° and 270°, but at stimulus angles 15° above and below these values. That was expected, because the individual sensors did – as mentioned above – elicit the weakest responses in the range of, but not exactly at 90° and 270° (respectively

at 0° and 180°, c.f. Fig. 21a). As the lowest correlation coefficients (delay detection errors) did only occur when the delay was close to 0 s, it was reasonable to assume a delay of 0 s when the correlation coefficient dropped below 0.8.

Once the delays of the signals of artificial neuromast 1 and 3 (dt_{13}) respectively 2 and 4 (dt_{24}) were determined, the stimulus angle α could be calculated (assuming parallel waves; c.f. Fig. 21a). The following applies:

$$\cos\alpha = \frac{d_{13}}{d_{AN}} \tag{12}$$

$$\sin\alpha = \frac{d_{24}}{d_{AN}} \tag{13}$$

where d_{AN} is the distance between the artificial neuromasts (= 16 mm). Although the effective distances between the artificial neuromasts d_{13} and d_{24} are not known we can set up the following equations to bring up dt_{13} and dt_{24}:

$$d_{13} = dt_{13} * C_{ph} \tag{14}$$

$$d_{24} = dt_{24} * C_{ph} \tag{15}$$

where C_{ph} is the phase velocity of the waves (also not known). By using (14) in (12) and (15) in (13) we get:

$$\cos\alpha = \frac{dt_{13} * C_{ph}}{d_p} \tag{16}$$

$$\sin\alpha = \frac{dt_{24} * C_{ph}}{d_p} \tag{17}$$

Dissolving (17) by C_{ph} leads to:

$$C_{ph} = \frac{d_p * \sin\alpha}{dt_{24}} \tag{18}$$

Using (18) in (16) and dissolving by α:

$$\cos\alpha = \frac{dt_{13} * \frac{d_p * \sin\alpha}{dt_{24}}}{d_p}$$

$$\cos\alpha = \frac{dt_{13} * d_p * \sin\alpha}{dt_{24} * d_p}$$

$$\frac{\cos\alpha}{\sin\alpha} = \frac{dt_{13}}{dt_{24}}$$

$$\cot\alpha = \frac{dt_{13}}{dt_{24}}$$

$$\alpha = \cot^{-1}\frac{dt_{13}}{dt_{24}} \tag{9}$$

The applicability of equation (9) becomes apparent in Fig. 21e. The calculated stimulus angles match the actual stimulus angles. The angular error does not exceed 10° even at angles at which sensor signals were weak, causing a low cross correlation coefficient (c.f. Fig. 21e, marked in green). In addition, angular errors might also have been caused by an imprecise positioning of the sensor.

The raster stimulation experiments (Fig. 21f) confirmed the results of the circular stimulation experiments: severe direction detection errors only occurred at the stimulus angles 0° and 90°. The only exception is a big error, which occurred at the stimulus angle 45°. However, it occurred when the wave source was so close to the sensor that the effective stimulus angle of artificial neuromasts 1 and 2 was close to 90° respectively 0°.

In the raster stimulation experiments the surface wave amplitudes were so large that the surface waves still could be detected even at the largest source distances. Hence, our data does not show a decline of direction detection accuracy with increasing stimulus distance.

4.6. Conclusions

The present study demonstrates that the ALL detects water surface waves when positioned horizontally below the water surface. However, some sensor characteristics are inherently associated with the sensor design: The principle of measuring differential pressure between two pores leads to responses that depend on the propagation direction and frequency of the wave stimulus. These effects can be controlled by altering the IPD to shift the negative interference of wavelength and IPD to a non-relevant frequency range. For certain applications the described effects may even be useful. For instance, altering the dimension

and properties of the sensor components can set up a mechanical filter that separates signals from noise.

Another sensor property that has to be considered is the hydrodynamic interaction of sensor and fluid. This interaction alters the surface wave and thus can lead to discrepancies between the recorded and the actual surface wave. This disadvantage can be minimized by incorporating the sensor in existent solids, e.g. the bottom of a shallow water tank or the surface of an underwater vehicle. Indeed, in some applications, an underwater surface wave sensor may be advantageous compared to overwater devices.

To locate a surface wave source an array of sensors is mandatory. Our approach to detect the propagation direction of a surface wave is only a first step. For instance, the detection error at 0°, 90°, 180° and 270° could be eliminated by backing up the sensor with another pair of artificial neuromasts. Different sensor designs and data processing algorithms must be tested. The morphology of the lateral line system of surface feeding fish can be a great source of inspiration.

III. *Xiphister* miscellaneous

1. Introduction

1.1. Outline: The functional significance of the *Xiphister* lateral line

The lateral line system is a mechanosensory organ that enables fishes to detect weak water motions and pressure gradients (Hassan, 1985; Coombs, 2002). It is used for spatial orientation, prey detection, predator avoidance, schooling and intraspecific communication (Bleckmann, 1994). The smallest functional units of the lateral line are the neuromasts, sensory structures whose cupulae are deflected by water movements. Neuromasts occur free standing on the skin (SNs) or inside subepidermal canals (CNs) that run parallel to the surface of the fish. Lateral line canals are hydrodynamically connected to the surrounding water by pores (Bleckmann, 1994).

The typical teleost lateral line trunk morphology comprises a single canal with regularly spaced pores extending from the dorsal margin of the operculum over the horizontal septum and onto the caudal peduncle. One neuromast is located between two adjacent canal pores (Webb 1989; c.f. Fig. 18b,d). The stichaeid genus *Xiphister* possesses three main trunk canals extending on each body side from the head region onto the tail fin: the dorsolateral, the mediolateral and the ventrolateral line canal (Clardy et al., 2015; Clardy & Hilton, 2015; c.f. Fig. 18a). The latter loops onto the abdomen forming a fourth canal between the pectoral girdle and the anal fin. The main canals follow a slight zigzag course. Dorsal and ventral branches (tubuli) alternately extend from the main canals at each turn of the zigzag. Pores are only present in the tubuli (up to five pores in each tubulus) whereas neuromasts can only be found in the main canals (Bleckmann & Münz 1990; c.f. Fig. 18c).

Bleckmann & Münz (1990) recorded neuronal activity from the posterior lateral line nerve (PLLN) of *Xiphister atropurpureus*. They found that the frequency sensitivity of *Xiphister* was similar to other fish species. They mapped the receptive fields of primary lateral line afferents and found a slight displacement of the receptive fields of neuromasts located in the dorsolateral and mediolateral

canal. Supported by calculations they demonstrated that multiple lateral lines lead to an increase of receptive field size for nearby objects that generate weak dipole stimuli. However, the functional significance of the tubuli and the astonishing number of pores – a key feature of the *Xiphister* lateral line morphology – remained unexplained.

In a second approach, the functional significance of the *Xiphister* lateral line was studied with an ALL mimicking the morphology of the *Xiphister* trunk canals (Klein et al., 2013). The study suggests that the *Xiphister* canals integrate hydrodynamic signals over a larger spatial area compared to a simple lateral line. This results in a lower spatial resolution. In addition, it serves as a filter for spatial noise (e.g. air bubbles): If one of the few pores of the simple lateral line canal is exposed to spatial noise, the hydrodynamic signals are masked. Conversely, in the complex *Xiphister* trunk canals, one pore is always backed up by the many neighboring pores; the hydrodynamic signal persists. Thus, Klein et al. (2013) suggested that the trunk lateral line canal of *Xiphister atropurpureus* is an adaptation to highly turbulent habitats.

However, the functional relevance of this spatial filter hypothesis was only demonstrated in ALLs made of solid plastics, stimulated with water motions disturbed by air bubble noise. It remained unclear whether the filter hypothesis is biologically relevant. Closing this gap of knowledge was the aim of the research project presented in this chapter.

For this purpose, we planned to measure the receptive fields of PLLN fibers of *Xiphister*. The approach was similar to the one used by Bleckmann & Münz (1990) with the exception that the receptive field scan had a much higher resolution: Bleckmann & Münz (1990) used a vibrating sphere that had a diameter of 17.6 mm. The sphere was manually transecting the receptive field horizontally in spatial intervals of approx. 10 mm. This method delivered a 1-dimensional image of the receptive field and only resolved the distance between the main canals (approx. 5 mm). It could not uncover the influence of single pores (which are spaced approx. 1 mm apart). In contrast, the present study used a 0.5 mm vibrating rod with a cylindrical tip as dipole source. The dipole source could automatically be moved at intervals as small as 0.1 mm in two directions over the surface of the trunk of the fish providing a 2-dimensional high resolution image of the receptive fields of primary lateral line afferents in

Xiphister. The size and structure of the receptive field can be used to examine the influence of each pore and thus to estimate how the hydrodynamic signal is spatially integrated. It finally allows to determine the functional relevance of the spatial filter hypothesis in the biological system rather than its biomimetic replica.

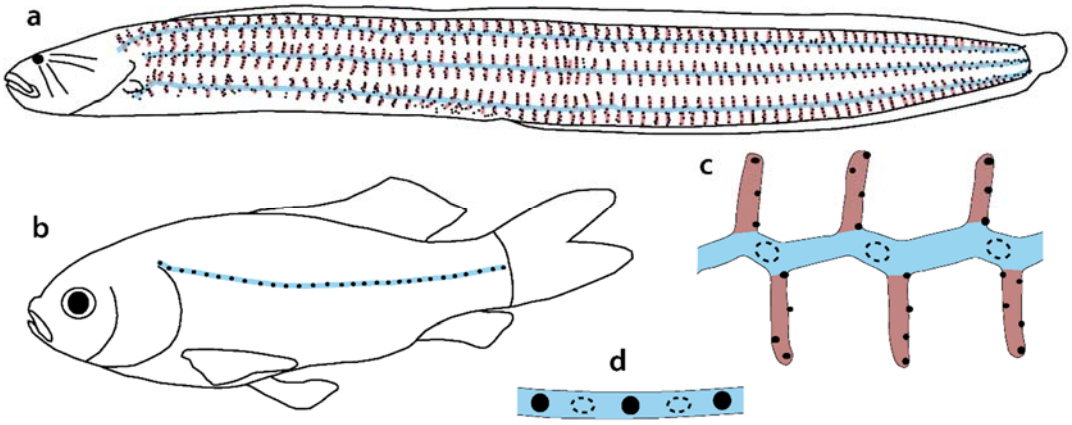

Fig. 23 *Xiphister* and goldfish trunk canal morphology Schematic overview (**a**,**b**) and close up (**c**,**d**) of the trunk canals of *Xiphister* (**a**,**c**) and goldfish (**b**,**d**). Blue: main canal; red: tubuli; black dots: canal pores. Dashed circles indicate neuromast position. Dimensions are not to scale.

1.2. Review: *Xiphister* miscellaneous

The planning of the research project outlined above started in the beginning of 2014 as a cooperation of the Bleckmann workgroup in Bonn, Germany and the Zelick workgroup in Portland, OR, USA. The apparatus to automatically scan the receptive field of a single afferent was developed in Bonn. Also, the method to record from posterior lateral line units of goldfish was established in Bonn. Subsequently, the experimental setup was transferred to Portland for a period of 3 months from August to October 2014. Specimens of *Xiphister mucosus*, a sister species of *Xiphister atropurpureus* that possesses the same lateral line features, and – for comparison – a close relative from the subfamily of the Xiphisterinae, *Anoplarchus purpurescens*, were caught at the pacific coast close to Portland. Animals were kept in the saltwater facilities of the Portland State University. Electrophysiological experiments were done in the laboratory of the Zelick workgroup. Fixed samples of the fishes were brought to Bonn for subsequent morphological investigations.

In the course of the research period in Portland several unexpected discoveries were made. None of the single units recorded from the PLLN of *Xiphister* was

mechanosensitive. Instead, all units were sensitive to temperature changes. The spatial filter hypothesis, which suggests that the trunk canal system of *Xiphister* is an adaptation for improved mechanosensitivity could not be confirmed.

The current chapter is a collection of miscellaneous findings made throughout the research project. Starting with the electrophysiological work on goldfish, *Anoplarchus purpurescens* and *Xiphister mucosus* the focus will be on the 2-dimensional receptive field scans. The results of temperature sensitivity tests as well as the general response properties of the recorded units will briefly be documented. Morphological methods such as DASPEI staining of neuromasts as well as SEM analyses were used to clarify the missing responses to hydrodynamic stimuli in *Xiphister*. SEM results are also presented in order to provide a general insight into the anatomy of the *Xiphister* lateral line.

Most of these miscellaneous findings, like the observed temperature sensitivity, are only briefly analyzed because they were not in the focus of the research project. However, they reveal interesting aspects of lateral line physiology and lead to interesting questions for future investigations.

2. Materials & Methods

2.1. Fish collection and housing

Nine goldfish (*Carassius auratus*, 8.8 ± 0.8 cm) were used for the experiments. They were purchased from a local dealer and kept at 18-22 °C in 250 l aquaria with a 12/12 h light/dark cycle in the fresh water facilities of the Zoological Institute in Bonn.

25 specimens of *Xiphister mucosus* (14.1 ± 3.8 cm) as well as 25 specimens of *Anoplarchus purpurescens* (9.6 ± 1.0 cm) were collected in Jaquina Bay (Newport, Oregon; 44°37'3.49"N, 124° 3'27.12"W) during low tides in a vertical range from +0.0 m to +1.0 m outside the water by turning rocks on pebbly substrate and catching the hiding fishes with handnets (c.f. Fig. 24). Some specimens of *Anoplarchus* were caught in tidepools by turning rocks or waving the handnets through seaweed and other algae. Specimens of *Xiphister* and *Anoplarchus* were transported in fish bags with saltwater and seaweed, cooled with ice packs and ventilated with an aquarium bubbler. They were kept in the saltwater facilities of the Department of Biology of the Portland State University in a 150 x 50 x 40 cm tank (w x d x h, temperature 12 °C, salinity 3.5 %, 12/12 h light/dark cycle) and fed with blackworms (*Lumbriculus variegatus*).

Fig. 24 Catching *Xiphister* at Jaquina Bay (**a**) Overview of the collection site at the South Jetty, Newport bridge in the backgound. Tide level at approx. +0.5 m. Animals were caught outside the water by turning rocks (**b**,**d**) on pebbly substrate (**c**). The multiple, complex trunk lateral line canals and the pores were visible to the naked eye (**e**).

2.2. Electrophysiology

2.2.1. Anesthesia and artificial ventilation

Experimental animals were caught from the housing aquaria with handnets and transferred into a bin with 1 l of water and 1 % of MS 222 (3-aminobenzoic acid ethyl) for initial anesthesia. As soon as the animals ceased to react to slight pinching with tweezers they were paralyzed by injecting pancuronium bromide (0.25 µg / g bodyweight). Prior to the surgery, Xylocain was applied superficially to locally anesthetize the skin at the operation site.

For artificial ventilation (Fig. 25) a silicone tube was tightly fitted into the fish's mouth providing an adequate flow (20 – 80 ml/h, depending on the size of the fish) of cooled water (13 ± 0.5 °C; for goldfish the tank water was kept at room temperature) over the gills. A peristaltic pump (Hyflow, Platon, Flowbits ltd., Basingstoke, UK) pumped the water out of the experimental tank, through a salt water resistant brass loop system embedded in a cooled aluminum block, a temperature sensor (Typ 4028, Ultrakust, Hattingen, Germany) and through the mouth and the gills of the fish back into the tank. This method ensured a constant tank water level. The aluminum block was cooled by means of a peltier element that was powered by a laboratory power supply. The peltier element was sandwiched between the aluminum block and a heat sink to carry away the waste heat. The heat sink was cooled with tab water. The temperature (monitored by the temperature sensor) was manually controlled by adjusting the DC voltage of the laboratory power supply that powered the peltier element and the flow rate of the tap water that carried away the waste heat.

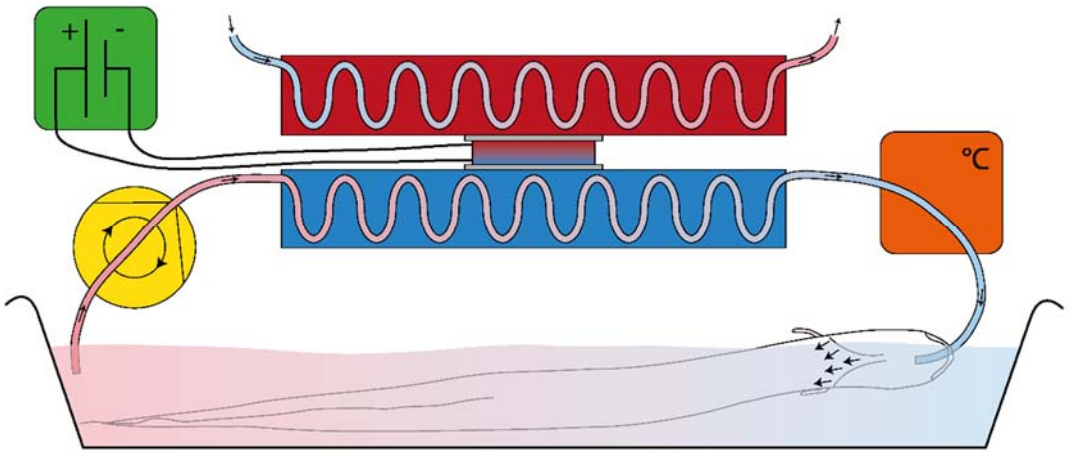

Fig. 25 Artificial ventilation A peltier element (in the center of the drawing) powered by a laboratory power supply (green) was used to cool an aluminum block (blue). A perestaltic pump (yellow) pumped water from the experimental tank through salt water resistent brass cooling loops embedded in the cooled aluminum block through a temperature sensor (orange) and into the mouth of the fish (lying on its side) providing a flow of seawater over the gills. A second aluminum block (red) was cooled by perculation of tab water from the laboratory faucet into the sink and attached to the hot side of the peltier element to carry away the waste heat.

2.2.2. Surgery

After initial anesthesia fish were transferred to the experimental tank, positioned on the side with approx. the first anterior quarter of the body being out of the water to expose the operation site behind the operculum. Extruded polystyrene foam (XPS) served as a base layer on which the experimental animal was fixed with needles and strips of paper tissue (cf. Fig. 26c).

In *Xiphister*, a scalpel was used to cut the skin right behind the operculum in the shape of an X (cf. Fig. 26a). Because the dorsal or medial lateral line canal was cut, the resulting triangular pieces of skin were folded back onto the fish surface and fixed with superglue (UltraGel, Pattex, Düsseldorf, Germany). This procedure ensured that no salt water contaminated the operation site by leaking through the cut lateral line canals. Subsequently the wound was protected and isolated from the surrounding salt water by forming a ring of superglue around the operation site (cf. Fig. 26d). In goldfish (where the trunk canal was destroyed by removing the scales at the operation site before cutting the skin; cf. Fig. 26b) and *Anoplarchus* (no trunk canals present), a rectangular piece of skin was removed with fine scissors and tweezers and a ring of superglue was formed.

In goldfish, the PLLN runs superficially under the skin and parallel to the trunk canal. The nerve was visible after removing the scales and skin behind the

operculum slightly above the trunk canal (c.f. Fig. 26b). The superficial branch (ramus superior) of the PLLN of *Xiphister* and *Anoplarchus* runs parallel to the dorsolateral trunk canal (respectively the dorsolateral row of SNs in *Anoplarchus*, c.f. Fig. 26a). This nerve branch was also visible when the skin was removed. The deeper branch (ramus inferior) of the PLLN runs parallel to the mediolateral trunk canal (respectively the mediolateral row of SNs in *Anoplarchus*, c.f. Fig. 26a). It is embedded 1-2 mm deep inside the septum that separates epaxial and hypaxial muscles. The nerve was exposed by carefully pulling away the muscle and connective tissue with tweezers. When the respective branches of the PLLN was approached, the epi- and perineurium were penetrated with a pair of fine tweezers to expose the nerve fibers. Ringer's solution (Appendix A) was used to prevent the operation site from desiccation.

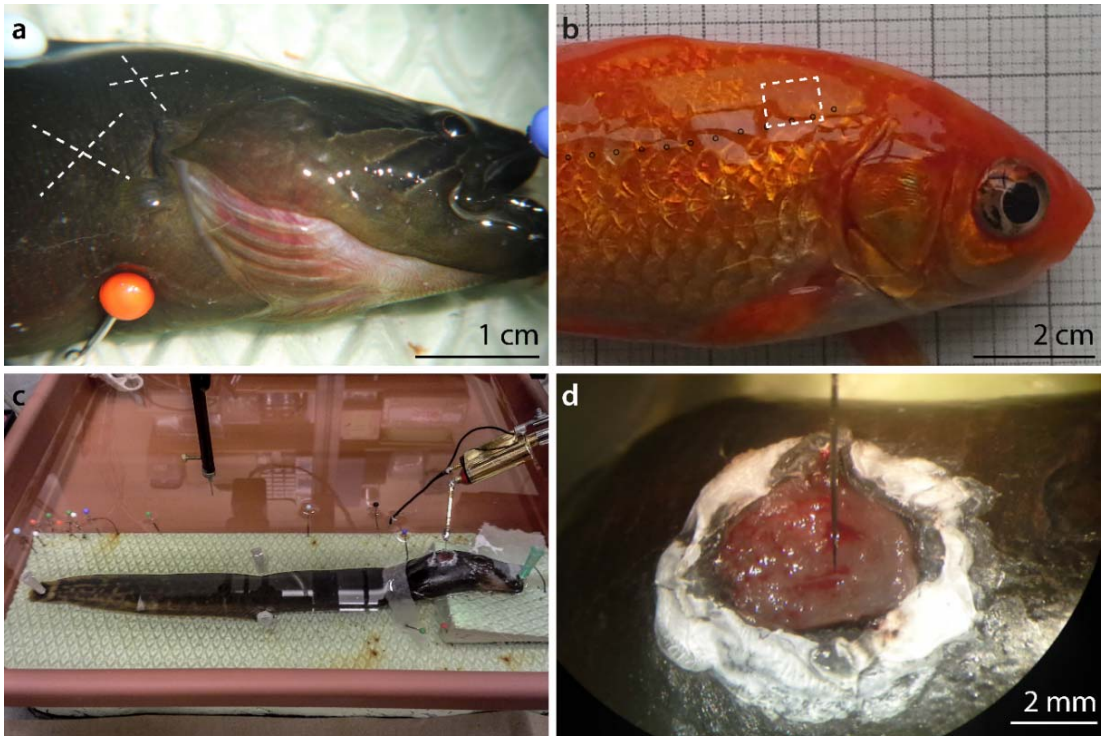

Fig. 26 Surgery (**a**) Head region of *Xiphister*, dashed lines indicate the X-shape cuts above the ramus superior (dorsal) and the ramus inferior (medial). (**b**) Goldfish, dashed rectangle indicates the area where scales and skin were removed, lateral line pores are marked by black circles. (**c**) *Xiphister*, fixed on extruded polystyrene foam (XPS) by means of needles and strips of paper tissue. Approx. the first anterior quarter of the body was above the water surface to expose the operation site. (**d**) Operation site in *Xiphister* showing the white ring of superglue and a metal hook electrode.

2.2.3. Recording

Metal hook electrodes

Nervous activity from the PLLN was predominantly recorded with metal hook electrodes. The electrodes were custom fabricated from stainless steel insect pins (diameter 0.1-0.2 mm) or used neurophysiological tungsten electrodes. Under visual control by means of a dissecting microscope the tip of the metal needles was pushed against a rigid surface to bend the tip into a tiny hook (cf. Fig. 27a). Size and shape of the hook were determined by the shape of the metal needle rather than the bending process: a thin but short tip was needed to get a thin and small hook. The fabrication of the electrodes was crucial for a successful recording. Not only the shape and size of the hook, but also the material or even the surface of the metal influenced recording success. In addition, the electrodes worked differently in different species. For instance, stainless steel insect pins of the same size and shape but from a different batch with a slightly different color, worked both well in *Anoplarchus* whereas only one type of electrode worked in *Xiphister*. However, to successfully record with metal hook electrodes it was important to try out different types of needles and materials until the right electrode was found. Once that was the case, recordings were easy and reliable and the durability of the electrodes was high.

The electrodes were soldered to a gold connector that was plugged into the head stage of the DAM 80 amplifier (World Precision Instruments, Sarasota, USA). The head stage was mounted to a 3-axes-micromanipulator (M3301R, World Precision Instruments, Sarasota, USA). To load only a few nerve fibers onto the hook, the hook was positioned close to the nerve and few fibers were lifted onto the hook with fine tweezers. A more reliable method was to drive the hook into the nerve before lifting it back up. With a sufficiently small hook only a few fibers were loaded onto the hook. By slightly moving the hook parallel and perpendicular to the longitudinal axis of the nerve the fibers could be separated and electrically isolated from the rest of the nerve. For a successful recording it sometimes was necessary to rise or lower the level of the ringer's solution around the nerve. Recording success depended on manual skills and needed some training and experimenting with the different techniques but finally was successful and reliable. Several units could be recorded from one experimental animal.

Hook electrodes provided single or few (distinguishable) unit recordings of reasonable s/n-ratio (up to 10/1). In some cases multi unit recordings were obtained. Recordings were robust and lasted for up to 4 hours. The main reason for losing a unit was an unstable level of ringer's solution. The electrodes eventually were shortened or the nerve dried out.

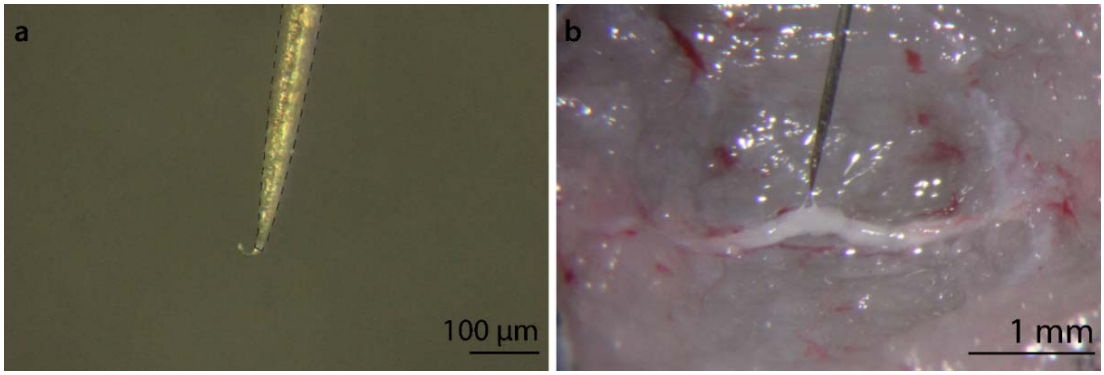

Fig. 27 Recording with metal hook electrodes (**a**) Tip of a tungsten electrode bent to a small hook, the dashed line indicates the coated part of the electrode. (**b**) Electrode in the vicinity of the PLLN. Some nerve fibers are loaded onto the hook.

Suction electrodes

Suction electrodes were used to record multi unit activity from the PLLN. Glass micro-pipettes (GB150F-8P, Science Products, Hofheim, Germany) were pulled (P-87-Brown/Flaming, Sutter Instrument Company, Novato, USA) and the tip of the electrode was manually broken off so that the inner tip diameter matched the nerve diameter (about 200 µm, crucial to ensure electrical isolation necessary for recording of neural activity). The glass micro-pipette was attached to an electrode holder with a suction port. The electrode holder was plugged into the head stage that was attached to the 3-axes-micomanipulator. A syringe with Ringer's solution was connected to the suction port of the electrode with silicone tubing. The entire system (syringe, tubing, electrode holder and electrode) was filled with Ringer's solution. The nerve was cut and the distal end of the nerve was sucked into the electrode.

Suction electrodes provided multi unit recordings that were stable for up to one hour. The recording method was used while search stimuli of different modalities were applied.

Electrophysiological setup

Signals were amplified (DAM 80, World Precision Instruments, Berlin, Germany; band pass filter 300-3,000 Hz, 1,000 x), 50 Hz respectively 60 Hz hum noise filtered (Hum Bug, Quest Scientific, Vancouver, Canada) and digitized with an AD/DA converter (Micro 1401, CED, Cambridge, England; 16-bit resolution, 5 kHz sampling rate). Neuronal activity was audio-monitored via headphones and stored and monitored on a PC using the Spike2 Software (Version 7.16, CED, Cambridge, England).

To achieve stable recordings and defined hydrodynamic stimuli the experimental tank and the micromanipulator that held the electrode rested on a vibration isolated table (Micro-g, TMC, Peabody, USA).

2.2.4. Hydrodynamic stimulation - Receptive field scan

2.2.4.1 Search stimuli

Once neuronal activity was recorded, we applied weak water jets to the fish trunk from a Pasteur pipette to test for mechanosensitivity. The position that led to the largest response was determined with the aid of the audio-monitor.

Alternatively the spherical tip of a pin needle that was glued to the membrane of a small loudspeaker served as a stimulus source, creating sinusoidal water motions and pressure fluctuations. This stimulus could be applied at different locations near the fish surface manually in order to find the most sensitive spot. The loudspeaker was driven by a function generator (Model 2100, Krohn-Hite, Brockton, MA, USA) connected to an AC amplifier (467A Power Amplifier, Hawlett-Packard, Palo Alto, CA, USA). Amplitude and frequency of the search stimulus could be varied as needed. In most cases 50 Hz stimuli were applied.

2.2.4.2 Stimulus apparatus

To precisely measure the receptive fields of mechanosensitive units we built an apparatus that allowed to scan the receptive field of a unit automatically.

Dipole source

In this apparatus, vibrating cylindrical brass rods (diameter 0.5 and 1 mm) or plastic spheres mounted on brass rods (diameter 3, 4 and 5 mm) were used as dipole source (c.f. Fig. 28b). These exchangeable tips were mounted on a carbon

rod attached to a mechanical shaker (VT-20 Shaker 20N, Sigmatest, Gottmadingen, Germany; c.f. Fig. 28a). An acceleration sensor (ADXL330, Analog devices, Norwood, MA, USA) glued to the carbon rod and connected to the AD/DA-converter (Micro 1401, CED, Cambridge, England) was used to monitor the acceleration of the vibrating object. The shaker was driven by an AC power amplifier (PA75-2CH, Sigmatest, Gottmadingen, Germany) that was connected to the AD/DA converter (Micro 1401, CED, Cambridge, England). Stimuli of different amplitudes and frequencies were programmed (Matlab Version 7.8.0, The Mathworks, Inc., Natrick, MA, USA) and triggered (Spike2 Software, Version 7.16, CED, Cambridge, England) with the PC. The axis of vibration was oriented vertically such that the dipole vibrated perpendicular to the surface of the fish that was positioned horizontally on its side (c.f. Fig. 28d).

3-axis-CNC-manipulator

The shaker was mounted to a set of three perpendicularly oriented linear guides allowing to move the dipole source in three directions (c.f. Fig. 28d for axes definition). The linear guides were driven by stepper motors (X/Y-axis: QSH4218 Trinamic Motion Control, Hamburg, Germany; Z-axis: E7123-0140, Emis, Weiden, Germany). The stepper motors were connected to a 3-axis stepper motor control unit (SMC-TR-1000, Emis, Weiden, Germany) powered by a 24 V lab power supply. The movement was controlled with step and direction signals from the digital output of the AD/DA converter. The signals were programmed in the Spike2 sequencer module and could be adjusted and triggered by a graphical user interface based on a Spike2 script or by predefined keyboard commands.

The maximum travel distance of the CNC-manipulator was 170 mm in X-direction, 65 mm in Y-direction and 500 mm in Z-direction. The spatial resolution of movement was 0.1 mm. Movement velocity was 4.2 mm/s in X- and Y-direction and 3.9 mm/s in Z-direction. The reason for these low speeds was that no controlled and constant acceleration and deceleration could be effectively implemented in the Spike2 sequencer module. For the line scan procedure (c.f. Fig. 30b) the speed in X- and Y-direction was reduced to 0.8 mm/s. Finally, software limitations did not allow to move the dipole source in multiple directions simultaneously. This restricted the movement to rectangular paths only.

The entire stimulation device was rigidly suspended above the vibration-isolated table with aluminum profiles (40 x 40 mm, item Industrietechnik GmbH, Solingen, Germany) that were attached to the frame of the vibration-isolated table. Hence, the entire stimulus device was mechanically separated from the experimental tank.

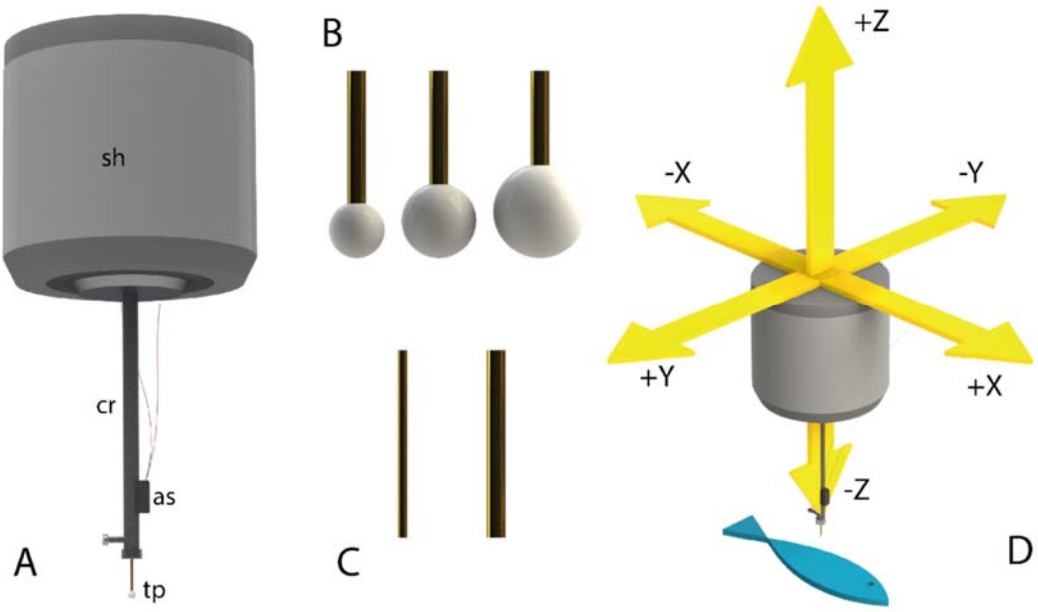

Fig. 28 Stimulus device (**a**) Shaker (sh) with carbon rod (cr), accelaration sensor (as) and exchangeable 3 mm sphere tip (tp), held by a small screw. Cylindrical brass rods (diameter 0.5 and 1 mm; **c**) or plastic spheres mounted onto brass rods (diameter 3, 4 and 5 mm; **b**) were used as stimulus source. (**d**) Axis labelling wih respect to the alignement of the experimental animal. The axis of vibration corresponded to the Z-axis.

2.2.4.3 Experimental procedure

Once a hydrodynamic unit was encountered, the X- and Y-position of the dipole source was adjusted to the center of the receptive field that was approximated with the aid of the manual search stimulus. The tip of the dipole was lowered under visual control until it barely touched the skin. Thereafter it was raised in Z-direction by 3 mm. It remained at this Z-level during the scans.

Dipole stimulation

In order to determine basic response properties of a unit (frequency response, dynamic amplitude range and adaptation characteristics) a dipole stimulation procedure was presented prior to the receptive field scans.

The procedure started with two 60 s sweeps, one with increasing (from 20 to 200 Hz) and the other with decreasing frequency (from 200 to 20 Hz). A

constant acceleration amplitude was achieved by calibrating the output signal of the AD/DA converter that controlled the shaker. This was done by measuring the frequency dependent acceleration of the rod in a test sweep with constant output amplitude. The output signal was then recalculated such that a constant acceleration amplitude was achieved across all frequencies. Slight variations in acceleration amplitude as those at the beginning of the sweep depicted in Fig. 29a (respectively at the end of the sweep depicted in Fig. 29b) were caused by the resonance properties of the setup that depended on the positions of the dipole source relative to its position during the calibration process that was only done once. Sweeps were used to quantify the frequency response of a unit.

In a second set of dipole stimuli short sine pulses with a fixed frequency and 5 different amplitudes were presented in random order, each stimulus was repeated 5 times (frequency: 50 Hz, duration: 700 ms, rise and fall time: 100 ms, amplitude: 1x, 2x, 4x, 8x, 16x (stimulus amplitudes were defined relative to the lowest amplitude applied), inter-stimulus interval: 2300 ms; c.f. Fig. 29c). These types of stimuli were applied to test if a unit was stimulated within its dynamic range.

The basic dipole stimulation procedure was completed with a single long-term stimulus with constant amplitude and frequency to test the adaptation characteristics of the recorded unit (stimulus frequency: 50 Hz, stimulus duration: 60 or 100 s, rise and fall time: 100 ms, amplitude: 4x; c.f. Fig. 29d).

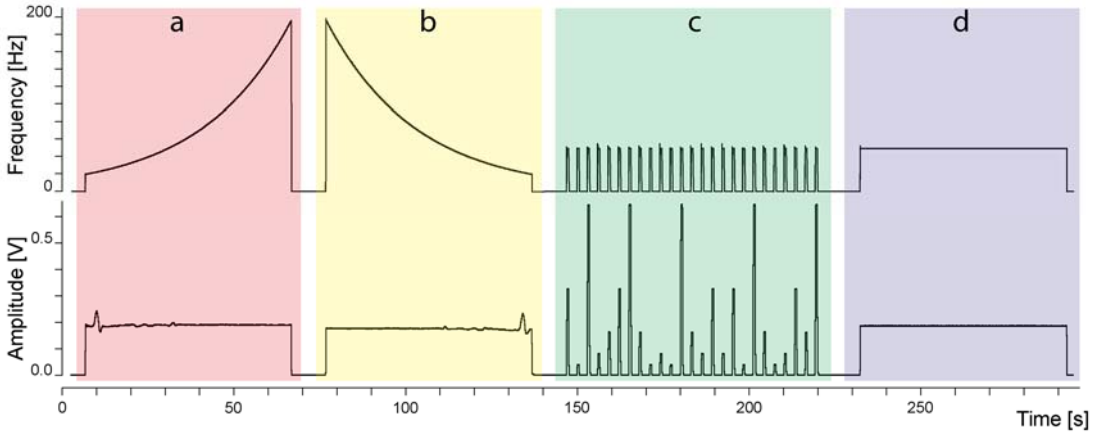

Fig. 29 Basic dipole stimuli. Sweeps of increasing (**a**, red) and decreasing (**b**, yellow) frequency with constant amplitude were followed by sine wave stimuli of various amplitudes but constant frequency (**c**, green) and a long-term stimulus of constant frequency and amplitude (**d**, blue).

Raster scan

The receptive field of a mechanosensitive unit was determined with one of two possible scan procedures. In the raster scan procedure short sine wave stimuli (frequency: 50 Hz, duration: 700 ms, rise and fall time: 100 ms, amplitude: variable (but constant within one scan procedure)) were presented at distinct locations in a raster pattern around the center of the receptive field as approximated by the search stimulus. The dipole followed a zickzack-path resulting in four possible scanning directions: +X, -X, +Y, -Y ("right, left, front, back", c.f. Fig. 30a).

Length and width of the raster field, raster resolution, scan direction as well as stimulus amplitude were set up in the graphical user interface.

Due to variable raster resolutions and the fixed speed of the movement of the scanning device the inter-stimulus intervals varied. However, after the stimulus device reached a scanning location, the procedure was paused for one second to reduce vibration artefacts due to the movement of the device. Subsequently a dipole stimulus was presented.

Line scan

In the line scan procedure an ongoing dipole stimulus (frequency: 50 Hz, amplitude: variable (but constant within one scan)) was presented while the stimulus device moved across the scanning field with a speed of 0.8 mm/s. Like in the raster scan procedure the scanning device followed a zickzack-path resulting in the four scanning directions (c.f. Fig. 30b).

Like in the raster scanning procedure, the length and width of the scanning field, the scanning resolution, the direction of the zickzack-scanning-path as well as the stimulus amplitude were adjusted in the graphical user interface.

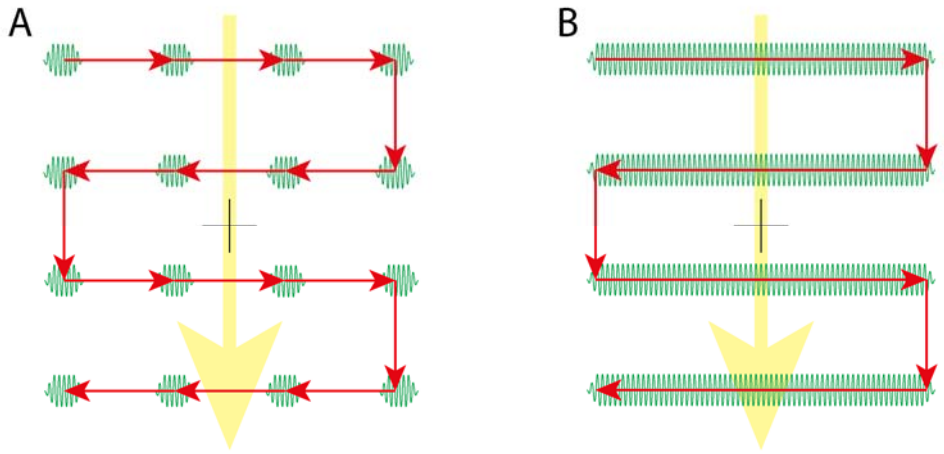

Fig. 30 Scanning procedures (**a**) Raster scan. (**b**) Line scan. Red Arrows indicate the travelling path of the dipole source. Green sine waves indicate the positions at which the dipole stimulus was presented. Black crosses in the center mark the predefined point of interest (approximated center of the receptive field). Yellow arrows show scanning direction. The scanning resolution corresponds to the vertical and horizontal red arrows in **a**, respectively the vertical red arrows in **b**.

2.2.5. Thermal stimuli

Sudden as well as steady thermal stimuli were applied.

Water jets (~10 °C or ~25 °C) that were manually applied with a Pasteur pipette to the trunk of the fish served as sudden thermal stimuli. These stimuli were applied when (1) the fish trunk was submerged or when (2) the water level in the tank was lowered and the fish trunk was emerged in air.

For application of a steady temperature stimulus the fish was always submerged in water. A metal container filled with ice or hot water was placed inside the experimental tank to slowly heat up or cool down the water in the experimental tank. Water temperature was measured with a temperature sensor (model 33, YSI, Yellow Springs, OH, USA) connected to the AD/DA converter.

2.2.6. Other modalities

Occasionally a unit was tested for other modalities. To test for salinity sensitivity, instant ocean salt or distilled water were added to the tank water. To test for mechanoreception (touch), the fish trunk was touched with tweezers or the rubber-back of a Pasteur pipette. To test for proprioception the fish trunk was bend without moving its fixed head region. Hand clapping or knocking against the wall of the experimental tank was used to test for vibration sensitivity or sound reception. Electrical fields were applied to test for

electroreception. Sine signals of various duration, amplitude and frequency from two silver wire electrodes at various distances were used for this purpose.

2.2.7. Data analysis

Action potentials were threshold discriminated with the Spike2 software. Further data analysis was performed in Matlab.

Receptive field scan results were 2-dimensionally (X- and Y-Position) plotted and processed (scaled, smoothed) using the Matlab image processing toolbox.

2.3. Morphology

2.3.1. DASPEI staining

To stain individual neuromasts, fish were immersed in a DASPEI solution (2-(4-dimethyl-aminostyryl)-N-ethyl pyridinium iodide in salt or fresh water) for 30 minutes. Fish subsequently were killed with an overdose of MS 222 and examined under a mercury fluorescence stereo microscope (BH-2, Olympus, Tokio, Japan). Pictures were taken with a digital camera (EOS 550D, Canon, Tokio, Japan) attached to the microscope with a custom fabricated camera adapter.

2.3.2. Scanning electron microscopy

Samples of the skin, the trunk lateral line or the cephalic lateral line of *Xiphister* and *Anoplarchus* were dissected. After dehydration in a graded ethanol series and drying in air the samples were mounted on aluminum stubs and sputter coated with gold. Scanning electron microscopy was done with a Stereoscan S200 (Cambridge Instruments, Somerville, MA, USA).

3. Results

3.1. Electrophysiology

3.1.1. Goldfish

Seven goldfish were used to test and improve the recording method and the 3-axis-stimulation-device. For two single units the responses to dipole stimuli as well as their receptive fields will be shown as a proof of principle of the raster scan method.

Unit 1

Stimulation with 5 stimulus amplitudes revealed that the unit was stimulated within its dynamic range: an increase in stimulus amplitude caused an increase in neuronal activity (c.f. Fig. 31b). The fourth strongest stimulus (8x) was thus used in the subsequent receptive field scan.

If stimulated with a sweep (20 to 200 Hz) the unit responded strongest at 20 Hz. Above 40 Hz the response decreased to 20 % with respect to the strongest responses. Above 100 Hz nearly all neuronal activity diminished (c.f. Fig. 31d).

If stimulated with the 60 s 50 Hz stimulus the response of the unit was phasic tonic. The initial phasic response component lasted for 5 s. Within these 5 s the response decreased by about 50 %. In the following 55 s the response decreased by approx. another 50 % (c.f. Fig. 31f).

The raster scanning procedure was used for the receptive field scan. Fig. 32 exemplifies the spatial response of the unit. Strongest responses were recorded at two distinct spots that were about 4 mm apart in X-direction (anterior-posterior) direction. The results of two receptive field scans obtained with different scanning direction (Fig. 32c,d) are fairly similar. The averaged data thus (Fig. 32e) provides an even more distinct image of the receptive field.

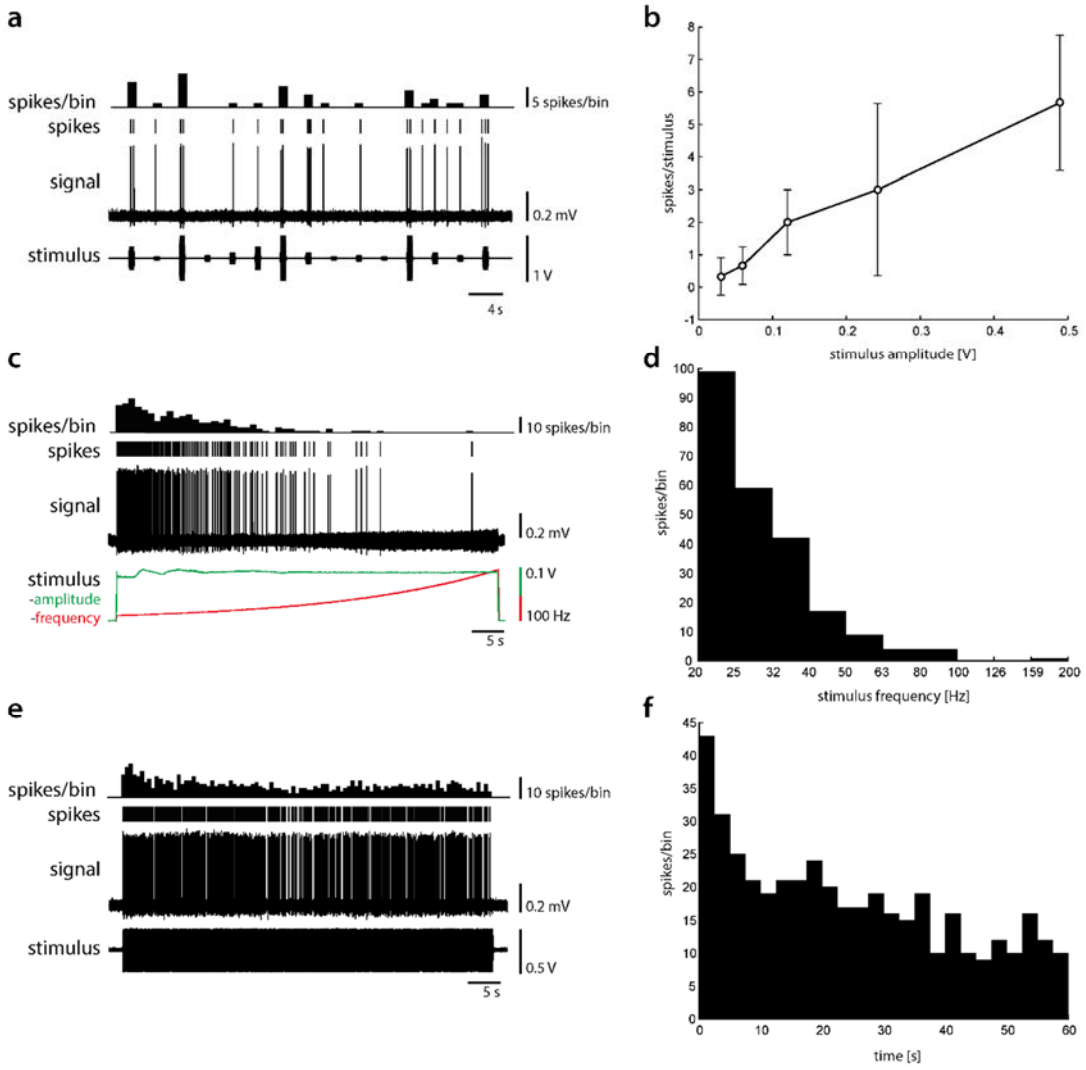

Fig. 31 Goldfish unit 1 - Dipole stimulation Raw data (**a**,**c**,**e**) and results (**b**,**d**,**f**) obtained with dipole stimulation (c.f. 2.2.4.3). (**a**) Raw data of a dynamic range test showing 3 of 5 sets of fixed-frequency dipole pulses with different stimulus amplitudes presented in random order. Bottom to top: dipole acceleration, original recording, spike raster plot, spike histogramm. (**b**) Dynamic range. Mean spikes as function of stimulus amplitude (output voltage of the acceleration sensor). Error bars indicate standard deviation across stimulus repetitions. (**c**) Raw data of the 60 s sweep stimulus. Bottom to top: stimulus amplitude (green) and frequency (red), original recording, spike raster plot, spike histogramm. (**d**) Spikes/bin as function of stimulus frequency. (**e**,**f**) Raw and analyzed data of the 60 s long-term stimulus with fixed stimulus frequency and amplitude.

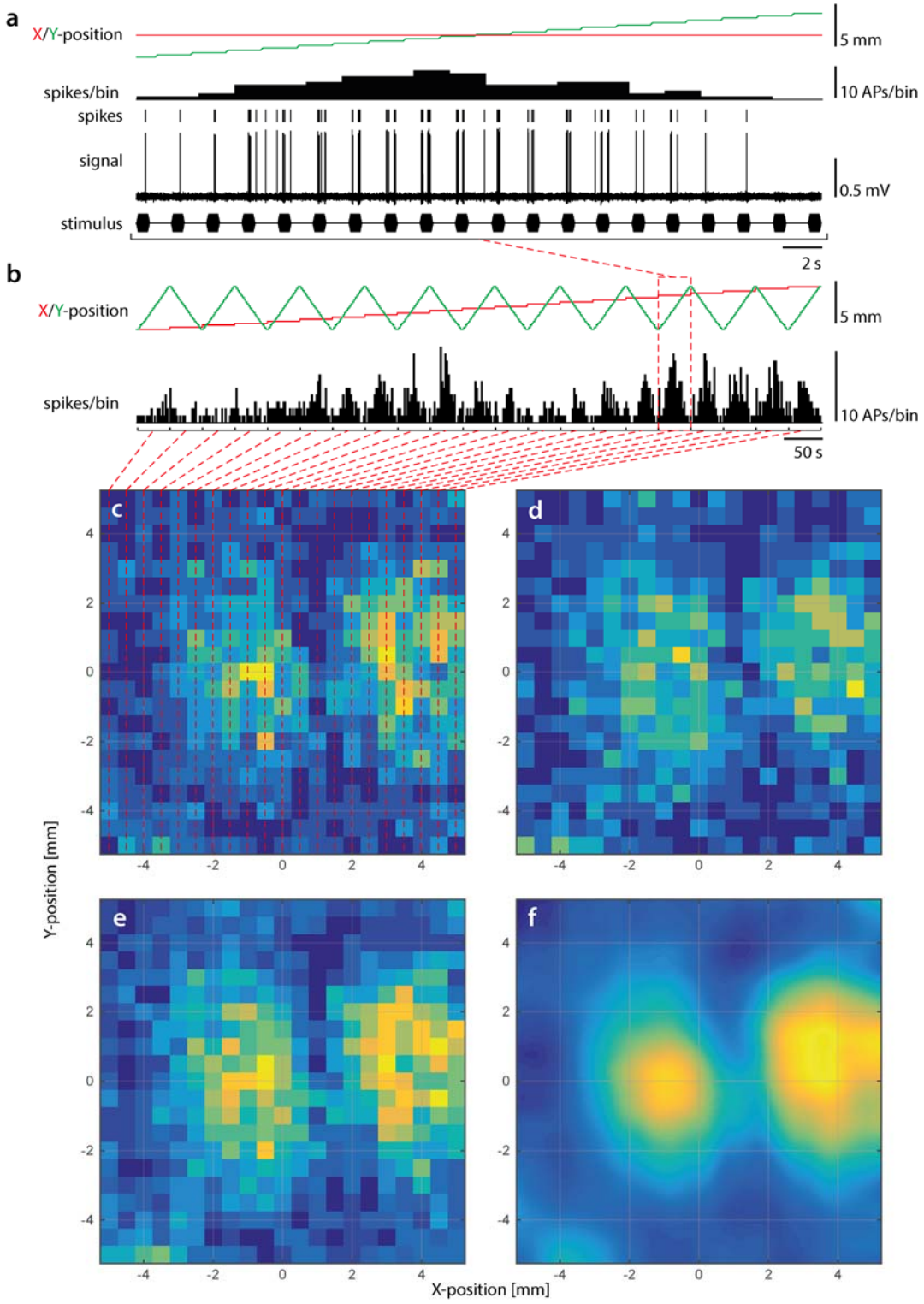

Fig. 32 Goldfish unit 1 - Receptive field scan (**a**) Raw raster scan data. The sphere was moved in Y-direction (constant X-position, red graph). From bottom to top: dipole acceleration, original recording, spike raster plot, spike histogram, X-(red) and Y-position (green) of the dipole source. (**b**) Spike histogram (bottom) and X- and Y position of the dipole source during the entire raster scan. Row after row was scanned in Y-direction. (**c**-**e**) Color coded normalized responses (spikes/stimulus) are plotted against the X- and Y-position of the dipole source. One pixel represents the response to one stimulus. Warm colors represent strong responses. (**c**,**d**) Results of two raster scan procedures with different scanning directions. (**e**) Averaged data. (**f**) Interpolated and smoothed average.

Unit 2

Fig. 33 shows the response of a second unit. The unit was stimulated within its dynamic range. Again, the fourth strongest stimulus (8x) was chosen for the receptive field scan (Fig. 33a).

The unit was stimulated with sweeps of increasing (20 to 200 Hz) and decreasing frequencies (200 to 20 Hz). The sweep with increasing frequency elicited the strongest responses at the lowest frequencies. No response was recorded above 100 Hz. The sweep with decreasing frequency also elicited the highest responses at the lowest frequencies but some neuronal activity was also recorded up to 200 Hz (Fig. 33b).

The 60 s, 50 Hz stimulus did not lead to a phasic tonic response like unit 1 (Fig. 33c). Within the first 10 seconds the unit constantly responded with over 80 % of the response at stimulus onset. In the subsequent 50 seconds the response varied from about 15 to 180 % with respect to the response at the stimulus onset.

The receptive field scans confirmed the results of the first unit. Strongest responses were observed at two distinct spots that were about 4 mm apart in X-direction and on the same Y-level. Between these spots the response decreased. The results of three receptive field scans with different scanning direction (Fig. 33d-f) are fairly similar and again the averaged data (Fig. 33e) provides an even more distinct image of the receptive field. In a fourth receptive field scan the scanned area was extended in X-direction (Fig. 33i,j). This recording did not reveal any further receptive field features despite the two already described distinct spots of increased sensitivity.

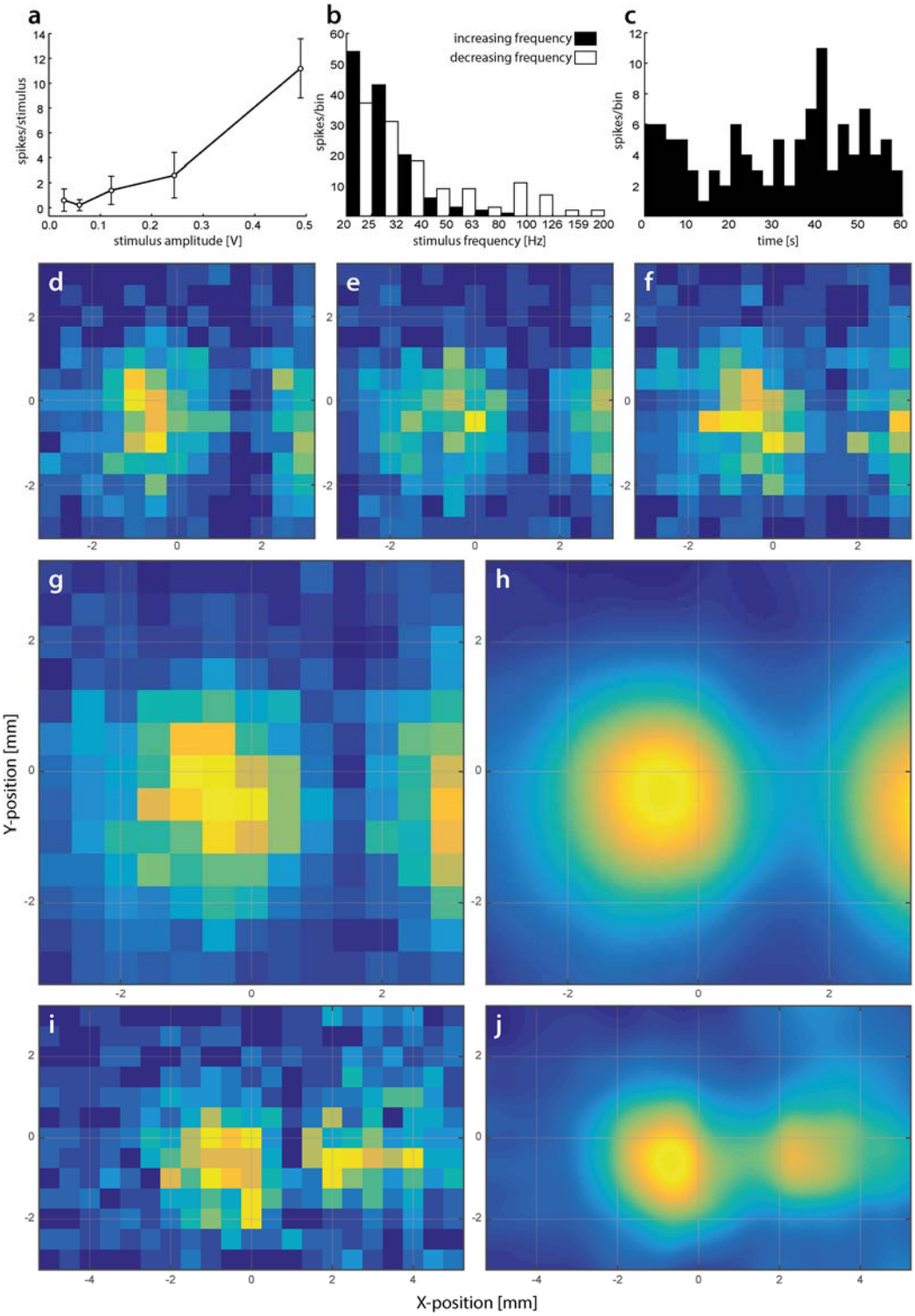

Fig. 33 Goldfish unit 2 – Dipole stimulation and receptive field scan (**a**) Dynamic range. Error bars indicate standard deviation across stimulus repetitions. (**b**) Response to sweeps with increasing (20 to 200 Hz, black bars) and decreasing frequency (200 to 20 Hz, white bars). (**c**) Discharge rate in response to a 60 s 50 Hz stimulus. (**d-f**) Receptive fields determined with different scanning directions. Averaged (**g**) and interpolated and smoothed data (**h**). (**i**) Receptive field scan result of a scanning procedure with horizontally extended scanned field and the smoothed image (**j**).

Thermal stimuli

Peripheral units of goldfish responded fairly similar if stimulated with warm or cold water jets applied with a Pasteur pipette (c.f. 2.2.5). Duration and strength of the neuronal responses were comparable, no matter if cold or warm water jets were applied with the Pasteur pipette (Fig. 34a,b).

However, when a steady temperature stimulus was applied (heating or cooling of the entire water in the experimental tank, no hydrodynamic stimulation), the baseline activity followed the water temperature with a delay of approx. 50 s (Fig. 34c). This delay most likely was caused by the certain distance between the temperature sensor and the recorded neuromast.

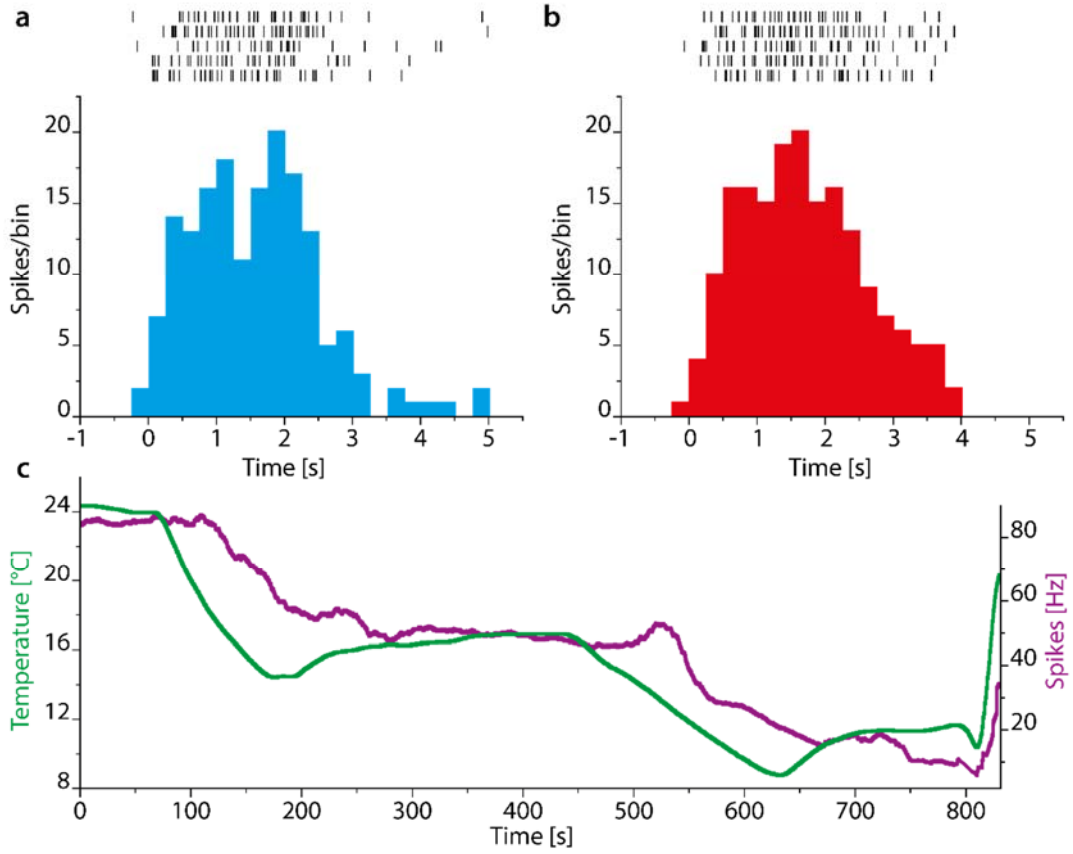

Fig. 34 Goldfish – temperature stimuli (**a**,**b**) Spike raster plots (top) and stimulus histograms to five cold (**a**) and warm (**b**) sudden thermal stimuli. Stimuli were applied with a Pasteur pipette. The trunk of the fish was emerged in air. (**c**) Neuronal activity (purple) during a steady temperature stimulus (green, c.f. 2.2.5).

3.1.2. *Anoplarchus*

Since specimens of *Xiphister* were not available in Portland at the beginning of the research project, initial receptive field scans were conducted on *Anoplarchus*

to test the setup. To reduce the scanning time, the line scan procedure was developed in the *Anoplarchus* experiments.

Unit 1

The unit shown in Fig. 35 exemplifies the results of the line scan procedure, no basic dipole stimuli were applied. The discharge rate of the neuron increased and then decreased as the slowly moving dipole source crossed the receptive field (Fig. 35a). This pattern repeatedly appeared in the subsequently scanned lines (Fig. 35b). The composition of the data into a 2-dimensional image thus revealed a spot of increased neuronal response – presumably the receptive field of the unit (Fig. 35c).

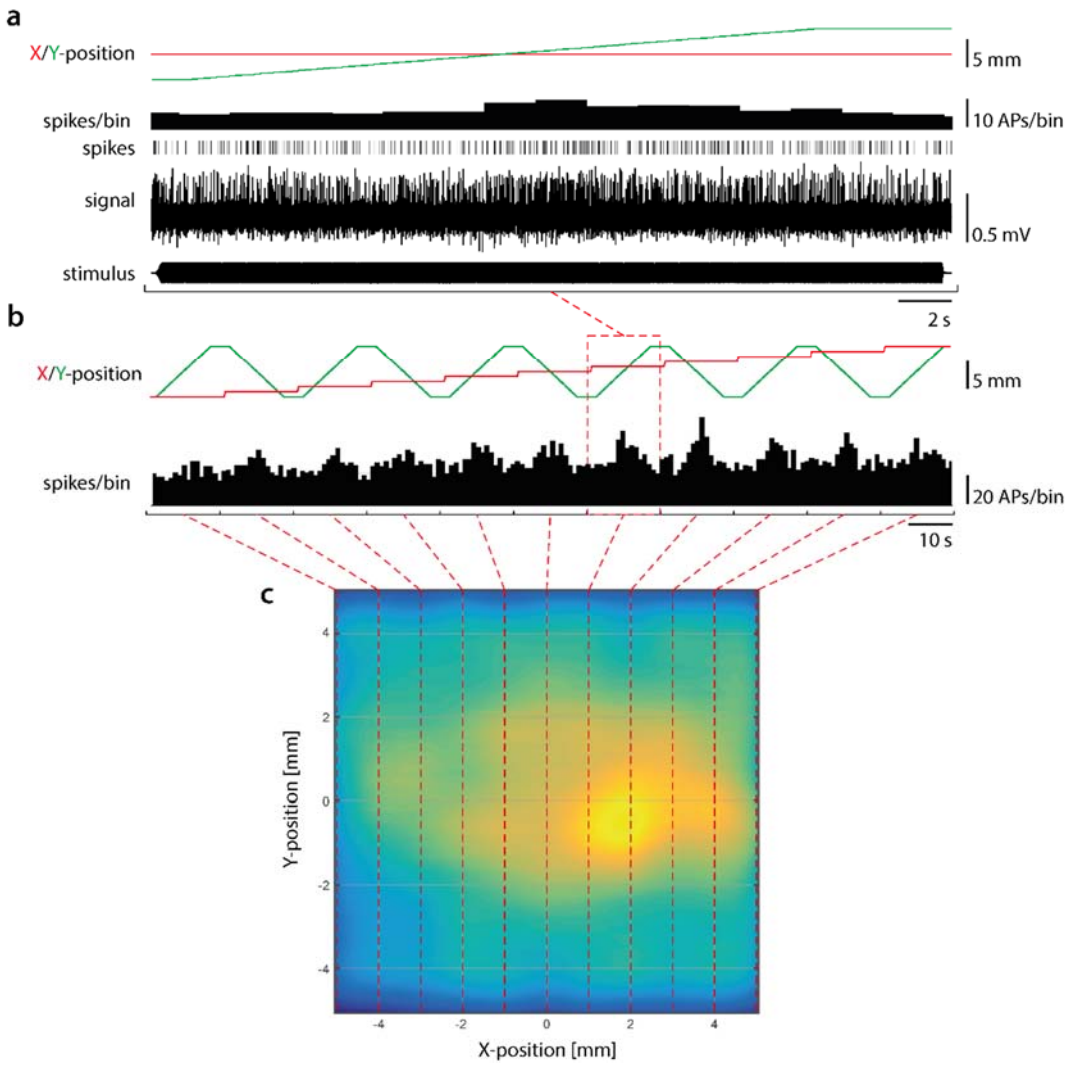

Fig. 35 *Anoplarchus* unit 1 - Receptive field scan Data from the line scan procedure. (**a**) Raw data from a single scanned line. The object was slowly moved along the Y-direction while the shaker constantly vibrated. From bottom to top: dipole acceleration, original recording, spike raster plot, spike histogram, X-(red) and Y-position (green) of the dipole source. (**b**) Spike histogram (bottom) and X- and Y position of the dipole during the entire scan procedure. (**c**) Receptive field of the unit, composed of normalized discharge rate and X- and Y-positions. Warm colors indicate high discharge rates. Black brackets and dashed red lines illustrate the composition of the raw data into the image.

Unit 2

The second unit was stimulated with dipole stimuli and the receptive field was determined in three line scan procedures.

The unit again was stimulated within its dynamic range (Fig. 36a). However, the strongest stimulus amplitude (16x) was chosen in the subsequent line scan procedures because of the relatively low sensitivity of the unit, as encountered with the audio monitor.

To both the sweep with increasing and the sweep with decreasing frequency, the unit showed the strongest responses at the lowest frequencies (Fig. 36b). The

sweep with the decreasing frequency caused slightly stronger responses, especially at higher frequencies.

When stimulated with a sine wave stimulus with constant frequency (50 Hz) and amplitude (4x) for 60 seconds, the discharge rate of the unit unsystematically varied between 8-18 Hz (20 and 45 spikes/bin, c.f. Fig. 36c).

The receptive field scan revealed systematic data across three successive scans with different scanning resolutions and sizes of the scanned field (Fig. 36d-f). Although the unit showed fluctuating responses, the averaged image of the three scans confirms the presence of an inhomogeneous spot at which the unit repeatedly showed the strongest response (presumably the receptive field of the unit; c.f. Fig. 36g).

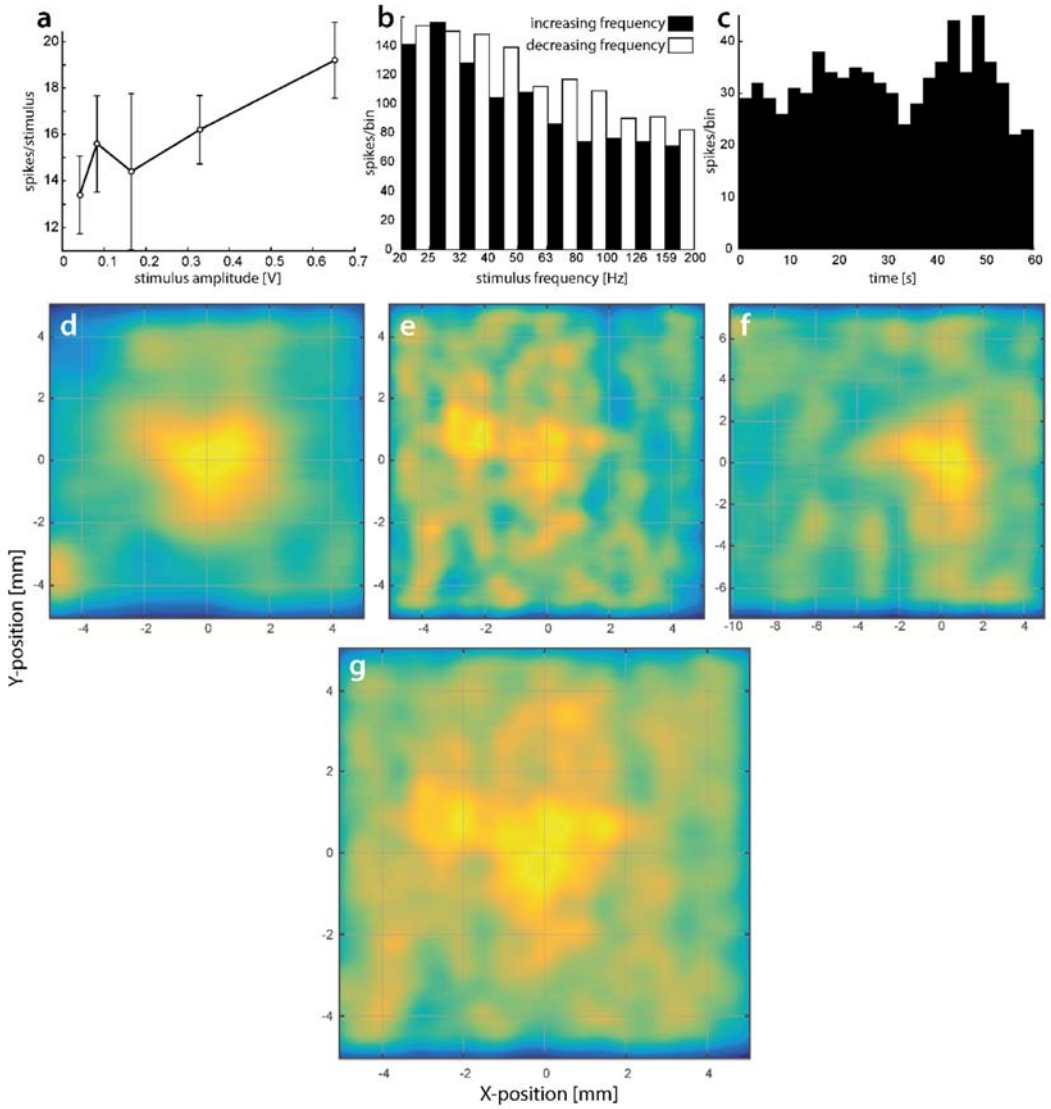

Fig. 36 *Anoplarchus* unit 2 - Receptive field scan (**a**) Dynamic range. Error bars indicate standard deviation across stimulus repetitions. (**b**) Response to sweeps with increasing (black bars) and decreasing (white bars) frequencies. (**c**) The discharge rate in response to the 60 s 50 Hz sine wave stimulus with constant amplitude (4x). (**d-g**) Receptive fields measured with the line scan procedure. (**d**) Scanning resolution = 1 mm. (**e**) Scanning resolution = 0.5 mm. (**f**) Scanning resolution = 1 mm, increased size of the scanned field. (**g**) Averaged data from **d-f**.

Unit 3

The third unit presented was the only *Anoplarchus* unit that was stimulated with the raster scan procedure. Unfortunately, the unit could not be held long enough to finish the entire stimulus protocol. Unit 3 was not stimulated with basic dipole stimuli.

The raster scan procedure in this *Anoplarchus* unit revealed – similar to the raster scans in goldfish – two areas of increased neuronal activity, separated by a distinct area where stimulation elicited only weak responses.

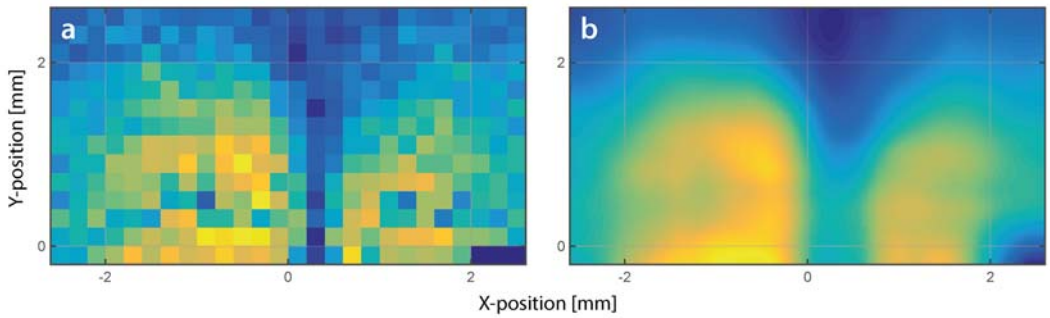

Fig. 37 *Anoplarchus* unit 3 – Receptive field scan Results of an unfinished raster scan procedure. (**a**) Color coded normalized spike rate per stimulus (1 pixel ≙ 1 stimulus). (**b**) Interpolated and smoothed image. Data is missing in the lower right corner since the unit was lost.

3.1.3. *Xiphister*

Responses to hydrodynamic stimuli

The aim of the research project was to measure the receptive fields of PLLN fibers of *Xiphister*.

Unfortunately, in 111 single and 22 multi unit recordings, the various hydrodynamic stimuli applied (c.f. 2.2.4.1) did not elicit any neuronal responses. To verify the insensitivity of the posterior lateral line to hydrodynamic stimuli, whole nerve suction electrode recordings from both branches of the PLLN were made. Fig. 38 exemplifies the results and shows that hydrodynamic stimulation did not alter ongoing activity, i.e. the units were insensitive to hydrodynamical stimulation.

With the exception of the thermal stimuli all other stimuli applied (c.f. 2.2.6) did not elicit a response. However, not all 111 single and 22 multi units were tested with all types of stimuli.

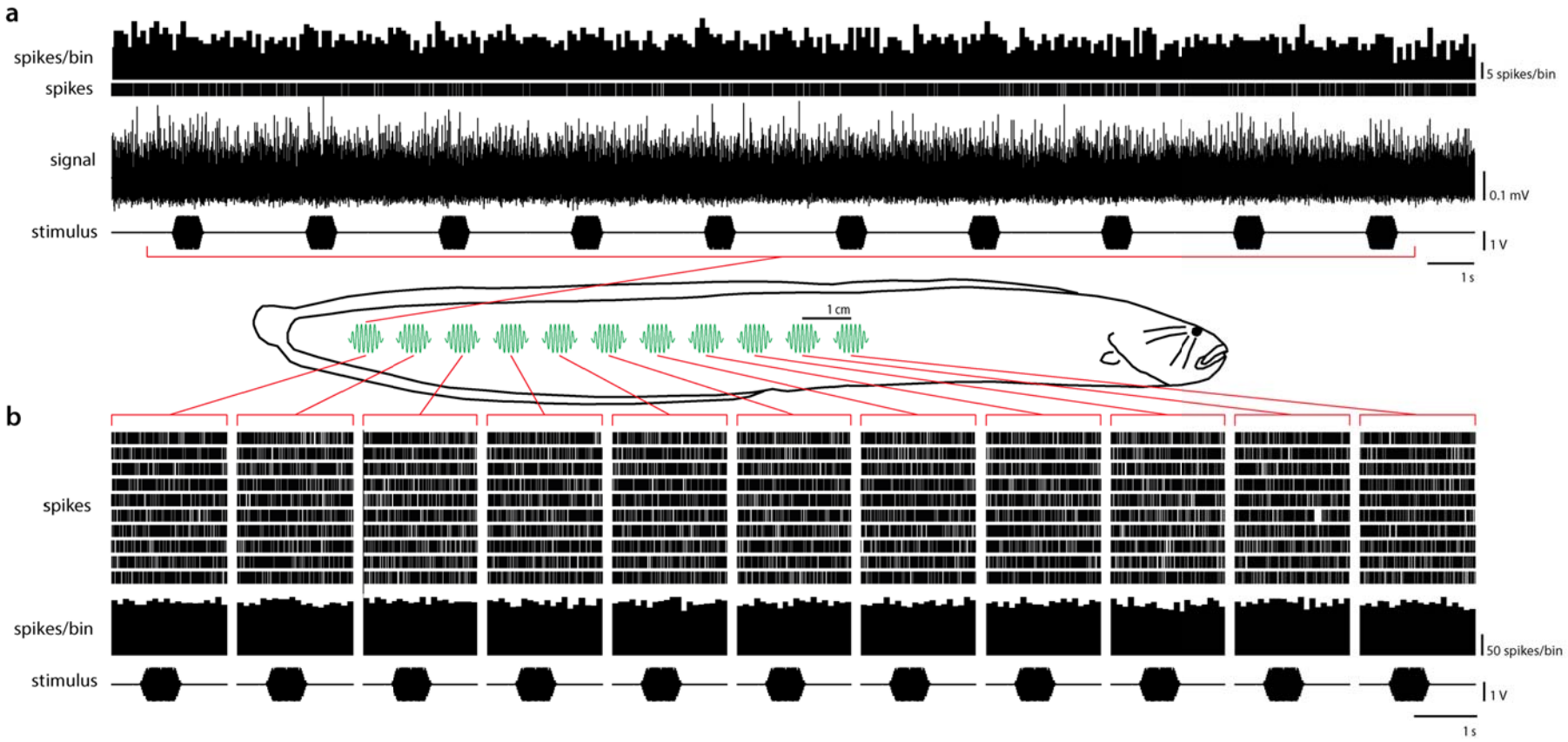

Fig. 38 *Xiphister* – No hydrodynamic response (**a**) Neuronal activity during 10 repetitive 50 Hz pulse stimuli at the most posterior stimulus position. From bottom to top: dipole source acceleration, original recording, spike raster plot, spike histogram. (**b**) PSTHs at each of the stimulus positions. From bottom to top: dipole source acceleration, spike histogram and spike raster plot. Schematic drawing of Xiphister is not to scale. The anterior part of the body could not be hydrodynamically stimulated because it was emerged in air. A 5 mm plastic sphere was used as a dipole source and the strongest stimulus amplitude (16x) was applied.

Discharge patterns

All 111 single units showed ongoing activity, mainly between 1 and 40 Hz. About 40 % of the units elicited fairly constant discharge rates (Fig. 39a,b). Another approx. 30 % of the units showed bursting discharge patterns (Fig. 39c,d). These patterns remained stable for as long as the recording lasted, i.e. in some cases for up to 1 hour. The remaining 30 % of the units elicited varying discharge patterns and could not be classified (c.f. Fig. 40b).

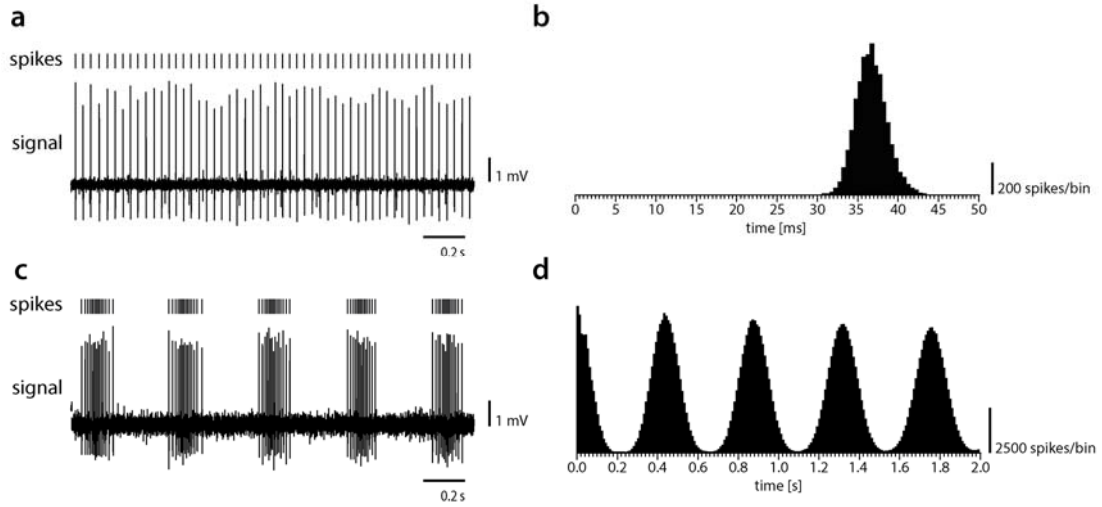

Fig. 39 *Xiphister* – Discharge patterns Original recording (**a**,**c**; bottom) respectively spike raster plots (top) and spike auto correlation (**b**,**d**) of a constantly spiking (**a**,**b**) and a bursting unit (**c**,**d**). Each spike auto corraltion evaluates a 200 second excerpt of the recording.

Nerve cut experiments

While single units were recorded, the whole nerve was cut proximal or distal to the recording site. The activity of some units persisted when the cut was made on distal side (presumably efferents, c.f. Fig. 40a) or when the cut was made on the proximal side (presumably afferents, c.f. Fig. 40b). In one few unit recording (c.f. Fig. 40c) one constantly spiking single unit persisted to fire while the other bursting unit stopped firing after cutting the nerve at the proximal side. However, only a persisting neuron is significant for the interpretation of whether a unit is efferent or afferent. It thus remains part of speculation that we recorded an efferent and an afferent simultaneously. The nerve cut experiments were performed sporadically and do not allow for any quantification (e.g. of the ratio of efferents and afferents) or further conclusion other than that both – afferents and efferents – were recorded.

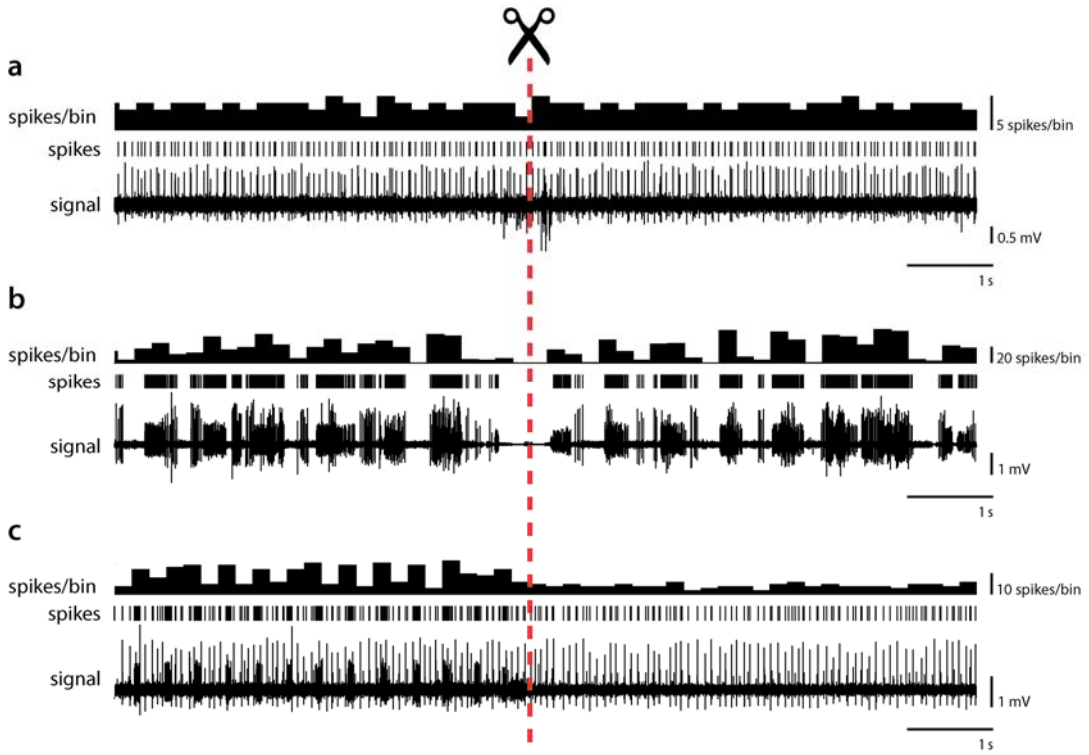

Fig. 40 Xiphister – Nerve cut experiments Original recording (bottom), spike raster plot (center) and spike histogram (top) of three nerve cut experiments (**a**-**c**). While recording nervous activity, the whole nerve was cut distal (**a**) or proximal (**b**,**c**) to the recording site. Red, dashed line indicates time of cut.

Thermal stimuli

In the early experiments, sudden thermal stimuli (c.f. 2.2.5) were applied when the fish trunk was submerged. Neuronal activity never was altered by these stimuli. On the last days in Portland, sudden thermal stimuli were applied while the fish trunk was emerged in air. Thermal stimuli immediately led to neuronal responses.

Fig. 41a-c exemplifies the responses to sudden thermal stimuli: While a warm water jet (~25 °C) led to a decrease of neuronal activity, a cold water jet (~10 °C) caused an increase in neuronal activity. This effect already is apparent in the raw data (Fig. 41a) and becomes even more obvious in the peristimulus time histograms (PSTHs, Fig. 41b,c). After the first unit clearly responded to thermal stimuli, 8 more units in total were tested in 3 specimens, all of which responded in the same or similar way. Due to the expiring time in Portland, no further experiments could be performed.

Hence, the obtained data does not allow for a quantification such as the determination of a sensitivity threshold. However, the data clearly shows that cold water jets increased and warm water jets decreased neuronal activity.

The unit presented in Fig. 41a-c was also stimulated with a steady temperature stimulus. Now the unit responded in the opposite way: with a delay of about 200 s, decreasing steady temperatures led to a decrease of ongoing activity, increasing temperatures increased the ongoing activity (Fig. 41d). As in the goldfish experiments, the delay was most likely caused by different positions of the temperature sensor and the receptive field of the recorded unit. The steady temperature stimulus was successfully applied only once.

Finally, we report that one unit did not only change its discharge rate when stimulated with cold short-term temperature stimuli but apparently also changed the discharge pattern from bursting to more constantly spiking (Fig. 41e).

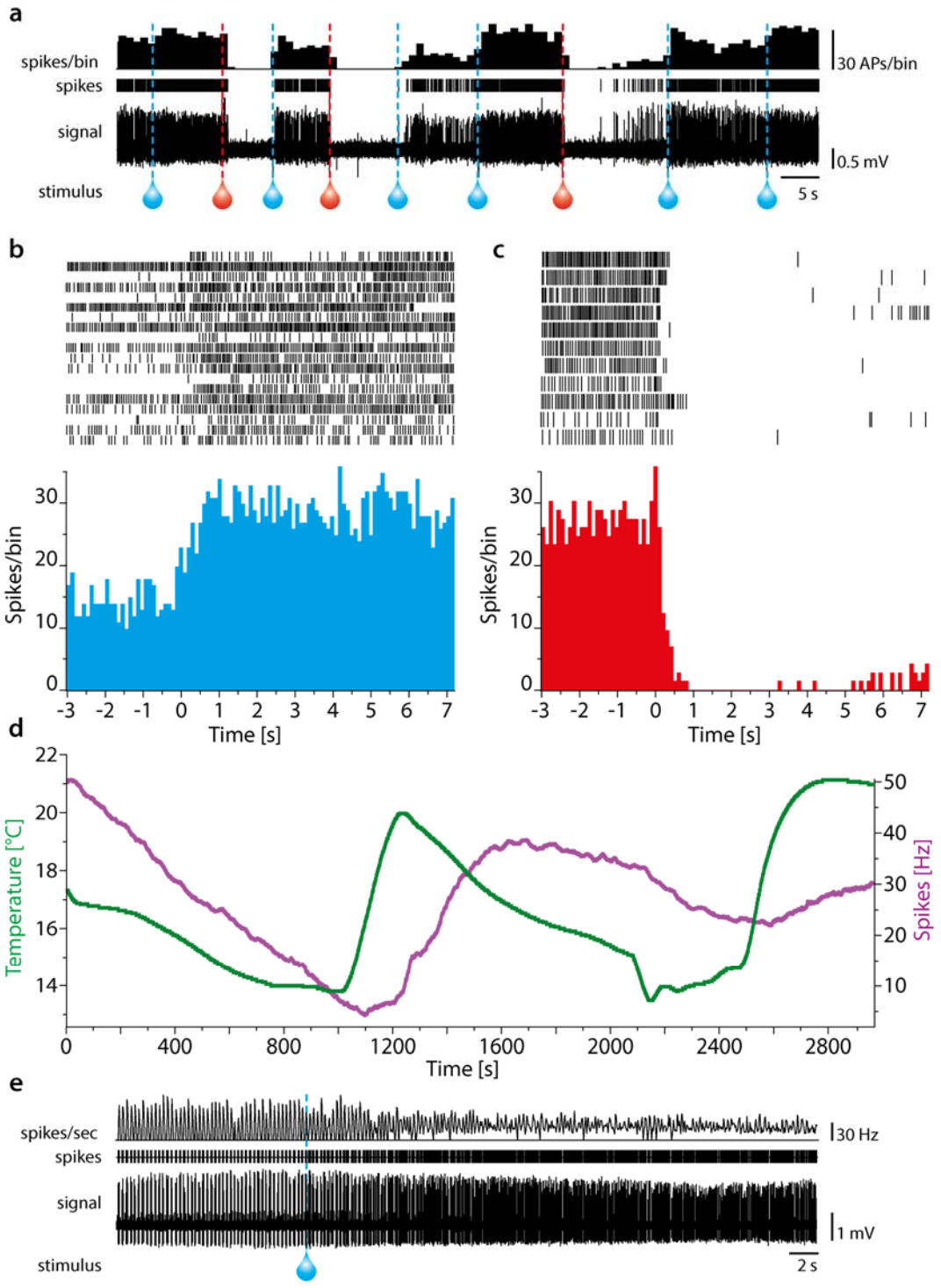

Fig. 41 Xiphister – Thermal stimulation (**a-c**) Response to sudden thermal stimuli. (**a**) Bottom to top: original recording, spike raster plot, spike histogramm. Droplet symbols indicate time of stimulation (blue ≙ cold water stimulus, red ≙ warm water stimulus). Responses to a cold (**b**) and a warm (**c**) stimulus plotted as PSTH. Top: spike raster plot. (**d**) Neuronal activity during steady temperature stimulation (same unit as in **a-c**). (**e**) One unit changed its discharge pattern from bursting to continous spiking in the course of cold water stimulation, applied with a Pasteur pipette.

3.2. Morphology

3.2.1. DASPEI staining

The DASPEI staining in goldfish was performed as control experiments to evaluate our staining procedure. SNs as well as CNs were successfully stained (Fig. 42a). As expected (Beckmann et al., 2010), SNs were visible as dots, mostly in groups of 3 to 5, arranged in vertical rows at the base of the scales. CNs were visible as bright green spots inside the lateral line canal at the base of each lateral line canal scale.

In *Anoplarchus*, DASPEI stained all trunk lateral line neuromasts (Fig. 42c,d). Neuromasts were visible as green dots arranged in horizontal rows and spaced approx. 2 mm apart. The green dots corresponded to small structures that were visible to the bare eye.

In Xiphister no structures were stained with DASPEI (Fig. 42b). Potential CNs could not be visualized with this method.

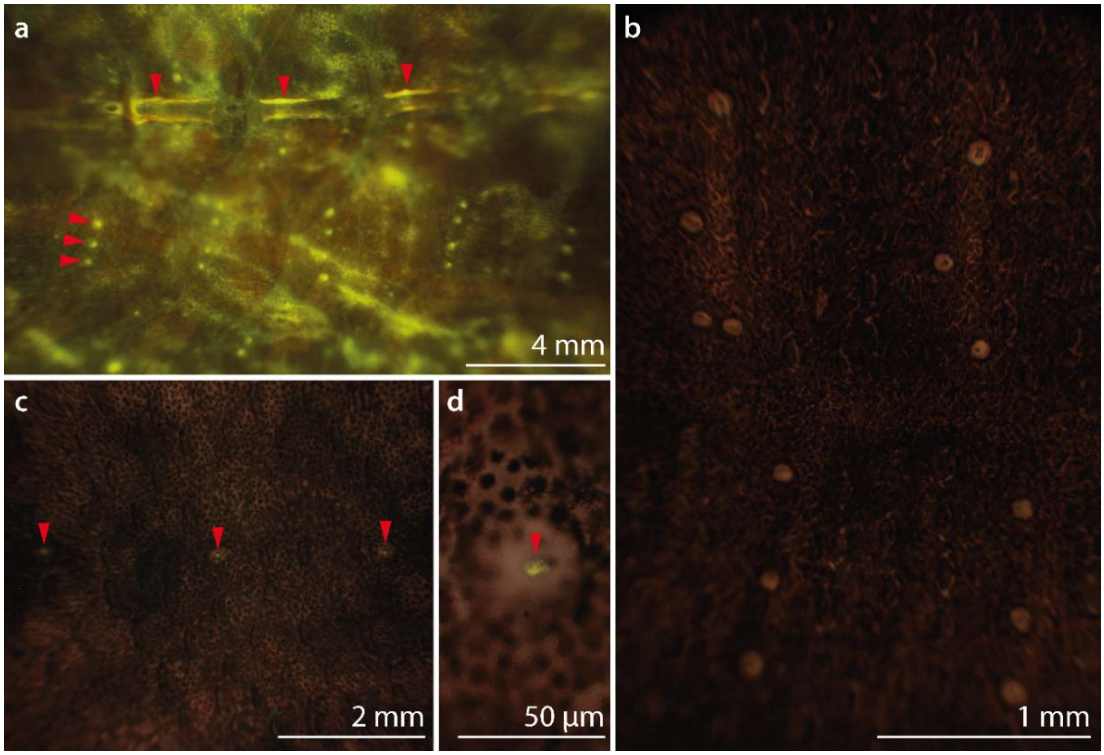

Fig. 42 DASPEI staining DASPEI-staining in goldfish (**a**), *Xiphister* (**b**) and *Anoplarchus* (**c**,**d**). Vertical arrowheads indicate CNs, horizontal arrowheads indicate SNs. Note that in **a** not all SNs are marked with arrowheads.

3.2.2. Scanning electron microscopy

Anoplarchus

Scanning electron microscopy on skin samples of *Anoplarchus* confirmed the presence of lateral line organs on the trunk, as shown by the DASPEI stains (Fig. 43a-c). Neuromasts were arranged in two horizontal rows, spatially corresponding to the dorso- and ventrolateral line canals of *Xiphister* (c.f. Fig. 23) and spaced approx. 2 mm apart. Cycloid scales were only visible on the posterior part of the fish up to about the origin of the anal fin.

The SNs had a diameter of about 20 µm. A notch parallel to the long axis of the fish was visible at the tip (Fig. 43e). The neuromasts were surrounded by a circular crest (approx. 200 µm in diameter) that was dorsally and ventrally slightly extended (Fig. 43d). These extensions were lacking at SNs found in a circular pattern around the nostril of the fish (Fig. 43f,i).

CNs were found in the head canals, e.g. in the infraorbital canal below the eye (Fig. 43g,h). They were diamond-shaped and about 150 µm in width and 110 µm in length (with respect to the long axis of the canal). Perpendicular to the long axis the neuromasts were apparently subdivided into two parts. They were composed of a smoothed outer and a more structured inner compartment. Under high magnification hair cell microvilli bundles were visible (not shown).

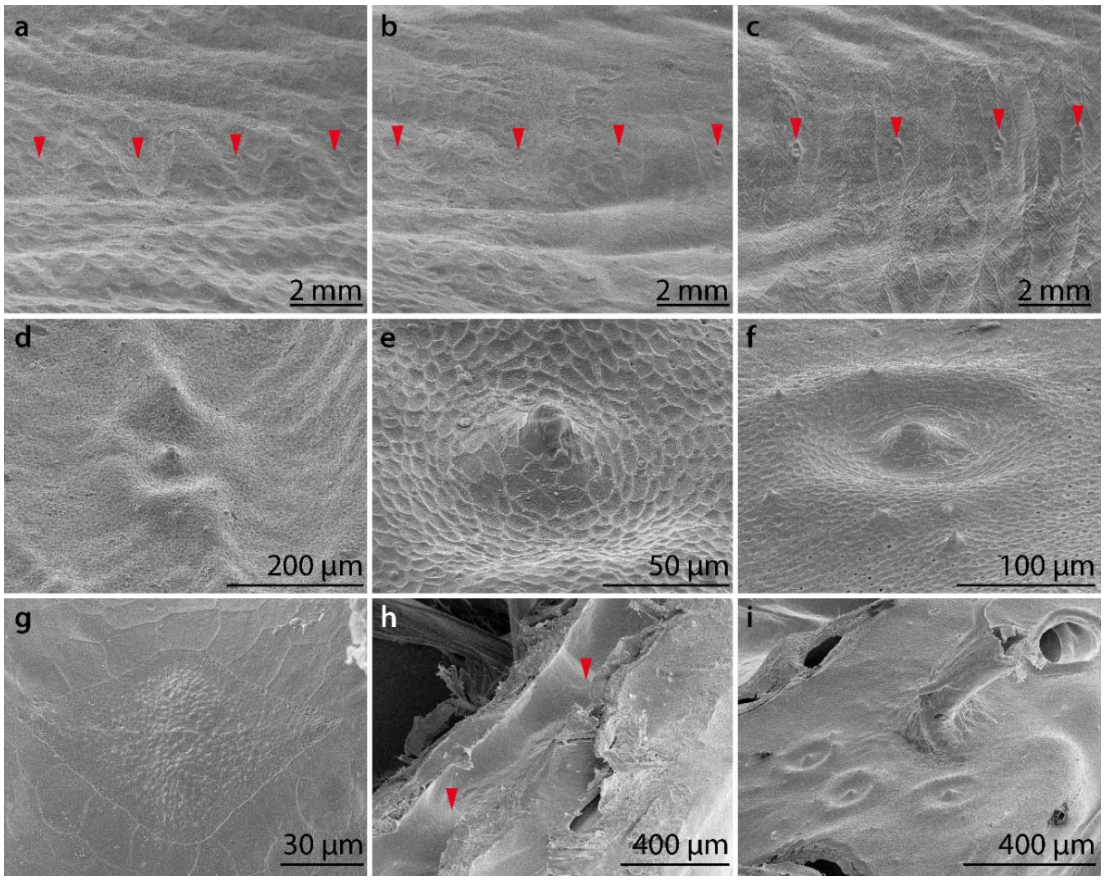

Fig. 43 ***Anoplarchus*** **– Scanning electron microscopy** Skin and scale structure at the posterior (**a**) and anterior (**c**) body part and the transition between both parts at the level of anal fin origin (**b**). Red arrows indicate the position of neuromasts which are well visible at the scale free anterior part of the body. (**d-e**) SN on the fish trunk at different magnifications. (**f**) SN found in a circular pattern around the nostril of the fish (**i**). (**g**) CN located in the cephalic, infraorbital canal (**h**). Red arrows indicate neuromast positions. Vertical axis in **g** corresponds to the long axis of the canal.

Xiphister

In *Xiphister*, cycloid scales were present throughout the entire length of the trunk. In the air dried skin samples used for scanning electron microscopy the pore pattern was visible even with the bare eye. The main canals were visible as slight elevations of the skin (Fig. 44a).

Longitudinal sections of one tubulus (Fig. 44b) of a 12 cm specimen revealed a tubulus length of about 1400 µm. Its diameter slightly decreased from about 200 µm close to the main canal to less than 100 µm at the tip. The depth of the canals with respect to the skin surface also decreased from approx. 100 µm at the main canal to 40 µm at the tip of the tubulus. The main canal was about 400 µm in dorso-ventral and 350 µm in lateral direction. A distinct crest was visible on its lateral side (Fig. 44b).

The bony ring structures that support the trunk canals in *Xiphister* were visible when the skin above the canal was removed with tweezers (Fig. 44c). The method revealed that the rings were not entirely closed at the crest on the lateral side of the main canal (c.f. Fig. 44e).

As in *Anoplarchus*, SNs were located around the nostril of *Xiphister* (Fig. 44h,i). The neuromasts had a diameter of about 30 µm and were embedded in a circular cavity that was approx. 120 µm in diameter and 30 µm deep. In the *Xiphister* samples the notch on top of the neuromast was not as pronounced as in *Anoplarchus*.

CNs were also found in cephalic canals like the infraorbital canal below the eye (Fig. 44d). They were diamond shaped but – in contrast to *Anoplarchus* – were longer than wider (about 150 µm in width and 190 µm in length, with respect to the long axis of the canal; Fig. 44g,j). However, the structural properties of the neuromasts were different: hair cell microvilli bundles were not visible. The surface was almost flat, disrupted only by small, circular indentations.

In the lateral line trunk canals no neuromasts could be identified unambiguously. Two examples of structures that barely looked like neuromasts are shown in Fig. 44k,l. Both structures had a similar surface like the CNs of the cephalic canals. However, they were much smaller (diameter about 50 µm). They were rarely found in the mediolateral line canal. Their presence did not correspond to the branching pattern of the tubuli.

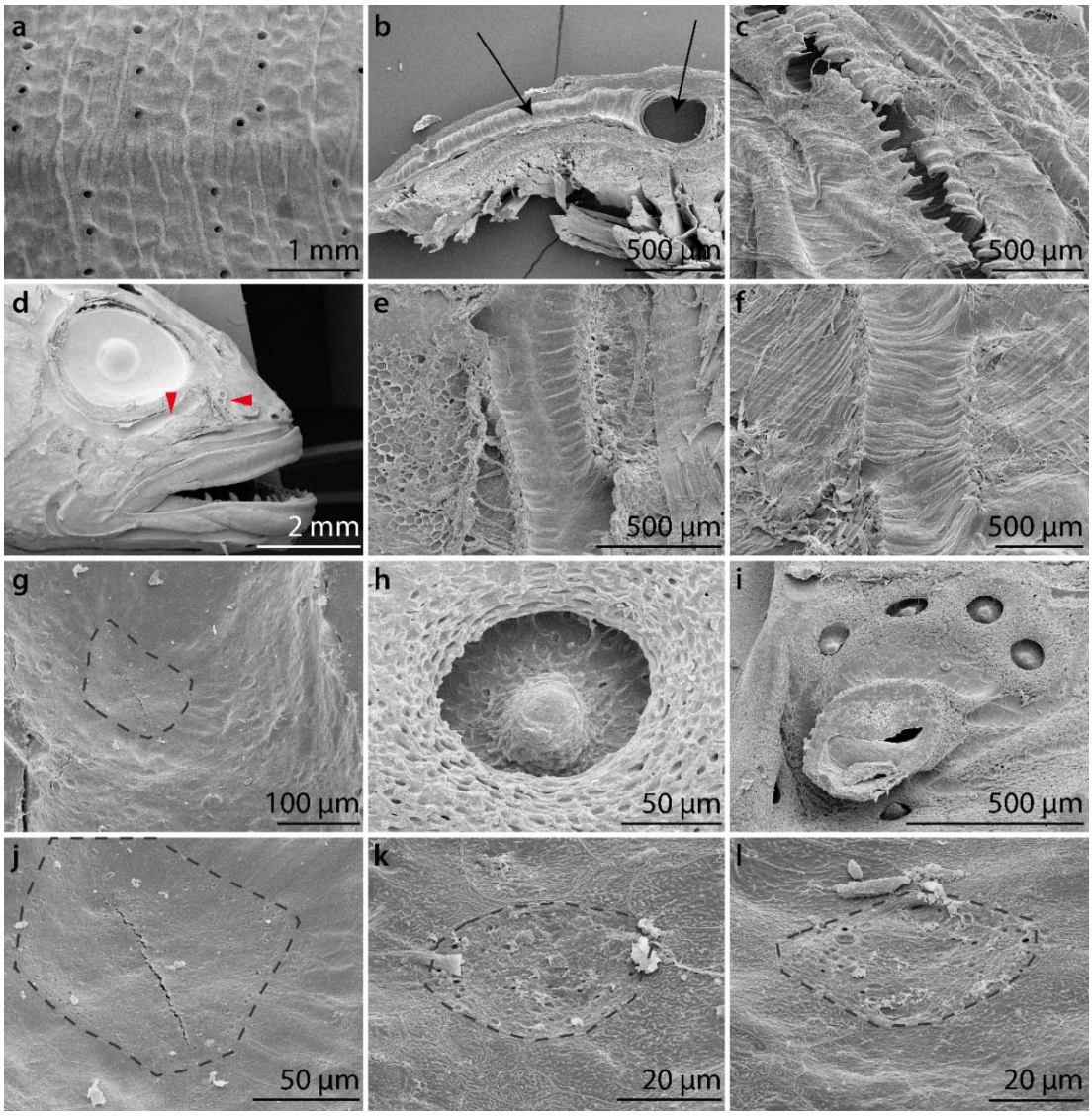

Fig. 44 *Xiphister* – Scanning electron microscopy (**a**) Typical skin structure of *Xiphister* showing the pore pattern, the slightly elevated main canal and scale pattern. (**b**) Longitudinal section of a tubulus (left arrow) respectively a cross section through the main canal (right arow). (**c**) Skin and the attached tubuli were teared away with tweezers uncovering the bony ring structures that support the main canal. (**d**) Overview of the head region and the cephalic lateral line system. Canals were cut open with a razor blade. Vertical red arrowhead indicates the approximate position of the CNs shown in **g** and **j**. Horizontal arrowhead indicates the position of the SNs around the nostril. (**e**) Dissected top part of the main canal with the distinct crest that connects both sides of the bony ringstructures (ringstructures visible as ridge pattern, c.f. **c**). (**f**) Rigdes on the bottom of the main canal formed by the bony ring structures. (**h**,**i**) SNs arranged arround the nostril and situated in distinct circular cavities. (**g**,**j**) CNs in the infraorbital cephalic canal. (**k**,**l**) Structures in the mediolateral line canal that barely looked like CNs. Dashed lines emphasize the respective structures.

4. Discussion

4.1. Receptive fields

4.1.1. Superficial neuromasts

Prior to the receptive field scans, basic dipole stimuli were presented in order to characterize the units and to ensure that units were stimulated within their dynamic range. The sweeps were presented to determine the frequency response characteristics. Stimuli were presented with increasing (20-200 Hz) as well as with decreasing frequency (200-20 Hz). The responses to these two stimuli were slightly different: sweeps with decreasing frequency elicited slightly stronger responses to high frequencies and slightly weaker responses to low frequencies compared to sweeps with increasing frequency (c.f. Fig. 33b). This shows that the neuronal response not only depended on frequency, but also on the temporal order of the frequencies. The units responded strongest to stimulus onset. This is in agreement with the results obtained with the 60 s stimulus with constant frequency and amplitude (c.f. Fig. 29f and Fig. 33b). However, all units showed the strongest response at frequencies below 32 Hz. CNs of trout respond in proportion to water acceleration up to frequencies of about 90 Hz (Kroese & Schellart, 1992). As the neuronal responses to the sweep stimuli (20-200 Hz) constantly decreased with increasing frequency we assume that the recorded units did innervate SNs. For *Anoplarchus* that is expected because this fish lacks a trunk canal system.

4.1.2. Stimulus physics

To explain the two spot receptive fields observed in goldfish (c.f. Fig. 32 and Fig. 33) and *Anoplarchus* (c.f. Fig. 37) it is important to understand the hydrodynamics of the stimulus. A vibrating sphere is commonly used in lateral line research (Coombs et al., 1996). It displaces fluid particles in front of the sphere (with respect to the direction of movement). The displaced fluid particles move on trajectories that are similar to the magnetic field lines (Fig. 45a). In most studies, the sphere vibrated parallel to the surface of the fish. The water flow on the fish surface therefore corresponded to the particle trajectories as seen in side view (view perpendicular to the axis of vibration, c.f. Fig. 45b). In contrast, in the present study the axis of vibration was not parallel but

perpendicular to the fish surface (c.f. Fig. 28d). Thus, the water flow on the fish surface corresponded to the particle trajectories as seen in front view (view parallel to the axis of vibration, Fig. 45c). The particle trajectories radiated from the axis of vibration.

Due to the axial symmetry of the flow field around a dipole source, the particle velocities can be described by the radial, v_r and a tangential, v_t, velocity components according to (Kalmijn, 1988):

$$v_r = -\frac{k^2 r^3}{2D_r} U \cos\theta \cos(\omega t - kD_r) - \frac{kr^3}{D_r^2} U \cos\theta \sin(\omega t - kD_r) + \frac{r^3}{D_r^3} U \cos\theta \cos(\omega t - kD_r) \quad (19)$$

$$v_t = -\frac{kr^3}{2D_r^2} U \sin\theta \sin(\omega t - kD_r) + \frac{r^3}{2D_r^3} U \sin\theta \cos(\omega t - kD_r) \quad (20)$$

where k = wave number = ω/c, $\omega = 2f$, f = dipole frequency in Hz, c = speed of sound, r = dipole radius, D_r = radial distance between the center of the sphere to the point of interest, θ = angle of radiation, U = amplitude of axial source velocity, t = time. However, particle velocities can also be expressed as the velocity components parallel to the X-, Y- and Z-axis as defined for the experimental setup (c.f. Fig. 28d).

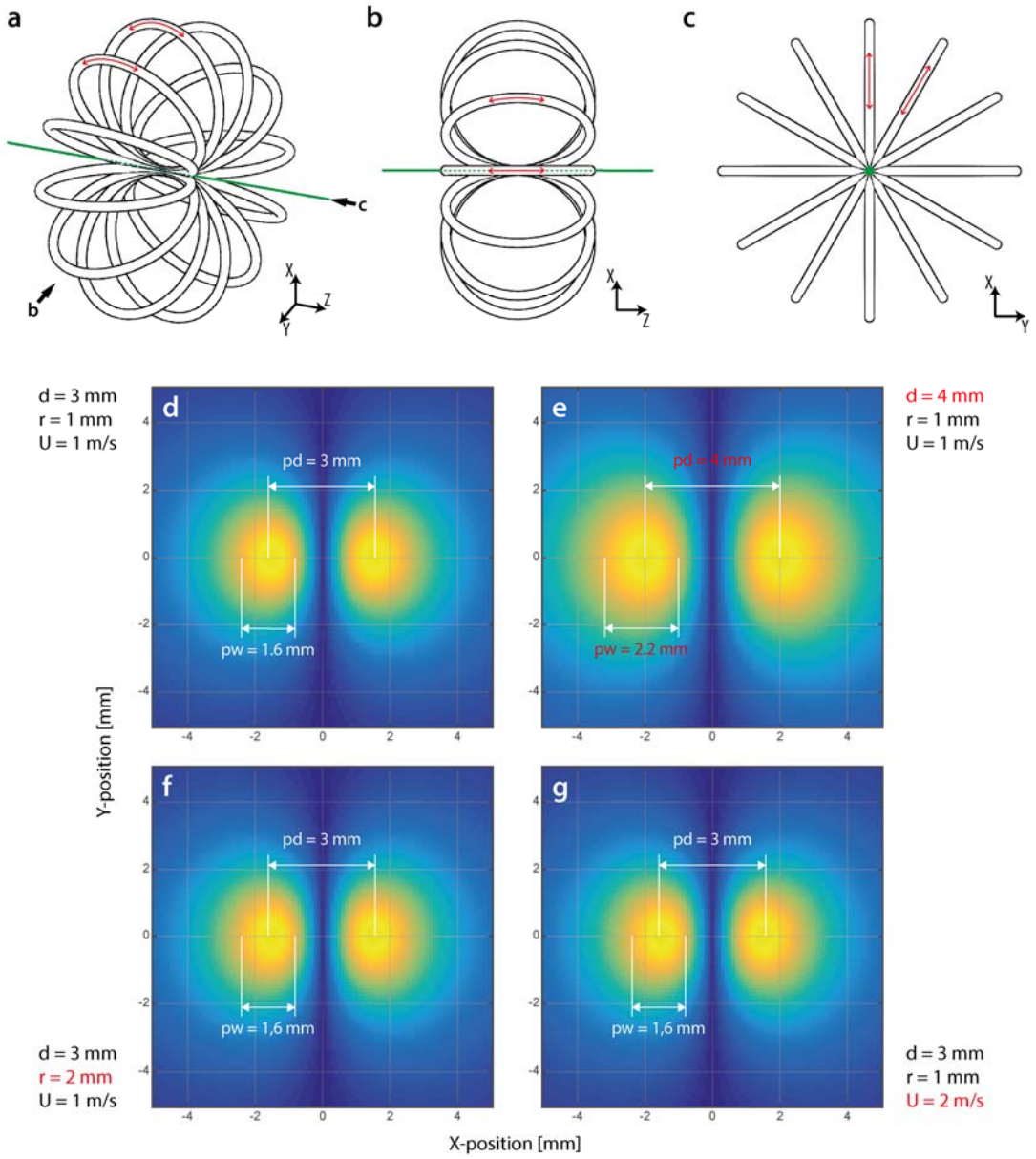

Fig. 45 Stimulus hydrodynamics (**a**-**b**) Fluid particle trajectories in the vicinity of a dipole source. Axis of vibration marked in green. Coordinate axes correspond to the axes definition of the experimental setup (c.f. Fig. 28d). Black arrows in **a** illustrate the point of view in **b** respectively **c**. (**d**-**g**) Calculated particle velocity component along the X-axis in the X/Y plane. Velocity is color coded, warmer colors represent higher velocities. d = distance from the dipole source, r = dipole radius, U = axial dipole velocity, pd = distance between the centers of the 2 spots, pw = width of the spots (spot edges defined as 80 % of the maximum).

4.1.3. Modeling receptive fields

The axis of best sensitivity of most SNs is parallel to the long axis of the fish body (Schmitz et al., 2008) respectively the X-axis in our experiments. The receptive fields should thus correspond to the particle velocity component in X-direction present at the fish surface. Assuming that the fish surface is flat and perpendicular to the axis of vibration and that the dipole source is positioned

3 mm above the fish surface, the receptive field should thus be modelled by calculating the particle velocity in X-direction in the X/Y-plane (perpendicular to the axis of vibration) 3 mm away from a dipole source vibrating in Z-direction.

The resulting calculated receptive field (Fig. 45d) reflects the measured receptive fields quite well: In the X/Y-plane 3 mm away from a dipole source the particle velocity component in X-direction is increased at two distinct spots left (X-) and right (X+) of the axis of vibration (Z-axis, X and Y = 0 mm, c.f. Fig. 45d-g). The distance between the centers of the two spots is 3 mm. That is comparable to the measured receptive fields where the distance between the centers of the two spots ranged from approx. 2 mm (c.f. Fig. 37) to 4.5 mm (c.f. Fig. 32). Also the width of the spots compares well between the calculated flow field and the measured receptive field. Slight variations in shape, size and symmetry might be explained by the assumptions of the model: e.g. the axis of vibration might not have been exactly perpendicular to the curved surface of the fish. Due to methodical restrictions the distance between fish and the dipole source might not always have been 3 mm. Furthermore, the equations mentioned above assume a spherical dipole object, not a cylindrical object as used in the present study. Also, the model does not consider the hydrodynamic interaction between the flow and the fish surface. However, the similarity of the calculated and the measured receptive fields confirms the assumption that the measured receptive fields are, in fact, receptive fields of SNs. The neuromasts most likely were located between the two spots of highest sensitivity and their axis of best sensitivity spanned between the centers of the spots.

Calculating the flow fields is not only important for the comparison with measured data but also helps to understand the stimulus characteristics. Fig. 45e illustrates the flow field further away (4 mm) from the dipole. With increasing distance from the center of the dipole **d** the width of the spots of increased flow velocity **pw** and the distance between the centers of the spots **pd** increases. Thus, larger receptive fields might have been caused by positioning the dipole source further away from the fish surface. In contrast, varying the dipole radius **r** or the amplitude of the axial dipole velocity **U** does not influence the shapes of the calculated flow fields (c.f. Fig. 45f,e). Note that the plotted data is normalized. Of course, e.g. with increasing distance to the dipole source (**d**)

particle velocities decrease. An increased axial dipole velocity (**U**) overall leads to increased particle velocities. However, the calculation of the flow field reveals that – as long as the neuromasts are stimulated within their dynamic amplitude range and as long as the nervous activity is normalized, too – the measured receptive fields only depend on the distance and orientation of the dipole source but not on its radius or axial velocity.

4.1.4. Scan procedures

The results obtained in the line scan procedures differ from the results obtained in the raster scan procedures. Instead of the distinct two spot receptive fields recorded in the raster scans, the line scans resulted in diffuse, inhomogeneous receptive fields (c.f. Fig. 35 and Fig. 36). This cannot be explained by the model described above. Also it is unlikely, that the inhomogeneous fields are caused by morphological features of the SNs of *Anoplarchus*. The only raster scan performed on *Anoplarchus* which, unfortunately, could not be finished, also shows the two spot receptive field characteristics observed in goldfish. Hence, we assume that the inhomogeneous receptive fields are caused by the line scan stimulus. Although the dipole source was moved slowly, unintended vibrations of the entire setup and thus of the dipole source might have stimulated the neuromasts and thus masked the applied dipole stimulus. Another possible disadvantage of the line scan method is the lack of a sharp stimulus onset. The dipole source slowly approached the receptive fields, resulting in a ramp-like stimulus. For phasic and phasic-tonic units such stimulus is much weaker, compared to the sharper stimulus onsets in the raster scans. Lastly, the quality of the recordings was worse in *Anoplarchus*. A worse spike discrimination might have been one reason for the inhomogeneous receptive fields, too. Overall, the line scan procedure does not seem to be a suitable method to precisely determine receptive field properties.

The best scanning method would, however, be to randomly approach different raster locations. This would eliminate the influence of temporal variations in the response properties of the units (e.g. variations in ongoing activity). Unfortunately, the traveling distance of the dipole source would be excessively higher, resulting in longer scanning times. The zickzack-scanning path used in the raster scan procedure was a compromise to decrease the scanning times, accepting the disadvantage of a possible bias due to temporal variations in

neuronal activity. Repeating the scan with different scanning directions and averaging the results could partly compensate for this disadvantage. Depending on the size of the scanned field and the raster resolution, the raster scan procedure still could take up to two hours, a time that bares the risk to lose a unit. The line scan procedure was therefore designed to further decrease the scanning times by avoiding long times between raster scan pulses. As this method did not turn out to be suitable, we suggest that the raster scan procedure is the method of choice for potential future experiments.

4.1.5. Conclusion

Scanning the receptive fields of SNs in goldfish did not uncover new unexpected features of these sensory structures. The results confirmed the expected model of how SNs respond to a dipole stimulus in a spatial context. Nevertheless, our data stands out from earlier studies on receptive fields of lateral line units.

Measuring the receptive fields is commonly used to characterize the properties of lateral line units in the PLLN (Caird, 1978; Coombs et al., 1996, 1998; Goulet et al., 2008; Künzel et al., 2011), the medial octavolateral nucleus of the medulla in the brainstem (Caird, 1978; Bleckmann et al., 1989*b*; Coombs et al., 1998; Künzel et al., 2011) and the torus semicircularis in the midbrain (Engelmann & Bleckmann, 2004; Voges & Bleckmann, 2011; Meyer et al., 2012). However, most of the studies mentioned above only determined the size of the receptive fields in one dimension. Bleckmann et al. (1989) and Voges & Bleckmann (2011) determined the 2-dimensional shape of the receptive fields. The spatial resolution of these receptive field scans and the overall number of data points was low (e.g. approx. 50 data points and a spatial resolution of 5 mm in Voges & Bleckmann (2011)). The results of these studies were hard to explain by a simple model, which might be due to central integration mechanisms. 2-dimensional receptive fields of peripheral lateral line units have never been determined before. The present study not only fills this gap. The 2-dimensional images provide a much higher spatial resolution compared to the studies mentioned above (up to 400 data points and a spatial resolution of 0.2 µm) and the data fits the assumed receptive field model.

The data on the receptive fields of SNs of goldfish was obtained as a by-product in the preliminary tests of the *Xiphister* study. In fact, the low sample size should

be increased in future projects. The methods should be improved and used to study different questions. The setup used in this study does easily allow to extent the image of the receptive field into the third dimension. In addition, it would be interesting to compare the receptive fields of SNs and CNs. However, another reasonable use of the method might still be to uncover the functional significance of lateral line morphologies, not only in *Xiphister*.

4.2. Neuronal activity in the posterior lateral line nerve of *Xiphister*

4.2.1. Insensitivity to hydrodynamic stimuli

Units in the PLLN are known to be hydrodynamic sensitive (Bleckmann, 1994). In contrast, in the present study none of the 111 single and 22 multi units recorded in *Xiphister* responded to hydrodynamic stimuli. This seemingly contradicts the results of Bleckmann & Münz (1990) who found hydrodynamic sensitive units in the PLLN of *Xiphister atropurpureus*, a close relative of *Xiphister mucosus*. Furthermore, Clardy et al. (2014) found neuromasts in the dorso- and mediolateral trunk canals of *Xiphister mucosus*. This finding suggests that hydrodynamic information is transmitted in the PLLN.

It is very unlikely that we only recorded efferents in over hundred cases and that the insensitivity to hydrodynamic stimuli could thus be explained by recording efferents only. In fact, the cut nerve experiments showed that we recorded from both, efferents and afferents.

We used DASPEI staining and scanning electron microscopy to survey the presence of trunk CNs in our animals. Of course, proving the absence of certain morphological structures is always problematic because methodical deficits cannot be excluded. We could not confirm the presence of trunk CNs in the specimens used in the present study. On the one hand this might be the reason for not finding hydrodynamic units. On the other hand, the contradiction to Clardy et al. (2014) – who found CNs in the dorsal and medial lateral line canals of *Xiphister mucosus* – remains and we can only speculate about a possible reasons for the absence of (functional) neuromasts.

One explanation might be that the neuromasts were damaged by external factors such as extreme desiccation, water pollution or diseases. This explanation seems

unlikely because specimens of *Anoplarchus* that were found at the same collecting site had functional neuromasts. Another possible explanation for the absence of neuromasts in the Xiphister trunk canals is that the neuromasts were not damaged but evolutionary reduced. In the course of the identification of the species some inconsistencies throughout the identification literature (Peterson et al., 1999; Lamb & Edgell, 2010) and some ambiguous identification criteria such as variable skin coloring revealed that the classification of *Xiphister* into *Xiphister atropurpureus* and *Xiphister mucosus* might be oversimplified and possibly does not reflect the actual diversity. One might also consider possible seasonal or habitat related adaptations as reasons for the absence of functional neuromasts. However, all of the aforementioned explanations are speculations. Further research is needed to clarify the contradicting results of the different studies.

4.2.2. Discharge patterns

Hydrodynamic insensitive PLLN units with fairly constant discharge patterns such as constant spiking or bursting have occasionally been described in the literature (Münz, 1989). In some studies they are discussed to be efferents, a fact that can be excluded in the present study: We observed constantly spiking or bursting efferent and afferent units (c.f. Fig. 40).

One unit changed its discharge pattern in response to a sudden thermal stimulus from bursting to continuous spiking (Fig. 41e). This observation could not be reproduced (which might just be caused be the overall small sample size with sudden thermal stimuli). Still, it suggests that the discharge pattern classification into two distinct populations (bursting and single spiking) might not properly reflect the functional classification of the units.

4.2.3. Thermal sensitivity

All physiological systems are influenced by temperature. Thus, it is difficult to tell whether a neuronal response to thermal stimuli contributes to a dedicated sensory function.

In Xiphister, warm sudden thermal stimuli led to a decrease and cold sudden thermal stimuli to an increase of neuronal activity. Considering the increased motion of particles at higher temperatures one would more likely expect

increased neuronal activity at higher temperatures. In fact, in steady temperature stimulation an increase in temperature led to an increase in neuronal activity.

Sudden thermal stimuli did not elicit neuronal responses when the fish trunk was submerged. The reason for this might have been that the warm or cold water was instantly mixed with the tank water resulting in a much weaker temperature stimulus.

For comparison, the same experiments were also performed on goldfish. Here, a steady temperature stimulus led to results that were comparable to *Xiphister*. In contrast, sudden thermal stimuli (water jets) did elicit the same neuronal responses, no matter if cold or warm water was applied.

Although the *Xiphister* results seem to be hard to explain, they are in agreement with previous studies. In many studies the ongoing discharge rate of lateral line afferents was positively correlated with steady temperatures (Hoagland 1933 a, b, in bony fishes; Murray 1956 in *Xenopus*; Sand 1938 in *Raia*). In addition, the latter two authors also described the reversed (paradox) response to sudden thermal stimuli. In *Xenopus* the threshold to elicit responses to sudden thermal stimuli was 1-2 °C temperature difference (Murray, 1956). In *Raia*, temperature differences of about 10 °C were needed to elicit these responses (Sand, 1938). The same paradoxical effect was observed in other sensory organs: Much more prominent in the ampullea of Lorenzini (threshold to elicit reversed responses was about 0.1-0.2 °C) and less prominent in dermal stretch receptors. Due to the qualitative similarity of the responses, Sand (1938) suggested that similar biophysical structures of the excitatory systems had caused the observed phenomenon. As a basis for a future working hypothesis he speculates about a model of how identical chemical processes could lead to reversed responses to fast and slow temperature changes. Due to the quantitative differences of the responses, Sand (1938) excludes a functional relevance of the results for neuromasts and stretch receptors. He concludes that those receptor cannot be considered as thermoreceptors.

The present study agrees with the study done on *Raia* (Sand, 1938) and does not allow for any further conclusions. Due to the short period of time in Portland only few recordings could be made, responses to steady temperature stimuli could

not be measured repetitively. We also did not quantify the responses or determine thresholds. Another issue that should be addressed in future studies are the sudden thermal stimuli: warm and cold water jets are bimodal temperature and hydrodynamic stimuli. Especially in goldfish the responses to the hydrodynamic component of the stimulus might have overridden the responses to the temperature component. In future studies pure temperature stimuli should be preferred. Note that the neuromasts of *Raia* that responded to sudden temperature changes did also respond to hydrodynamic stimuli. In fact, this was one criteria to distinguish lateral line units from units that innervated ampullae of Lorenzini or stretch receptors (Sand, 1938). Due to the insensitivity to hydrodynamic stimulation we cannot even guarantee that responses originated from neuromasts. However, the present study is the first to show the paradoxical responses of PLLN units to sudden and steady temperature stimuli in bony fish. It might may be a starting point for further investigations.

4.3. Morphological methods

The first goal of the morphological experiments was to find out whether the mechanical insensitivity of PLLN units in *Xiphister* to hydrodynamic stimuli was due to the absence of (functional) neuromasts in the trunk canals.

4.3.1. DASPEI staining

DASPEI did not stain any structures in *Xiphister*. This does not prove the absence of neuromasts. The lack of staining might have been caused by the morphology of the canal system. As opposed to goldfish, in which the staining of CNs worked well and where the trunk canals are formed by cycloid scales, the *Xiphister* trunk canals are located below the scales and the skin and they are formed by bony ring structures. Thus, the DASPEI fluorescence – if even present – might not have been sufficient enough to be visible through this thicker skin.

Control experiments with goldfish and *Anoplarchus* were performed to exclude other methodical deficits as a reason for the *Xiphister* results. The results of DASPEI staining on goldfish were similar to previous studies (Beckmann et al., 2010) where SNs as well as CNs could easily be stained. The successful staining

of SNs in *Anoplarchus* furthermore demonstrates that the DASPEI staining works under salt water conditions.

4.3.2. Scanning electron microscopy

Scanning electron microscopy confirmed the presence of two rows of SNs on the trunk of *Anoplarchus*; the neuromasts were also identified with DASPEI staining. The neuromasts differ from other studies (Faucher et al., 2003; Schmitz et al., 2008; Beckmann et al., 2010). The cupulae were much less elongated and the non-sensory area around it (Faucher et al., 2003) was not or only barely present. We assume that these differences are caused by methodical differences (e.g. the air drying process) or mechanical stress in the course of the transportation of the samples from Portland to Bonn (e.g. the cupulae might have been broken off).

We searched for CNs in the cephalic lateral line as a positive control for finding CNs with SEM. The examined CNs of *Anoplarchus* basically resembled the CNs found in other studies (Faucher et al., 2003): Located on the medial side of the canals with a smooth non-sensitive area embracing the diamond shaped sensitive cupula/macula area. The cupulae differed from other studies (Faucher et al., 2003; Schmitz et al., 2014). We assume that this might have been caused by methodical differences.

In the cephalic CNs of *Xiphister* the surface was barely raised and structured, no microvilli bundles were visible. As the method was identical to the method used in *Anoplarchus* the smoother surface structure on the *Xiphister* CNs might be an indication for damaged, non-functional neuromasts.

Our data does not confirm the presence of trunk CNs in *Xiphister*. The structures that were most similar to the CNs found in the cephalic canals lacked the diamond shape. A diameter of 50 µm is much less than the 128 µm diameter quoted in Clardy et al. (2014). Still, the neuromast like structures are reported because they stand out from the surrounding epithelial cells.

Further morphological features like the notched tip of the SNs, the circular, dorsally and ventrally extended crests around the SNs on the trunk of *Anoplarchus* or the circular SN pattern around the nostril of *Anoplarchus* and *Xiphister* are reported. We will not speculate about possible functions of these

structures. Note that the method used to air-dry the samples does not guarantee that the observed cupula shapes resemble the situation in an intact animal.

4.4. Conclusion

The aim of the study was to investigate the receptive fields of trunk CNs in *Xiphister* in order to confirm the spatial filter hypothesis (Klein et al., 2013). However, although we failed this original aim, several ideas for future work derived from the research project in Portland.

The receptive field scans of primary lateral line units in goldfish are the most detailed scans described so far. The setup and working method are promising for further research on the form/function relationship in lateral line morphologies other than the *Xiphister* trunk canals.

The reason for the unexpected insensitivity of PLLN units to mechanical stimulation in *Xiphister* remains unclear. Unraveling this puzzle by comparing specimens of different habitats or at different times of the season might be a research project on its own.

The briefly investigated influence of temperature on the responses of PLLN units needs to be quantified in further research for a better comparison with the similar findings in *Raia* (Sand, 1938) and *Xenopus* (Murray, 1956).

Bibliography

Beckmann M, Erös T, Schmitz A & Bleckmann H (2010). Number and distribution of superficial neuromasts in twelve common European cypriniform fishes and their relationship to habitat occurrence. *Int Rev Hydrobiol* **95,** 273–284.

van Bergeijk WA & Alexander S (1962). Lateral line canal organs on the head of Fundulus heteroclitus. *J Morphol* **110,** 333–346.

Bleckmann H (1985). Perception of Water Surface Waves: How Surface Waves Are Used for Prey Identification, Prey Localization, and Intraspecific Communication. In *Progress in Sensory Physiology 5*, ed. Autrum H, Ottoson D, Perl ER, Schmidt RF, Shimazu H & Willis WD, pp. 147–166. Springer, Berlin.

Bleckmann H (1988). Prey Identification and Prey Localization in Surface-feeding Fish and Fishing Spiders. In *Sensory Biology of Aquatic Animals*, ed. Atema J, Fay RR, Popper AN & Tavolga WN, pp. 619–641. Springer, Berlin.

Bleckmann H (1994). *Reception of hydrodynamic stimuli in aquatic and semiaquatic animals*ed. Rathmayer W. Gustav Fischer, Jena.

Bleckmann H & Münz H (1990). Physiology of lateral-line mechanoreceptors in a teleost with highly branched, multiple lateral lines. *Brain Behav Evol* **35,** 240–250.

Bleckmann H & Schwartz E (1982). The functional significance of frequency modulation within a wave train for prey localization in the surface-feeding fishAplocheilus lineatus (Cyprinodontidae). *J Comp Physiol A* **145,** 331–339.

Bleckmann H, Tittel G & Blübaum-Gronau E (1989*a*). The Lateral Line System of Surface-Feeding Fish: Anatomy, Physiology, and Behavior. In *The Mechanosensory Lateral Line*, ed. Coombs S, Görner P & Münz H, pp. 501–526. Springer, Berlin.

Bleckmann H, Waldner I & Schwartz E (1981). Frequency discrimination of the surface-feeding fish Aplocheilus lineatus - A prerequisite for prey localization? *J Comp Physiol* **143,** 485–490.

Bleckmann H, Weiss O & Bullock TH (1989*b*). Physiology of lateral line mechanoreceptive regions in the elasmobranch brain. *J Comp Physiol* **164,** 459–474.

Caird DM (1978). A Simple Cerebellar System: The Lateral Line Lobe of the Goldfish. *J Comp Physiol A* **127,** 61–74.

Chagnaud BP, Bleckmann H & Hofmann MH (2007). Kármán vortex street detection by the lateral line. *J Comp Physiol A* **193,** 753–763.

Clardy TR & Hilton EJ (2015). Osteology of the prickleback genus Xiphister (Cottiformes: Zoarcoidei: Stichaeidae). *Acta Zool*; DOI: 10.1111/azo.12118.

Clardy TR, Hilton EJ & Vogelbein WK (2015). Morphology and ontogeny of multiple lateral-line canals in the rock prickleback, Xiphister mucosus (Cottiformes: Zoarcoidei: Stichaeidae). *J Morphol* **276,** 1218–1229.

Coombs S (1988). Diversity of lateral line systems: evolutionary and functional considerations. In *Sensory Biology of Aquatic Animals*, ed. Atema J, Fay RR, Popper AN & Tavolga WN, pp. 553–559. Springer, Berlin.

Coombs S (2002). Imaging of the hydrodynamic environment by the peripheral lateral line system. *Bioacoustics* **12,** 148–150.

Coombs S, Hastings M & Finneran J (1996). Modeling and measuring lateral line excitation patterns to changing dipole source locations. *J Comp Physiol A* **178,** 359–371.

Coombs S, Mogdans J, Halstead M & Montgomery J (1998). Transformation of peripheral inputs by the first-order lateral line brainstem nucleus. *J Comp Physiol A* **182,** 609–626.

Denton EJ & Gray J (1983). Mechanical factors in the excitation of clupeid lateral lines. *Proc R Soc Lond B Biol Sci* **218,** 1–26.

Denton EJ & Gray J (1988). Mechanical Factors in the Excitation of the Lateral Lines of Fishes. In *Sensory Biology of Aquatic Animals*, ed. Atema J, Fay RR, Popper AN & Tavolga WN, pp. 595–617. Springer, Berlin.

Dijkgraaf S (1963). The functioning and significance of the lateral-line organs. *Biol Rev Camb Philos Soc* **38,** 51–105.

Engelmann J & Bleckmann H (2004). Coding of lateral line stimuli in the goldfish midbrain in still and running water. *Zoology* **107,** 135–151.

Faucher K, Aubert A & Lagardere JP (2003). Spatial distribution and morphological characteristics of the trunk lateral line neuromasts of the sea bass (Dicentrarchus labrax, L.; Teleostei, Serranidae). *Brain Behav Evol* **62,** 223–232.

Goulet J, Engelmann J, Chagnaud BP, Franosch J-MP, Suttner MD & van Hemmen JL (2008). Object localization through the lateral line system of fish: theory and experiment. *J Comp Physiol A* **194,** 1–17.

Grap NJ, Monzel AS, Kohl T & Bleckmann H (2015). Crocodylus niloticus (Crocodilia) is highly sensitive to water surface waves. *Zoology* **118,** 320–324.

Hassan E (1985). Mathematical analysis of the stimulus for the lateral line organ. *Biol Cybern* **36,** 23–36.

Hoagland H (1933*a*). Electrical responses from the lateral-line nerves of catfish . I. *J Gen Physiol* **16,** 695–714.

Hoagland H (1933*b*). Quantitative analysis of responses from lateral-line nerves of fishes. II. *J Gen Physiol* **16,** 715–732.

Janssen J (1997). Comparison of response distance to prey via the lateral line in the ruffe and yellow perch. *J Fish Biol* **51,** 921–930.

Kalmijn AJ (1988). Hydrodynamic and acoustic field detection. In *Sensory Biology of Aquatic Animals*, ed. Atema J, Fay RR, Popper AN & Tavolga WN, pp. 83–130. Springer, Berlin.

Kestin J, Khalifa HE & Correia RJ (1981). Tables of the dynamic and kinematic viscosity of aqueous NaCl solutions in the temperature range 20–150 °C and the pressure range 0.1–35 MPa. *J Phys Chem Ref Data* **10,** 71–87.

Klein A (2009). *Examination of artificial lateral line systems* (thesis). Bonn.

Klein A (2012). *Vortex sensing and energy expenditure of fish exposed to unsteady flow and biomimetic transfer of noise filter and signal amplification techniques* (thesis). Bonn.

Klein A & Bleckmann H (2011). Determination of object position, vortex shedding frequency and flow velocity using artificial lateral line canals. *Beilstein J Nanotechnol* **2,** 276–283.

Klein A, Herzog H & Bleckmann H (2011). Lateral line canal morphology and signal to noise ratio. In *Proceedings of SPIE*.

Klein A, Münz H & Bleckmann H (2013). The functional significance of lateral line canal morphology on the trunk of the marine teleost Xiphister atropurpureus (Stichaeidae). *J Comp Physiol A* **199,** 735–749.

Kroese a B & Schellart N a (1992). Velocity- and acceleration-sensitive units in the trunk lateral line of the trout. *J Neurophysiol* **68,** 2212–2221.

Künzel S, Bleckmann H & Mogdans J (2011). Responses of brainstem lateral line units to different stimulus source locations and vibration directions. *J Comp Physiol A* **197,** 773–787.

Lamb A & Edgell P (2010). *Coastal Fishes of the Pacific Northwest, Revised and Expanded Second Edition*, 2nd edn. Harbour, Madeira Park.

Liao JC, Beal DN, Lauder G V & Triantafyllou MS (2003). The Kármán gait: novel body kinematics of rainbow trout swimming in a vortex street. *J Exp Biol* **206,** 1059–1073.

Lighthill J (2001). *Waves in Fluids*. Cambridge University Press, Cambridge.

Makushok V (1961). *Some peculiarities in the structure of the seismosensory system of the northern Blenniids (Stichaeoidae, Blennioidei, Pisces)*. U.S. Bureau of Commercial Fisheries, Washington D.C.

Matthews SA (1931). Observations on Pigment Migration Within the Fish Melanophore. *Am J Med Sci* **181,** 449.

Merrilees MJ & Crossman EJ (1973). Surface pits in the family Esocidae - I. Structure and Types. *J Morphol* **141,** 307–320.

Meyer G, Klein A, Mogdans J & Bleckmann H (2012). Toral lateral line units of goldfish, Carassius auratus, are sensitive to the position and vibration direction of a vibrating sphere. *J Comp Physiol A* **198,** 639–653.

Münz H (1979). Morphology and Innervation of the Lateral Line System in Sarotherodon niloticus (L.) (Cichlidae, Teleostei). *Zoomorphologie* **93,** 73–86.

Münz H (1989). Functional Organization of the Lateral Line Periphery. In *The Mechanosensory Lateral Line*, ed. Coombs S, Görner P & Münz H, pp. 285–297. Gustav Fischer, Jena.

Murray R (1956). The thermal sensitivity of the lateralis organs of Xenopus. *J Exp Biol* **33,** 798–805.

Nelson J (2006). *Fishes of the World*. John Wiley & Sons, Hoboken.

van Netten SM (2006). Hydrodynamic detection by cupulae in a lateral line canal: functional relations between physics and physiology. *Biol Cybern* **94,** 67–85.

Oakley B & Schafer R (1978). *Experimental Neurobiology: A Laboratory Manual*. University of Michigan Press, Ann Arbor.

Ozbek H, Fair JA & Phillips SL (1977). Viscosity of Aqueous Sodium Chloride Solutions from 0 - 150° C. 1–68.

Peterson RT, Eschmeyer WN, Herald ES, Hammann HE & Smith KP (1999). *A Field Guide to Pacific Coast Fishes: North America*. Houghton Mifflin Harcourt, Boston.

Sand A (1938). The Function of the Ampullae of Lorenzini, with some Observations on the Effect of Temperature on Sensory Rhythms. *Proc R Soc B Biol Sci* **125,** 524–553.

Schlichting H & Gersten K (2004). *Boundary-layer theory*. Springer, Berlin.

Schmitz A, Bleckmann H & Mogdans J (2008). Organization of the superficial neuromast system in goldfish, Carassius auratus. *J Morphol* **269,** 751–761.

Schmitz A, Bleckmann H & Mogdans J (2014). The lateral line receptor array of cyprinids from different habitats. *J Morphol* **275,** 357–370.

Schwartz E (1970). Ferntastsinnesorgane von Oberflächenfischen. *Zeitschrift für Morphol der Tiere* **67,** 40–57.

Schwartz E (1971). Die Ortung von Wasserwellen durch Oberflächenfische. *Z Vgl Physiol* **74,** 64–80.

Vogel D & Bleckmann H (1997). Water wave discrimination in the surface-feeding fish Aplocheilus lineatus. *J Comp Physiol A* **180,** 671–681.

Vogel S (1996). *Life in Moving Fluids: The Physical Biology of Flow*. Princeton University Press, Princeton.

Voges K & Bleckmann H (2011). Two-dimensional receptive fields of midbrain lateral line units in the goldfish, Carassius auratus. *J Comp Physiol A* **197,** 827–837.

Webb JF (1989). Developmental Constraints and Evolution of the Lateral Line System in Teleost Fishes. In *The Mechanosensory Lateral Line*, ed. Coombs S, Görner P & Münz H, pp. 79–97. Gustav Fischer, Jena.

Yang Y, Nguyen N, Chen N, Lockwood M, Tucker C, Hu H, Bleckmann H, Liu C & Jones DL (2010). Artificial lateral line with biomimetic neuromasts to emulate fish sensing. *Bioinspir Biomim* **5,** 1–9.

Young J (1933). The preparation of isotonic solutions for use in experiments with fish. *Pubbl staz zool Napoli* **12,** 425–431.

Appendix

A. Ringer's solution

Fresh water (Oakley & Schafer, 1978):

- NaCl 100.99 mM
- $NaHCO_3$ 25 mM
- KCl 3.5 mM
- $MgSO_4$ 3.1 mM
- $CaCl_2$ 2.5 mM
- Na_2HPO_4 1.26 mM
- TRIS-Buffer 1 mM

Salt water (Young, 1933):

- NaCl 204.4 mM
- KCl 8 mM
- $CaCl_2$ 4.0 mM
- $MgCl_2$ 3.65 mM
- $NaHCO_3$ 2.25 mM

B. Skin color change

Specimens of *Xiphister* and *Anoplarchus* showed changes of their skin color. *Xiphister* were completely dark immediately after being caught from the housing tank before the experiments and mostly changed their color to dark/green spotted or even completely green. Specimens of *Anoplarchus* sometimes even changed their color from uniformly dark to a colorful pattern. Occasionally – in both species – the color also changed from a brighter back to a darker shade.

Figures a and b exemplify the color change of a specimen of *Xiphister* in the course of 30 minutes. Samples of the skin were examined under a dissecting microscope revealing dark, palmate-like structures of about 100 µm in diameter (Figure c). They were identified as melanophores by shape and size (c.f. Matthews, 1931) and most likely are responsible for the change of skin color.

Skin color change in fishes in general is a well investigated phenomenon. However, for *Anoplarchus* and *Xiphister* the observed color change capability was unexpected and is not explicitly covered in the literature. Hence, we report the phenomenon.

Xiphister **– Skin color change** Skin color before (**a**) and after (**b**) a period of 30 minutes. (**c**) Skin sample in transmitted light under a dissecting microscope, presumably uncovering melanophores.